Combining Perovskites and Quantum Dots: Synthesis, Characterization, and Applications in Solar Cells, LEDs, and Photodetectors

Soumyadipta Rakshit, Piotr Piatkowski, Iván Mora-Seró, and Abderrazzak Douhal*

Metal halide perovskites having high defect tolerance, high absorption characteristics, and high carrier mobility demonstrate great promise as potential light harvesters in photovoltaics and optoelectronics and have experienced an unprecedented development since their occurrence in 2009. Semiconductor quantum dots (QDs), on the other hand, have also been proved to be very flexible toward shape, dimension, bandgap, and optical properties for constructing optoelectronic devices. Of late, a strategic combination of both materials has demonstrated extraordinary promise in photovoltaic applications and optoelectronic devices. Combining QDs and perovskites has proved to be quite an effective strategy toward the formation of pinhole-free and more stable perovskite crystals along with tunability of other properties. To boost this exciting research field, it is imperative to summarize the work done so far in recent years to provide an intriguing insight. This review is a critical account of the advanced strategy toward combining these two fascinating materials, including their different synthetic approaches regarding heteroepitaxial growth of perovskite crystals on QDs, carrier dynamics at the interface and potential application in the field of solar cells, light emitting diodes, and photodetectors.

1. Introduction

Sustainability is a key fundamental of Mother Nature, and the sun, wind, earth, and water are sources of renewable energy that can assist to ensure a sustainable future.[1] Renewable energy sources are encouraged over conventional fossil fuels because they are replenishable and can minimize greenhouse gas emissions, which aids to make the environment greener.[2] Thus far, fossil fuels have been used to meet most of the current world's energy demands; this has single-handedly depleted natural sources and acted as the driving force for climate change.[3,4] From an industrial viewpoint, solar cells, batteries, fuel cells, and light emitting diode (LED)-based lighting devices are sustainable alternatives for replacing traditional energy sources.[5–8] Given this scenario, solar power is the most abundant, clean, sustainable, and unperturbed energy source that can meet the current energy demand.[9,10] However, harvesting solar energy using conventional photovoltaics (PVs) remains challenging in terms of cost and efficacy. Therefore, there is an urgent need to design next-generation low cost, highly efficient, and sustainable PVs.

From a carbon and environmental footprint viewpoint, solar cells are the most cost-efficient approach to generate electricity,[11] and LEDs, which work in reverse, to produce light; both devices have very similar architectures.[12–14] Over the past few decades, commercial Si-based solar cells have been used extensively owing to their high power conversion efficiency (PCE) of up to 22%, excellent device stability, long-range light absorption capability,[15] and outstanding long-term stability. Thus far, materials with efficiency

S. Rakshit, A. Douhal
Departamento de Química Física
Facultad de Ciencias Ambientales y Bioquímica
and INAMOL
Universidad de Castilla-La Mancha
Avenida Carlos III, Toledo 45071, Spain
E-mail: Abderrazzak.douhal@uclm.es

P. Piatkowski[+]
Faculty of Chemistry
University of Warsaw
Pasteura 1, Warsaw 02–093, Poland

I. Mora-Seró
Institute of Advanced Materials (INAM)
University Jaume I
Avenida de Vicent Sos Baynat, Castellón de la Plana, Castellón 12071, Spain

[+]Present address: Department of Physics, American University of Sharjah, Sharjah PO Box 26666, UAE

records for solar cells, and InGaN, AlGaInP, and AlGaAs have been employed to develop conventional commercialized LED modules III–V semiconductors of the GaAs family.[16,17] The traditional high cost, energy payback, and environmental foot-print of these materials have led scientists to focus on more exciting and effective approaches for developing next-generation energy devices. To this end, dye-sensitized solar cells can obtain a PCE of >13%; however, a higher complexity in designing sensitizer dyes and contact layers with mesoporous titania has led to further development.[18,19] In this regard, QDs play a pivotal role; QD-based solar cells and LEDs have attracted considerable interest and are believed to be potential candidates for next-generation PVs because of their characteristics such as easy bandgap tunability, easy solution-based synthetic procedure, and ability to generate multiple excitons[20–23] until the arrival of perovskites (PSs) in 2009. Thin-film PV technology, PS-based solar cells, and LEDs have witnessed remarkable and unprecedented advancements in the last five years at speeds never seen in the history of PV development.[12,13,24] After the introduction of the first solid-state perovskite solar cell (PSC) in 2012 with a PCE ~ of 9.7%,[25] researchers have improved it to 25.5% at present.[26] Further, PS LEDs exhibit excellent external quantum efficiency (EQE) (>20%) with very high color purity to satisfy REC.2020 due to their higher charge carrier mobility and lack of exciton annihilation processes.[27,28]

Although laboratory-scale PS-based PV devices demonstrate considerable advancement, device stability in the presence of moisture, humidity, temperature, and UV light continue to remain significant obstacles.[29] The basic PSC operates through different steps, which include charge photogeneration by photon absorption in the PS layer and subsequent charge separation at the respective selective contacts.[30–32] Electrons and holes are separately collected at the electrode by the electron transport layer (ETL) and hole transport layer (HTL), respectively, to ensure the migration of the charge away from the PS absorber layer.[33,34] However, for LEDs, these layers act as injecting layers and the radiative recombination of the injected charge is pursued; the nonradiative recombination must be suppressed simultaneously to achieve the maximum electroluminescence efficiency.[35] Therefore, successful strategies are essential to maximize the PCE and EQE of PS-based nanostructured PVs and augment stability concurrently for successful commercialization. A significant and effective proof of concept has been developed in the last 5 years by combining the two most important materials, QDs and PS.

Careful designing of hybrid materials has brought forth an effective strategy for increasing the performance of single materials owing to the combination of desirable physical properties and characteristics of both materials.[36–38] A strategic combination of QDs and PSs to construct composite thin films that can introduce the best of both materials with enhanced stability and desiring optoelectronics properties can be considered crucial for designing more efficient and stable PVs (**Figure 1**). The scope of this review refers to critical analysis and summarization of the advancement so far done in the field of QD/PS hybrids for photovoltaic applications. We elaborate on the fabrication strategies of various QD/PS combinations and their systematic progress toward trap-free interface engineering for more stable PV devices. The extraction and transport of photogenerated carriers at the PS-charge transfer layer (CTL) interface is reviewed
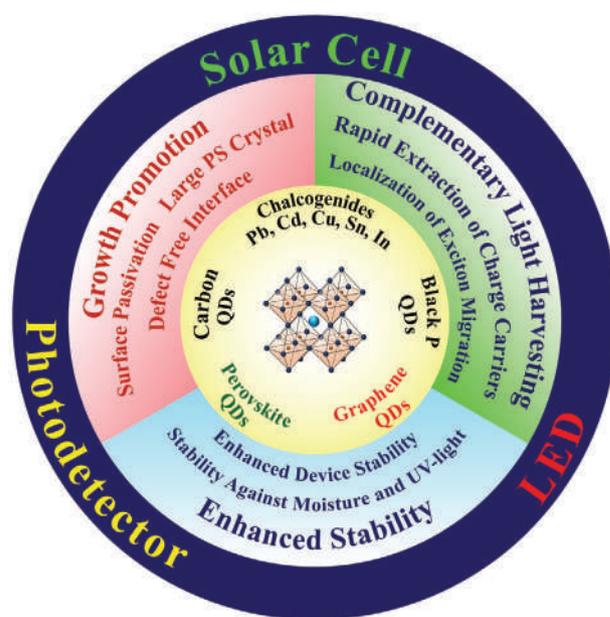
Figure 1. Schematic illustration of the effect of different integrated quantum dots on different properties of perovskites and chief applications of the QD/Perovskite hybrid systems.

with an emphasis on the modified carrier dynamics induced by the inclusion of QDs. Finally, the key effect of the strategic integration of QDs (Pb-based chalcogenides, Cd-based chalcogenides, In-based chalcogenides, perovskite quantum dots (PSQDs), graphene QDs (GQDs), carbon QDs (CQDs), black phosphorus, etc.) on the PS layer in terms of enhancing stability, charge carrier extraction, and PV performance is intricately delineated with special references to solar cells, LEDs, and photodetectors.

2. Synthesis and Challenges

Perovskites have the ability to amass the charge by themselves with a high carrier lifetime which renders them to achieve high photovoltaic conversion efficiencies in the last decade.[12,30,33,35,39,40] On the other hand, QDs are known for their stability, pure bright emission, and bandgap tunability. Since both the materials possess extraordinary optoelectronic properties, the combination of stability and brightness of QDs and long-range charge carrier transport of PSs can be rendered for finding a smart approach for a wide range of optoelectronic devices. The combination can be done in various ways: Passivation of the QDs in the perovskite matrix, constructing perovskite and QD multilayers, growth of QD and PS heterojunction in solution and capping of QDs with PS and vice versa. The primary goals for the formation of the QD/PS hybrids are increasing the stability, enhancing energy level alignment, and efficient charge extraction.[38,41–43]

The incorporation, and/or passivation of the QDs in the perovskite matrix endorse superior crystallization with better morphology. Uniformly distributed QDs with hydrophobic ligands reduce the trap state density and protect the surface from moisture-induced degradation as well. However, one of the most interesting aspects is that the ligand exchange step has the ability to introduce the possibility to exchange to short

ligands, which can directly improve the interdot electronic interaction and passivation of the trap states.[41–43] The tunable bandgap of the QDs up to the NIR region also gives the opportunity for the complimentary light-harvesting which extends the absorption from visible to the NIR region with QD-enhanced light collection.[38,41,42] Another significant objective for the generation of the nano heterojunction composed of discrete QDs and PS by chemical bonding or physical contact is to manage interfacial band alignment for efficient carrier transport and rapid extraction of charge carriers by creating interfacial dipole.[42,44,45] This directly influences and enhances the fill factor, short-circuit photocurrent, and PCE.[44–46] Therefore, designing potential QD/PS hybrid materials where the constructive synergies can disseminate the properties of individual materials, enhance, and/or generate new ones is undoubtedly a potential challenge for material scientists.[46,47]

In the following, we discuss the reported synthetic routes to get QD/PS hybrid materials. Passivation, incorporation, and capping, all are going to be highlighted on the basis of different QDs.

2.1. Integration of Quantum Dots in Organic–Inorganic Perovskites

2.1.1. Pb Chalcogenide Based Quantum Dots in Organic–Inorganic Perovskites

Poor control over the growth of the PS crystal often results from the choice of solvents, composition, temperature, and the effect of the underlayer of the film. This might be overcome by using the QDs as seeds to induce PS crystal growth. The synergy of both materials can be exploited for improved crystallization and interface engineering.[45,46] To design the hybrid polyheterocrystalline material, an organic-ligand-free strategy was implemented to cap the PbS nanoparticles (NPs). The organic ligands were exchanged on the PbS QDs with a short anionic iodide ligand (CH_3NH_2I).[45] The PbS QDs with CH_3NH_2I at the surface were then dissolved in butylamine along with PbI_2 to form QDs in PS as PbI_2 is prone to form a complex with CH_3NH_2I. Subsequently, atomic-level coherence between the inorganic PbS and the organometallic $MAPbI_3$ phase was achieved without the formation of interfacial and in-gap defects and aggregates, which offered uniform and controlled growth of the PS films over large areas with atomic thickness precision. The results empowered epitaxy for constructing QD/PS heteronanocrystals. Manifestation of atom-scale crystalline coherence in light of the lattice structure and interfacial energy between the PbS QDs and $CH_3NH_3PbI_3$ paved the way for others to walk in this path to design new strategies for developing modified QD/PS systems, along with enhanced optoelectronic properties and PCE.

Lately, coherence between solution-processed $CH_3NH_3PbBr_3$ PS single crystals and PbS QDs has been reported by different groups.[44,48–50] The synthetic pathways are more or less similar, which includes the ligand exchange process to transfer the PbS QDs prepared by the conventional hot injection method to the DMF phase to make the QD solid out of it and the growth of $MAPbBr_3$ single crystals by the modified antisolvent

vapor-assisted crystallization method, keeping the QD solids dispersed. Different ligand exchange procedures, comprising the substitution of the MA group by other alkylammonium sources with longer carbon chains to embed higher QD concentrations, have also been employed, resulting in a smoother interface between the active layer of 2D PSs and charge transport layers.[51] Recently, an interfacial heterojunction engineering method has been demonstrated to suppress the trap states at the interface and grain boundaries of MA-free PS by passivating a PbS layer. Introduction of the PbS layer during the antisolvent process of the PS film fabrication reduced the non-radiative recombination, resulting in a PCE of 21.07% along with excellent long-term ambient stability.[52] An intriguing technique to stabilize formamidinium lead iodide (FAPI) PS by taking advantage of the synergistic interaction of halide PSs with colloidal PbS QDs, but not through the introduction of alternative cations or anions to FA^+ and I^- has also been reported.[53] The PbS-FAPI interface created stronger chemical bonds with the black phase and reduced the thermodynamic preference for the yellow phase. The synergistic interaction of halide PSs with colloidal PbS QDs has been used in a very effective way to stabilize the FAPI. A superior path was accomplished as well by the same group to stimulate the favorable growth and orientation of $FA_{0.9}Cs_{0.1}PbI_3$ grains by introducing PbS nanoplates, which improved the atomic interactions to prevent degradation and promoted long-term stability at ambient temperature.[54]

Visible–NIR emissive hybrid PbS QD/PS system via an antisolvent additive solution process has also been developed. The volume of the antisolvent additive plays a decisive role in augmenting crystallinity and uniform grain size of the hybrids.[55] The addition of PbS QDs to the antisolvent increased the number of grains produced by the spin-coating process, ensuring the immobilization of the PbS QDs between the grain boundaries (**Figure 2**A). Besides, a solid-state ligand exchange method was established to obtain smooth, continuous, and thick PbS QD/$CH_3NH_3PbI_3$ hybrid film, which demonstrated superior efficiency as an active layer in solar cells.[56] In this synthetic pathway, the use of the highly volatile solvent acetonitrile proved to be critical (Figure 2B).[56] Compared to the original PbS QDs, the PbS QD/$CH_3NH_3PbI_3$ hybrid QDs exhibited complementary optical absorption spectra, facile charge separation, increased conductivity, and efficient charge transport. A triple cation $Cs_{0.05}(MA_{0.17}FA_{0.83})_{0.95}Pb(I_{0.9}Br_{0.1})_3$ PS composition was also employed for surface passivation of the PbS QDs, resulting in a record PCE of 11.3% through higher interdot coupling and suppressed recombination, majority of earlier reports on PbS solar cells.[57] Fascinating hybrid bilayers of $CH_3NH_3PbCl_xI_{3-x}$ PS and core/shell PbS/CdS QDs via both the PS/QD and QD/PS approach have been fabricated,[58] and the PS/QD exciplex bear promise toward an interesting scenario for the development of new and advanced optoelectronic devices.

In another report, a unique route was reported by introducing a hybrid vapor-assisted chemical bath deposition to fabricate $CH_3NH_3PbI_3$ from PbS.[59] The first step involved the generation of high-quality PbS precursor films without any pinhole and ditch defects and was completely different from the conventional PbI_2 layers by chemical bath deposition and subsequent chemical vapor deposition (CVD) produced smooth and high-quality uniform $CH_3NH_3PbI_3$ films, which exhibited
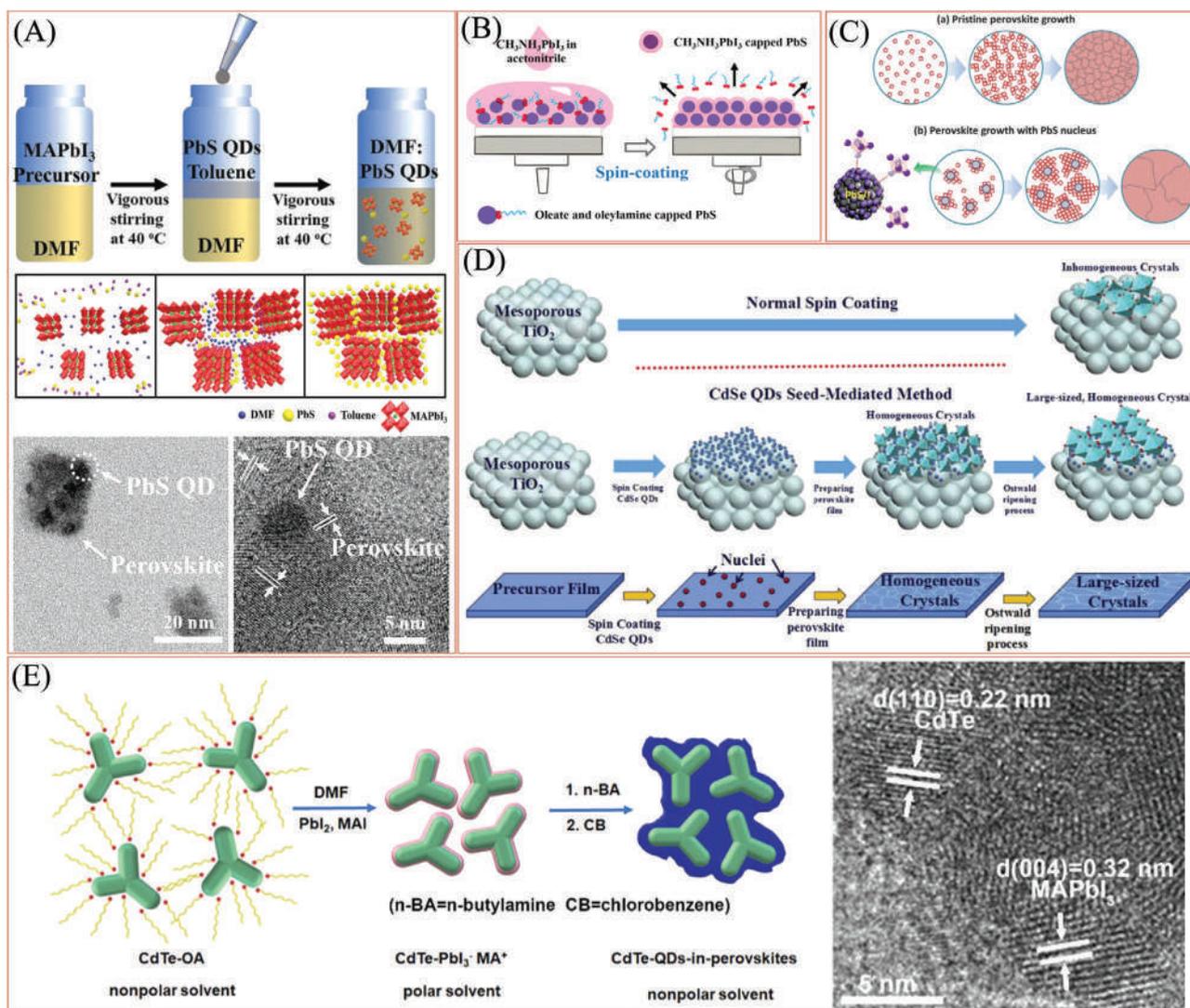
Figure 2. A) Illustration of the preparation of the perovskite precursor using the antisolvent additive solution process and of the PbS QDs attachment at the perovskite surface along with the different orientations of the lattice fringes given by TEM. Reproduced with permission.[55] Copyright 2018, Wiley-VCH. B) Schematic presentation of the synthesis of the CH₃NH₃PbI₃/PbS through solid state ligand exchange method. Reproduced with permission.[56] Copyright 2018, Wiley-VCH. C) Illustration of the nucleation and growth routes of perovskite crystal thin films without and with MAI-capped PbS nanoparticles. Reproduced with permission.[62] Copyright 2016, The Royal Society of Chemistry. D) Schematic of the spin coating process and the CdSe QDs seed-mediated method to fabricate PSCs. Reproduced with permission.[64] Copyright 2018, Elsevier. E) Illustration of the ligand exchange process of CdTe QDs to insert CdTe in MAPbI₃ along with the HRTEM image of the composites. Reproduced with permission.[65] Copyright 2018, Elsevier.

a preliminary PCE of 4.68%.[60] However, a fairly simple procedure was formulated in which ultrathin 2D PbS NCs were directly converted into uniform rectangular hybrid perovskite nanocrystals (PSNCs) by an all-anion exchange reaction route directly on solid substrates containing large planar areas.[61]

Unlike their use as seeds, intermixing the PbS QDs during the growth of the PS film furnishes a very high-quality $CH_3NH_3PbI_{3-x}Cl_x$ PS film.[62] The methylammonium iodide (MAI)-capped PbS QDs amplified the miscibility with the PS precursor in DMF and acted as active sites to facilitate the formation of lead–halide octahedrons near the surface of the QDs. The QDs also served as effective heterogeneous nucleation sites over the entire film to produce larger crystalline domains,

resulting in a high-performance planar heterojunction PSC yielding an excellent PCE of 17.4%. The synergistic effect of the PbS QDs in the heterogeneous nucleation of $MAPbI_{3-x}Cl_x$ PS crystals decreased the number of nucleation sites, facilitating larger high-quality crystals (Figure 2C). In another report, PbS QDs were adsorbed on the surface of perovskite films through in situ reaction with thioacetamide (TAA) in solution.[63] With the PbS layer, the trap state density of the perovskite film was significantly reduced, and charge extraction efficiency was enhanced from perovskite to the external charge transport layer.[63]

The interaction of PSs with PbS QDs can be managed by preparing bilayers that mostly imply surface passivation

or by forming a PS matrix with embedded QDs. While both approaches reported fascinating outcomes in terms of improved performance, the latter could bring the synergistic interaction to the most interesting level with essential implications for the development of advanced device configurations or enhanced properties in terms of efficiency and stability.

2.1.2. Cd-Based Quantum Dots in Organic–Inorganic Perovskites

QDs have been used to modulate the morphology, crystallinity, and high surface coverage by controlling the nucleation and growth for fabricating flexible PS film-based optoelectronic devices. The growth of the PS layer was prompted over an ultrathin CdSe QD film, and it plays the role of a seed-mediated underlayer (Figure 2D).[64] The presence of the QD layer not only minimized the defect and trap densities but also recrystallized small-sized crystals into large PS grains via a simple methylammonium bromide (MABr) treatment to achieve a PCE of 15.68%. Considering the feasibility of air-based measurements, this strategy can deliver a more general and promising route for developing high-performance PSCs with controlled PS crystallization and optimized interfaces. In another work, passivation of the perovskite surface with CdSe/ZnS QDs decreased the trap density and, simultaneously stabilized the organo-lead trihalide perovskite chemical structure and extend the charge carrier lifetime.[43]

The passivation of the CdTe QD layer has also been employed to induce high hole mobility. CdTe QDs were synthesized via the classical hot-injection method, cleaned by the solvent/anti-solvent method, and opted for ligand exchange to remove the long-chain alkyl ligand capped on CdTe QDs (Figure 2E).[65] However, the next step in synthesizing the CdTe/$CH_3NH_3PbI_3$ hybrids involves surface passivation or embedding QDs on the perovskite matrix.[45,56]

Recently, a solution phase synthetic route has been reported where CdS QDs have been proved to be quite effective for the formation of stable $CsPbBr_3$/CdS heterostructures which showed efficient charge transfer.[66]

2.1.3. Green Quantum Dots (Free from Pb and Cd) in Organic–Inorganic Perovskites

Most studies on the interaction between PS and QDs were performed with Pb-based PS. Therefore, the utilization of QDs containing Pb or Cd has not been considered a significant drawback in combination with Pb-based PSs. However, the toxicities of Pb and Cd limit their applications. Thus, the use of green QDs with less hazardous elements is a very interesting research topic—even in combination with Pb-based PSs—because the results can be more easily extrapolated to a Pb-free system. A double-active-layer photodetector was fabricated based on $CH_3NH_3PbI_3$ PS and $CuInSe_2$ QDs.[67] The synthesis procedure involved solution-based preparation of $CuInSe_2$ QDs followed by ligand exchange and incorporation of the solid QDs within the PS layer. However, the direct spin coating of $CuInSe_2$ QDs has been employed, and it omits the ligand exchange step. The trick is to quickly add the $CuInSe_2$ QD solution in toluene instead of using only toluene as the antisolvent during spin coating.[68] SnS been used to develop $CH_3NH_3PbI_3$/SnS QD hybrid films via a facile in situ crystallization process of PSs on the surface of SnS QDs.[69] The compatibility of Sn with Pb leads to the formation of high-quality QD/PS hybrid materials and the advantage of near-infrared light absorption caused by the lower bandgap of SnS.

2.2. Integration of Quantum Dots in All Inorganic Perovskites

Although the QD/PS field started with $CH_3NH_3PbI_3$ PS, the focus was shifted to $CsPbX_3$ to further increase the stability and efficiency of the QD/PS nanocomposites. Structural defects along with instability are ubiquitous for perovskites with small chain A-site organic cations.[27,32,70,71] The stability of metal halide perovskites has been found considerably larger when the organic cation was replaced by the Cs cation along with remarkably high carrier mobility and long diffusion length due to their intrinsically higher thermal-decomposition temperature.[71–73] Cs-based lead halide perovskites are highly defects tolerant. These only could induce shallow transition levels rather than deep transition.[73–75] However, the enhanced heat tolerance and photostability of the all-inorganic perovskites gets challenged due to the formation of different phases (including black phases) and interstitial defects when external stimulation comes into play.[76] Different strategies have been adopted to overcome these problems, and which include changing of cation (B-site) and anion (X-site),[77] hydrophobic organic layer formation at the surface, alteration of solvent, etc.[76] Another way of stabilizing the α-phase of the $CsPbX_3$ perovskites is to decrease the size of the crystals to nanoscale by releasing the excess surface strain.[75,76,78] Although these strategies improved the stability to a certain extent, the strategy of capping the $CsPbI_3$ NCs with PbS to enhance the stability and optical properties of all inorganic PSNCs without damaging their semiconducting properties was proved to be quite effective.[79,80] So, for the preparation of $CsPbX_3$ and QD hybrids, the same procedure for $MAPbX_3$ and $FAPbX_3$ cannot be followed blindly. And therefore, the interface engineering to design the heterostructure is slightly different. The PbS-capped $CsPbI_3$ NCs were prepared by injecting a cesium oleate solution into a mixture of Pb^{2+}, I^-, and PbS clusters.[79] The key point was to control the growth of PbS clusters by selecting a proper S precursor, (thioacetamide; in this case) and optimizing the growth time. The shape of the PbS-capped $CsPbI_3$ PSNCs was different from the typical $CsPbI_3$ NCs' regular cubic morphology and, at some points, $CsPbI_3$ NCs connected with each other via one PbS cluster. This concomitant connection improved the charge transport within the NC film and led to better device performance. In another procedure, passivation of the PbS QDs by $CsPbI_3$ perovskite led to remarkable stability both under long-term constant illumination and storage under ambient conditions (**Figure 3**A).[80] The improved passivation significantly diminishes the sub-bandgap trap-state assisted recombination, leading to improved charge collection and therefore higher photovoltaic performance. A similar structure of $CsPbBrI_2$/PbSe heterojunction NCs was reported for the fabrication of high-performance white light-emitting diodes and red-emitting

**ADVANCED
SCIENCE NEWS**

www.advancedsciencenews.com

**ADVANCED
OPTICAL
MATERIALS**

www.advopticalmat.de
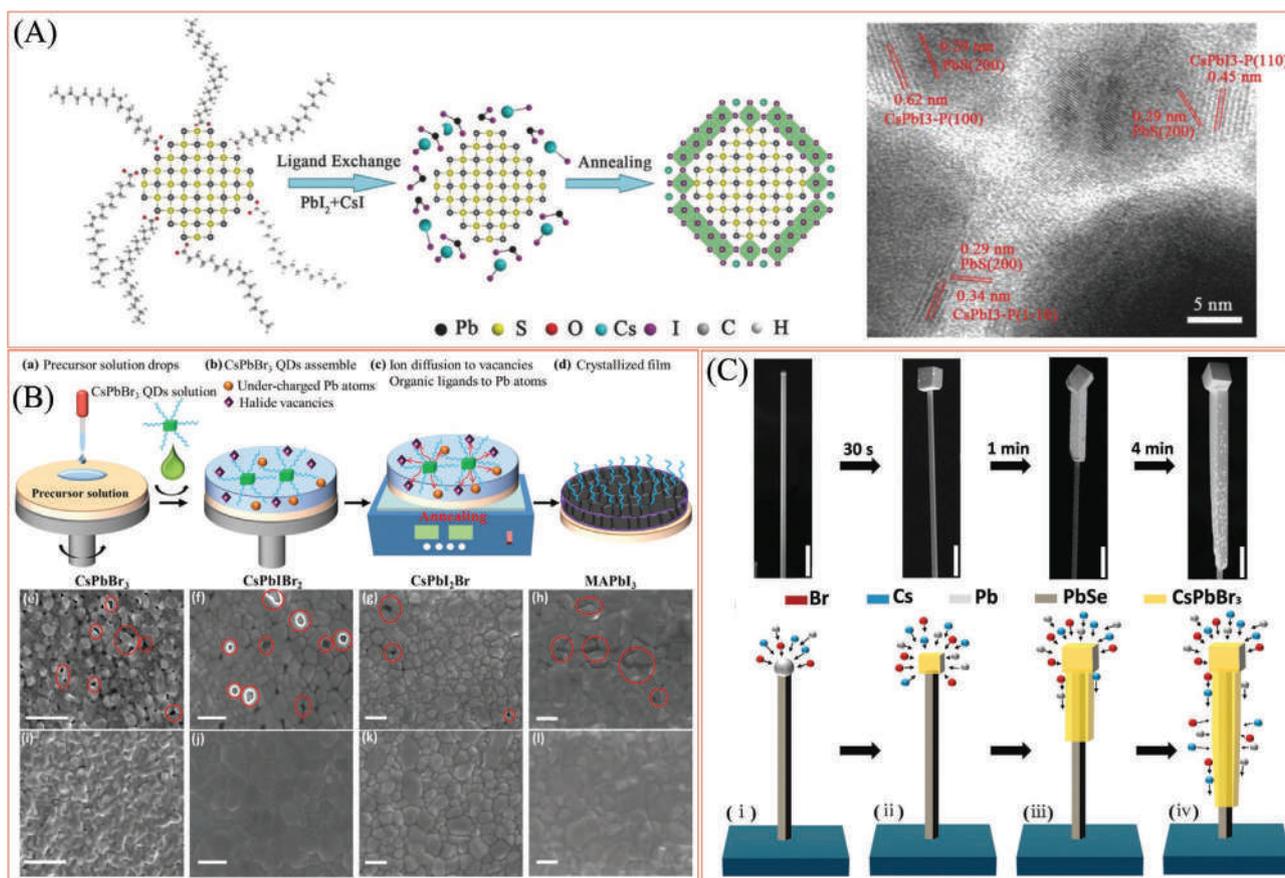
Figure 3. A) Illustration of the fabrication process of inorganic $CsPbI_3$ perovskite coating on the PbS CQD and HRTEM image of the PbS-$CsPbI_3$ perovskite based CQD. Reproduced with permission.[80] Copyright 2017, Wiley-VCH. B) Processing of perovskite films with the QD passivation treatment. a) Precursor solution is spin-coated on the substrate, then antisolvent containing $CsPbBr_3$QDs is dropped on precursor solution during the spin-coating process. b) $CsPbBr_3$QDs self-assemble on the surface of deposited films, which contain halide vacancies and under-charged Pb. c) The ions released from QDs diffuse into halide vacancies and organic ligands coordinate under-charged Pb atoms during the annealing. d) The crystallized halide perovskite film. SEM images of four kinds of perovskite films ($CsPbBr_3$, $CsPbIBr_2$, $CsPbI_2Br$, and $MAPbI_3$). e–h) without and i–l) with QD treatment. Heterogeneous spots on thin films without the QD treatment are marked with redcycles and ellipses. The scale bar is 300 nm in (e–l). Reproduced with permission.[83] Copyright 2021, Wiley-VCH. C) SEM images of the core–shell $PbSe@CsPbBr3$ wires at different growth times and schematic representation of the growth processes of the core–shell $PbSe@CsPbBr_3$ wires. Reproduced with permission.[89] Copyright 2018, Wiley-VCH.

PS LEDs under ambient air conditions.[81] The larger ionic radii of Se^{2-} anions (198 pm) compared to that of S^{2-} (184 pm) played a crucial role in inducing more lattice mismatches at the surface, and this resulted in PbSe NC-decorated QD/PS composites instead of forming a uniform shell of PbSe. In addition, the Se ratio affected the morphologies of these samples. Here, the connected NCs were also found, and they originated from the fusion of PSNCs together during the formation of a Pb–Se bond when some of the surface ligands were detached. Very recently, hybrid CdSe/$CsPbI_3$ QDs were introduced as the interfacial layer to regulate the charge transfer and energy transfer processes.[82] Recently, halide perovskite films of $CsPbBr_3$, $CsPbIBr_2$, and $CsPbBrI_2$ were coated with $CsPbBr_3$ QDs by an anti-solvent spin-coating process (Figure 3B).[83] The benefit of using the $CsPbBr_3$ QDs is threefold. First, they act as growth seeds to accelerate the crystallization and promoted larger grain crystals and improved surface morphology of the resulting films. Second, the ions of $CsPbBr_3$ passivate the vacancy defects that originated during the annealing process and finally

the self-assembly of the hydrophobic organic ligands on the surface and grain boundaries enhanced moisture stability (Figure 3B).

Tian and Rogach[84] were inspired by the previous work of Tu et al.,[81] and they understood the underlying problem behind the enhanced lattice mismatch. In all previous studies, tributyl-phosphine (TBP) was employed instead of tri-noctylphosphine (TOP), which acts as a considerably weaker reducing agent. The use of TBP resulted in water formation by reducing the carboxylic acid group of the oleic acid (OA); this directly influences the formation and optical properties of $CsPbI_3$/PbSe heterostructures. The problem with combining these two dissimilar inorganic materials is in the different capping layers. The formation of a heterojunction at the surface needs to be continuous or densely packed. Although both hybrids/composites have sufficient heterojunction points to improve the stability and performance of the individual material, it is important to form continuous heterojunction points. Thus, they developed a simple yet effective strategy for fabricating $CsPbI_3$/PbSe

ADVANCED
SCIENCE NEWS

www.advancedsciencenews.com

ADVANCED
OPTICAL
MATERIALS

www.advopticalmat.de

hybrids. In this approach, TOP served as the precursor to introduce selenium anions (in the form of TOP:Se adduct) and it triggered gradual PbSe nucleation on the exposed PS surface Pb sites, which resulted in the formation of a PbSe passivation layer.[84] However, in another study, a layer of $CsPb(Br/I)_3$ was passivated over PbSe QDs to increase the PCE of PbSe QD solar cells (QDSCs).[85] A series of mixed halide PS NCs were synthesized by tuning the ratio of $PbBr_2/PbI_2$; the solutions were then added to a sample of PbSe QDs to improve the passivation effect for PbSe QDs in solution, and this led to a superior PCE (9.2%). The introduction of the PbSe layer decreased the density of surface defects and increased the electron mobility and exciton lifetime. Inspired by the high flexibility of halide ion migration in PS materials, a unique passivation route was developed for PbSe QDs. The halide ions from these PS NCs could shuttle to defective or weaker Pb-Cl binding sites on the surface of PbSe without causing the excess removal of capping ligands owing to their similar surface conditions and absence of extra cations.[86] Passivation not only increased the air stability of the film but also improved the PCE of the PbSe QDSC by up to 8%. Recently, 2D CdSe nanoplatelet (NPL)-$CsPbX_3$ composites were developed to improve the photocurrent response. The synthesis procedure for $CdSe-CsPbBr_{1.5}I_{1.5}$, $CdSe-CsPbBrI_2$, and $CdSe-CsPbI_3$ composites involved the direct mixing of a fixed volume of CdSe NPLs from the stock solution with a desired amount of $CsPbBr_{1.5}I_{1.5}$, $CsPbBrI_2$, and $CsPbI_3$ NCs. $CsPbBr_3$/ZnS core/shell nanocrystals were designed to enhance the stability of the material and average PL lifetime.[87] The surface charge traps and grain boundaries of the PS surface were passivated by CdSe/ZnS and CdS/ZnS QDs. The CdSe/ZnS QD passivation layer on the PS materials served not only as a protective layer, but it also increased hydrophobicity to induce outstanding device stability.[43]

The nanowires of QD/PS heterostructures were synthesized in addition to the conventional morphology of QD/PS hybrids.[88,89] The slight modification of the conventional synthetic procedure resulted in a hybrid nanowire film in the last step of the synthesis: the solution containing PbS QDs, PbI_2, and CH_3NH_2I was spin-coated at 2500 rpm onto a polyethylene terephthalate film with gold contacts followed by annealing at 70 °C for 10 min under ambient conditions (relative humidity ≈ 50%). However, another method was developed to synthesize $PbSe@CsPbBr_3$ wire heterostructures through a simple CVD route (Figure 3C) wherein the $CsPbBr_3$ shell was grown epitaxially on the core of the PbSe wires prepared with self-catalyzed vapor–liquid–solid.[89]

From the literature, we learned about the synthesis of these hybrid systems. The first step is the synthesis of solution-processed QDs for designing heteroepitaxy. In this context, the hot injection method has been proved to be very useful for achieving monodisperse and high-quality colloidal QDs along with the control of the nucleation process. This method makes it easy to engineer the structure, bandgap, and morphology. The dispersibility of QDs in polar solvents needs to be achieved because the main goal is to develop a heterostructure of QD and PS. Thus, the exchange of long organic ligands with short halide ligands has proven to be considerably effective. QDs in polar solvents (DMF, butylamine, etc.) with halide ligands are mixed with PbI_2 for the in-situ epitaxial growth of PS on QDs.

QD/PS films were fabricated in the last step by soaking spin-coated halide QD films in a halide ligand/isopropanol solution.

3. Carrier Dynamics in Quantum Dot/Perovskite Systems

3.1. Perovskite Nano Crystals

In this subsection, we focus only on the photodynamics of PSNCs. While in subparagraph 3.2, we comment on the dynamics of QD/PS complex systems. A comprehensive understanding of the charge recombination and transport processes is paramount for designing highly efficient PS-based optoelectronic devices, as the optoelectronic parameters of the related devices are directly determined by these processes.[33] The dynamics of excitons and free charge carriers in PS crystals with sizes ranging from nano- to micro-scale is composed of carrier generation, transfer between neighboring crystals, and internal or interface recombination occurring within femto to nanosecond regime.[90,91] Carriers (electrons and holes in CB and VB bands, respectively) with excess energy relax via cooling processes through intra-band (electron–phonon interactions) transition pathways (**Figure 4**A).[91] Radiative transitions due to the recombination of generated electrons and holes give rise to band-edge photoluminescence (PL).[92] Self-trapped excitons attributed to lattice distortions or defect states generate broadband emission along with a delayed lifetime.[93,94] The photobehavior of the perovskite materials has been changed by modifying synthetic and post-synthetic procedures.[95–98] Based on the preparative methods, the reported trap-related recombination rates for $MAPbI_{3-x}Cl_x$ and $FAPbI_{3-x}Cl_x$ ($x = 0, 1, 2, 3$) range from ≈10 to 2×10^8 s^{-1}.[95] The contribution of the undesirable processes can be altered by varying the composition of PS materials. Modifying the composition of the lead halide PS by a combination of halide anions (I$^-$, Cl$^-$, Br$^-$) and organic/inorganic cations ($CH_3NH_2^+$ (MA), $HNCHNH_2^+$ (FA), Cs$^+$) can influence the size and crystal structure of the material.[99,100] This can change the band structure, leading to the bandgap modification. Another approach for changing the electronic structure in PS is reducing the dimensionality and size, which results in an increase in the bandgap of the system.[99] The decrease in the PS crystal size to a few nanometers can lead to a strong quantum confinement effect that manifests itself by the formation of discrete energy states.[101] Furthermore, quantum confinement can lead to a material wherein the majority of charge carriers is in the form of excitons.[102] The size-related modifications of the band structure in PS lead to changes in both time-integrated and time-resolved optical properties of PSNCs. Both absorption and emission intensity maxima shift toward shorter wavelengths, and new transitions may appear in the absorption spectra due to the increase in the bandgap upon a decrease in the size of the PSNCs.[99,103]

The photoexcitation of PSNCs with photon energy above the bandgap yields a state filling process at a higher excitonic level.[103–105] The excited system dissipates the excess energy through intraband charge carrier cooling, trapping, and interband recombination. The dynamics and spectral evolution can be recorded using femtosecond transient absorption

ADVANCED
SCIENCE NEWS

www.advancedsciencenews.com

ADVANCED
OPTICAL
MATERIALS

www.advopticalmat.de
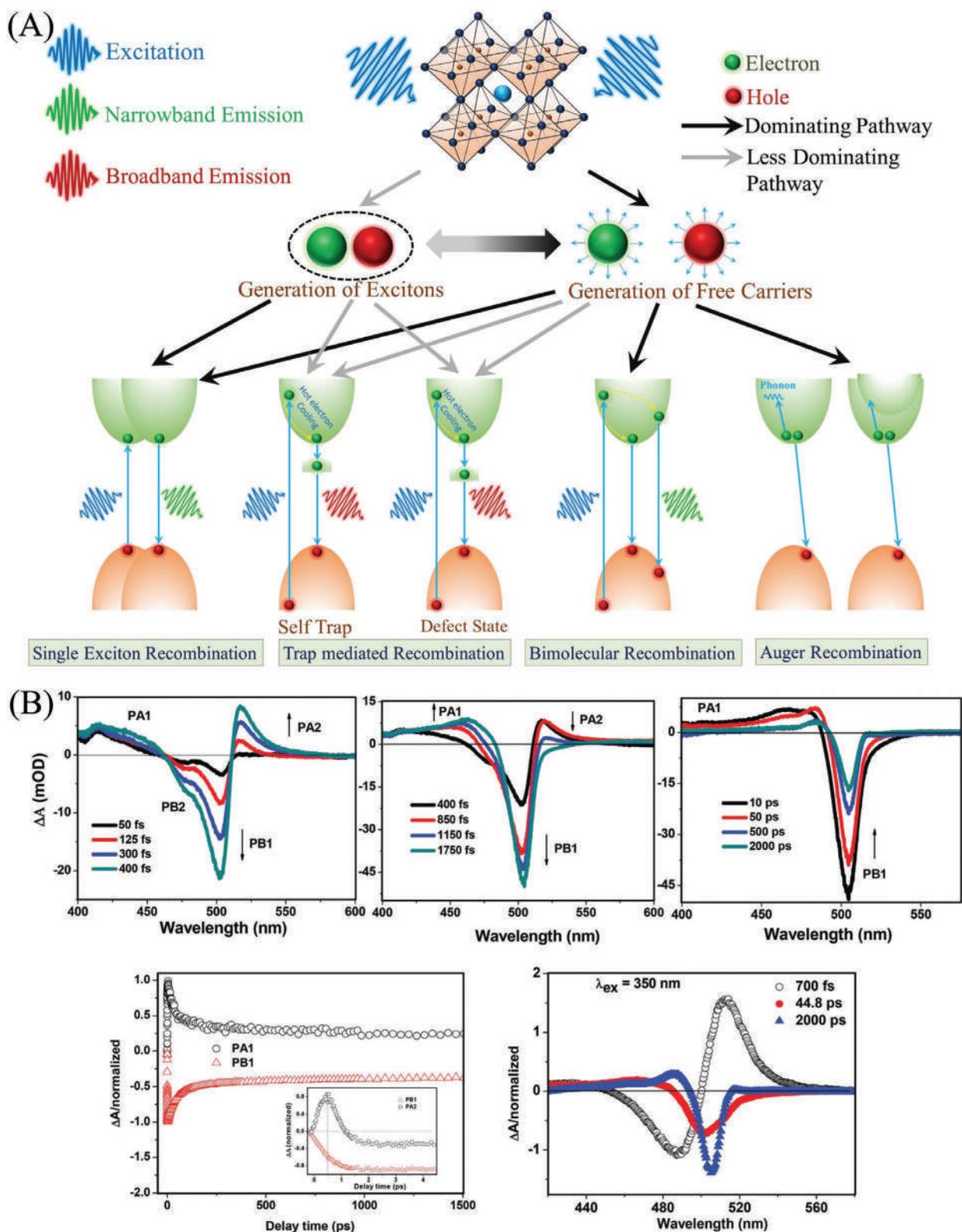
Figure 4. A) Illustration of ultrafast photoinduced processes in metal halide perovskites. B) Time-dependent evolution of the TA spectrum of $CsPbBr_3$ NCs in the short (0.05–0.4 ps, left panel), medium (0.4–2 ps, central panel), and long (10–2000 ps, right panel) time scales (upper panel). The formation and decay kinetics of PB1 (505 nm) and PA1 (465 nm) bands. The inset shows the comparison between the formation and decay dynamics of the PB1 (505 nm) and PA2 (525 nm) band, respectively. The lower panel shows the decay associated spectra of $CsPbBr_3$ NCs (lower panel). Reproduced with permission.[104] Copyright 2016, The Royal Society of Chemistry.

**ADVANCED
SCIENCE NEWS**

www.advancedsciencenews.com

**ADVANCED
OPTICAL
MATERIALS**

www.advopticalmat.de

spectroscopy. The transient absorption spectra (TAS) of the PSNCs are composed of a photo bleach band (PB, $\Delta A < 0$, A is absorption intensity) and excited state photoinduced absorption (PA, $\Delta A > 0$) (Figure 4B). The observation of the temporal evolution of PB and PA in different PSNCs provides information on the electronic states involved in the recombination processes. The rise and decay dynamics of PB and PA in the PSNCs are similar, which clearly indicate that the evolution of both bands is attributed to the same states (Figure 4B).[103–105]

The temporal evolution of the TAS was dominated by the hot charge carrier cooling process directly after excitation.[99,104–106] The TAS in CsPbBr$_3$ QDs at early pump-probe delay times below 2 ps consisted of two bleach bands (PB1 and PB2) and two photoinduced absorption signals (PA1 and PA2) (Figure 4B) because of the state-filling process of higher excitonic energy levels.[104] PB2 and PA2 disappeared within 300–700 fs owing to the carrier–carrier and carrier–phonon cooling process, whereas BB1 and PA1 were characterized by the long-time dynamics attributed to the interband relaxation of charge carriers (Figure 4B). Similar timescales of the cooling process were observed in various PS nanostructures with different compositions: CsPbBr$_3$, CsPbBr$_{1.5}$I$_{1.5}$, CsPbI$_3$, MAPbBr$_3$, and FAPbBr$_3$.[106,107] Interestingly, the increase in pump intensity and in photon energy results in slower intraband recombination because of Auger heating and phonon bottlenecks.[97,105,107,108] Two time components appear in the MAPbBr$_3$ hot-carrier cooling process. The faster time component ($\tau_1 = 1$ ps) is power independent; however, the slow component (τ_2) changes from 1.8 to 27 ps with an increasing concentration of photoexcited charge carriers. The τ_1 constant was attributed to carrier-longitudinal phonon interactions, whereas τ_2 was assigned to Auger heating.[105]

The VB and CB in PSNCs populated by holes and electrons after photoexcitation and the initial intraband relaxation may be depopulated because of charge carrier trapping, trap-assisted recombination, and bimolecular and Auger recombination. The contribution of charge carrier trapping events is predominant at low pump fluences because the density of traps is comparable to the density of photoexcited charge carriers.[103,109] Trapping events in such structures can occur because of the surface trap states owing to the high surface-to-volume ratio in QDs. Several reports have shown that halide surface vacancies are predominantly involved in trapping events in PSs.[104,110,111] The time decay of TA includes two components attributed to the direct interband recombination of electrons and holes and trapping events. The 400 ps component in the TA dynamics of CsPbI$_3$ upon excitation with a low fluence of 0.5 μJ cm^{-2} was observed on account of the trapping process.[112] A trapping time of one order of magnitude (45 ps) was provided by TA dynamics in CsPbBr$_3$ NCs upon excitation with a pump fluence of 2–4 μJ cm^{-2}.[104] Moreover, the increase it the relative amplitude of this component in CsPbBr$_3$ NCs with the decreasing intensity of the pump supports the trap-assisted origin of this process and excludes the possibility of the Auger recombination origin of the 45 ps component. Further, a 40 ps time constant was observed in the up-conversion spectroscopic results recorded at considerably lower excitation intensities (0.016 μJ cm^{-2}) than those of TA (2–4 μJ cm^{-2}), which further corroborates the trap-assisted processes in the material.

Trap states introduce undesirable recombination processes that quench the radiative recombination in PSNCs and diminish emission efficiency in the materials.[110,113] However, traps in PSNCs are related to the surface of the nanostructures and their passivation can eliminate undesirable energy states.[103,104,110,114] Further, several reports have indicated the strong effect of capping agents such as trimethylaluminum, di-dodecyl dimethyl ammonium bromide, hexylamine sulfate, or NH$_4$SCN on the emission efficiency of PSNCs.[110,115,116] The most impressive emission efficiency (PL quantum yield (PLQY) close to unity) was achieved by capping CsPbBr$_3$ NCs with NH$_4$SCN and hexylamine sulfate, which effectively removed the excess lead from the surface.[110,114] In addition, time-resolved TA and PL measurements revealed that the passivation of MAPbBr$_3$ QDs by *n*-octylamine resulted in the elimination of trap-assisted recombination.[103] The passivation of the QD surface caused the faster decay component to disappear, and both TA and PL decays were composed of one component because of the bimolecular recombination.

The excitation of PSQDs with high fluences of light yields large densities of photoexcited charge carriers; therefore, the contribution of Auger recombination becomes noticeable.[102,109] The presence of 15 ps component in the terahertz decays of CsPbBr$_3$ NCs attributable to the Auger recombination of free charge carriers was reported.[109] Wang et al. provided a different explanation for ultrafast photoinduced dynamics in CsPbBr$_3$ QDs.[102] Based on time-resolved emission studies, authors claim that excitons are responsible for the deactivation of excited states and not free charge carriers. However, it is important to note that QDs investigated in this study were smaller than those discussed earlier. Owing to the stronger quantum confinement in smaller NCs, the excitons may have become the majority charge carriers generated in the material. An increase in the light intensity led to a fast 105 ps decay component caused by Auger recombination. Only one component was present at low intensities because of the direct interband recombination. The assignment of the time components is based on three arguments. First, the authors argue that the binding energy of biexcitons of 50 meV is above the thermal energy at room temperature, which ensures the survival of the biexciton state. Second, the large biexciton binding energy produces a remarkable shift in the stimulated exciton band toward longer wavelengths compared to spontaneous emission. Finally, the quadratic dependence of the SE band intensity on the pump fluence upon excitation with a 5 ns pulse SE confirms the biexcitonic nature of the phenomena.

An easy and effective method for modulating the optical properties of PSNCs is the intentional doping of their lattice with heteroatoms; this has a negligible influence on the host crystal structure. The compositional engineering of PSQDs by the introduction of the main group metal cations, transition metal cations, and rare earth metal cations has been presented in several reports.[117–119] Such modifications can lead to the appearance of new radiative transitions, increase emission efficiency, and decrease the contribution of trapping events in doped nanostructures.[117–121] The discussion of metal-doped PSQDs is beyond the scope of this review, and it will not be discussed in detail.

3.2. Carrier Dynamics in Different Quantum Dot/Perovskite Systems

The combination of lead trihalide PSs of different dimensionality (3D, 2D, 1D, and 0D) with various materials aims to improve the stability of PS-based materials, enhance their PLQE, or acquire more effective charge carrier separation based on the desired application.[112,122–125] To accomplish these goals, both bulk and nanostructured PSs were combined with metal chalcogenide QDs (PbS, CdS, CdSe), black phosphorus quantum dots (BPQDs), and GQDs.

However, two different scenarios can arise: 1) The band gap of the QD is larger than that of the PS (**Figure 5**A) and 2) the band gap of the QD is smaller than that of the PS (Figure 5B). The presence of chalcogenide QDs with a band-edge emission range greater than that of the PS itself has been found to be successful for effective charge separation and bimodal radiative recombination. The processes involve charge carrier transport from the QDs to PSs or from PSs to QDs and the interface, followed by exciton recombination at the PS and QD, and the recombination of the transferred charges at the PS and QD.

Chalcogenide QDs are attractive materials for PV devices owing to the easy tunability of the bandgap across a wide range of energies and high light absorption coefficients (**Figure 6**A). The combination of these materials with lead trihalide PSs can help overcome the limitations of each component, which

enhances the performance of PV devices.[126] Therefore, materials composed of PSs and chalcogenide QDs have grown into the most extensively studied hybrid systems, surpassing mixtures with BPQDs or GQDs. Considering the importance of different nanomaterials, our discussion of PS-based nanocomposites begins with the description of PS nanocomposites with chalcogenide QDs followed by BPQDs and GQDs containing ones.

3.2.1. Pb Chalcogenides in Perovskites

Among all metal chalcogenides, PbS nanostructures have gained considerable attention as their crystal lattice matches with the PS structure that prevents the formation of an unstructured or highly disordered PS layer on the QD/PS interface.[45] The conformity of PS and PbS QD crystal lattices along with the tunable optical properties of PbS nanostructures makes their mixtures the most extensively researched PS-based composites.[45,62,127,128] The materials composed of PSNCs and PbS QDs show dual emission in the visible and NIR regions because of the respective PSs and PbS components. Dual emission in PbS/MAPbI$_3$, PbS/CsPbBr$_3$, and PbS/CsPbCl$_3$ QDs has been reported in several studies (Figure 6B).[45,58,122,] The combination of PbS QDs and PSQDs results in a material wherein the photoexcited charge carrier can migrate between
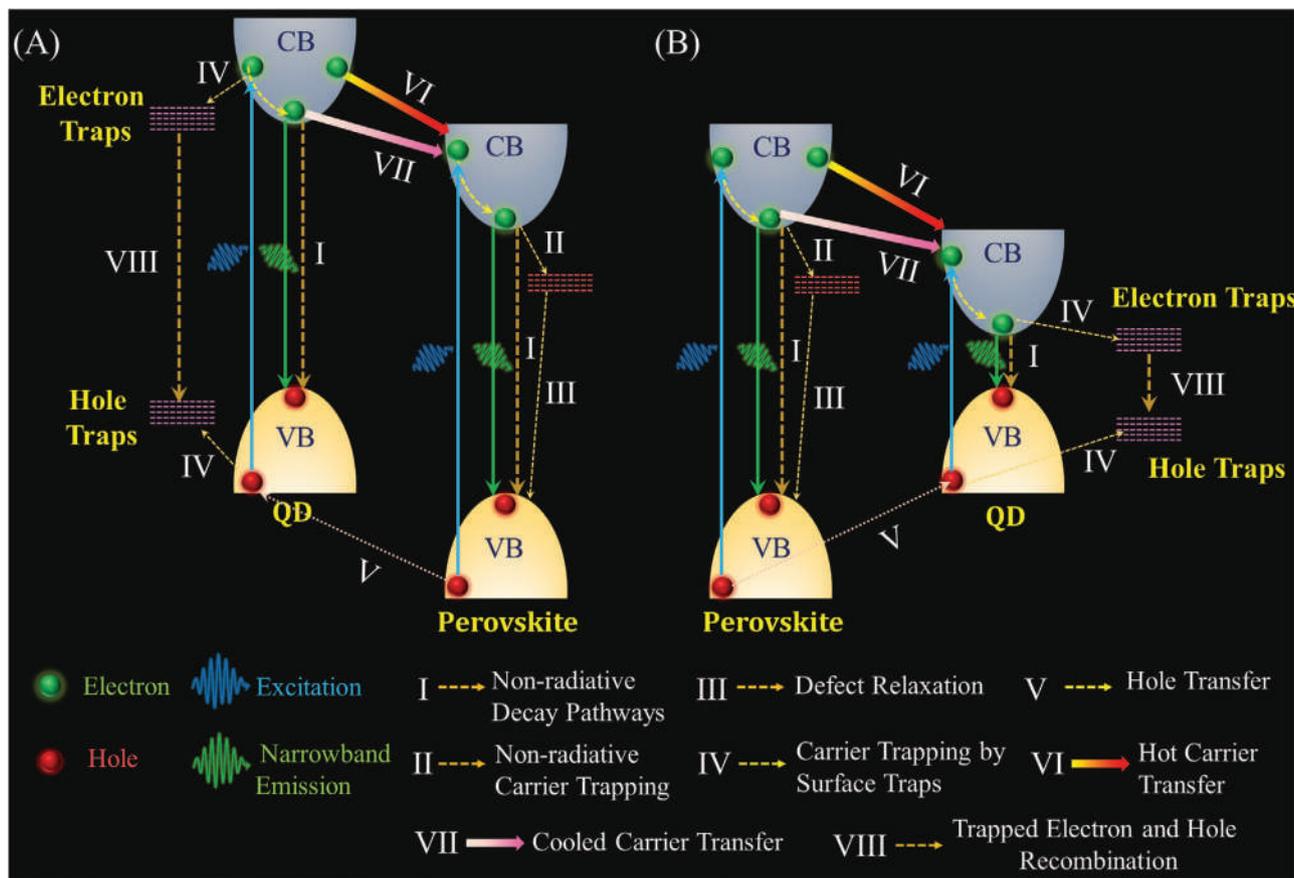
Figure 5. Schematic presentation of the charge carrier dynamics in a QD/PS composite with two distinctive situations where charge transfers from A) QDs to PS and B) PS to QDs.
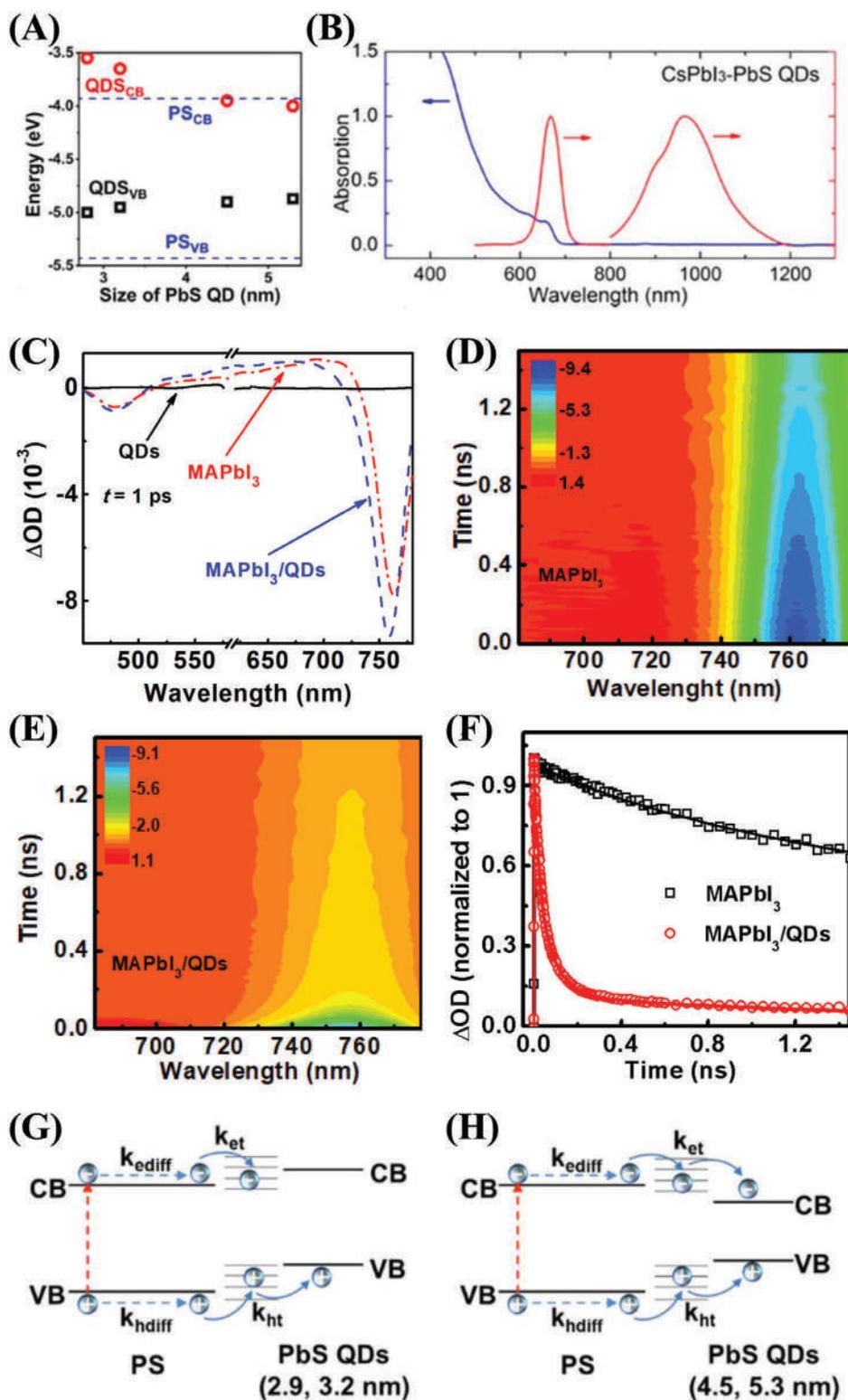
Figure 6. A) Positions of VB (■) and CB (○) for PbS QDs of different sizes and for bulk MAPbI$_3$. Reproduced with permission.[126] Copyright 2020, The Royal Society of Chemistry. B) Absorption and dual emission of PbS/CsPbI$_3$ heterostructural QDs. Reproduced with permission.[122] Copyright 2020, The American Chemical Society. C) Femtosecond transient absorption spectra of MAPbI$_3$ and PbS/MAPbI$_3$ QDs composite at 1 ps pump-probe delay time. 2D pseudo-color map of D) MAPbI$_3$ and E) PbS/MAPbI$_3$ QDs. F) Comparison of TA decays of pristine perovskite and composite at 760 nm observation wavelength. Reproduced with permission.[129] Copyright 2018, Elsevier. Scenarios of photoinduced hole and electron diffusion and transfer to QDs of different sizes. G) The electron transfer to the CB in QDs of 2.9 and 3.2 nm is precluded. H) The electron transfer to the CB of QDs of 4.5 and 5.3 nm is allowed. Reproduced with permission.[121] Copyright 2020, The Royal Society of Chemistry.

ADVANCED
SCIENCE NEWS
www.advancedsciencenews.com

ADVANCED
OPTICAL
MATERIALS
www.advopticalmat.de

components. It was observed that the PLQY of PbS embedded in $CsPbBr_3$ NCs increased from 0.67% to 18.4% because of the efficient electron transfer (87%) from $CsPbBr_3$ to PbS.[122] The femtosecond TA measurements of this system revealed that the presence of PbS results in an acceleration of the bleach band decay attributed to the energy transfer from PSNCs to PbS QD. The observation of the signal related to PbS QDs indicated that the exciton lifetime in PbS significantly increased in the composite as compared to neat PbS because of the exciton transfer from $CsPbIBr_3$ NCs to PbS QDs. The exciton and hole transfer from PSNCs to QDs is driven by the lower energy of the VB and the higher energy of the CB edge in PbS compared to those in $CsPbBr_3$.

Efficient charge carrier transfer from PSs to PbS QDs was observed in nanocomposites composed of PbS QDs embedded in a bulk $MAPbI_3$ matrix.[126,129] First, PbS/$MAPbI_3$ QDs thin polycrystalline films containing various concentrations of QDs (3 nm in size) were fabricated by femtosecond TA spectroscopy.[129] Interestingly, the interaction of the guest material with $MAPbI_3$ influenced the crystal structure of the host, and this was manifested by a slight blue shift of the TAS in the nanocomposite (Figure 6C–E). In addition, bleach band dynamics at the 760 nm observation wavelength were attributed to charge carrier generation and recombination in $MAPbI_3$, which increased significantly in the presence of PbS QDs (Figure 6F). For the composite material containing 3.0 nm QDs, only the edge of the VB in PbS QDs was located below that of the bulk $MAPbI_3$. Therefore, the hole and not the electron needs to be transferred efficiently to the host (Figure 6A,G). The ultrafast decay of the TA signal in the PbS/$MAPbI_3$ QDs suggested that electrons were efficiently transferred to the quest material because electrons are trapped in the surface trap states of PbS QDs. Further, the authors concluded that TA dynamics in nanocomposites are attributed to the temporal evolution of photoexcited charge carriers in two different regions: areas affected and unaffected by PbS QDs. Later work on PbS QDs embedded in bulk $MAPbI_3$ showed the temporal evolution of photoinduced charge carriers in composites containing QDs of different sizes. The utilization of the PbS of 2.9–5.3 nm in size allowed studying the electron and hole transfer processes of the systems wherein the energies of the CB edges in PbS QDs reduce to values below that in $MAPbI_3$ (Figure 6G,H).[126] This means that in the case of larger QDs, electron transfer from the CB of MAPbI3 to the CB of PbS QDs is possible. The authors separated the electron and hole diffusion and transfer times using femtosecond TA and terahertz spectroscopies and by fitting the results with the physical model. The transfer rate constants of electron (k_{et}) and hole (k_{ht}) are similar ($\approx 0.1 \times 10^{10}$ s^{-1}) in the case of 2.9 nm QDs, and they increase to 0.78 and > 1430 s^{-1} in composites containing 5.3 nm QDs. Both reports recommended the contribution of excitons to the processes of charge carrier generation.

The efficient transfer of photoexcited charge transfer from the PS matrix to PbS QDs was demonstrated by the results of PL studies on PbS/$MAPbBrI_2$ nanocomposites.[123] The increase in the concentration of QDs embedded in the PS matrix from 0% to 50% resulted in a drastic reduction in the emission intensity related to the host material caused by the charge carrier deactivation through transfer into PbS QDs. The decrease

in emission intensity was accompanied by an acceleration of the radiative recombination lifetime; this supports the presence of charge carrier transport. The examination of QD emission while excited in the range of PS absorption indicates an increase in its intensity with increasing concentration of QDs because of the improved QD ordering and better oriented PS domains, which can promote more effective energy transfer.[130] However, the emission intensity decreases for QD concentrations above 30% because of a more uneven QD landscape that leads to a different distribution of PS domains, compromised QD passivation, and enhanced inter-dot interactions.[123]

For $MAPbI_3$ shelled PbS QDs films, power-dependent photocarrier radiometry measurements showed that trap-mediated exciton transport between PbS QDs occur in this system.[131] The existence of shallow trap states at the interface between the host and guest (activation energy 34–41 meV as related to PbS QD CB energy) was confirmed. Further, the modeling of experimental data allowed the extraction of several system parameters such as exciton lifetime, hopping diffusivity, separation energy between dark and bright states, and carrier trapping rate.

3.2.2. Cd Chalcogenides in Perovskites

Transient absorption studies and theoretical calculations of chloride, OA, CdS, or $MAPbI_3$-passivated PbS QDs of two sizes indicate the strong contribution of unvented intradot Auger processes to the recombination processes in composite materials.[127] However, the authors demonstrated that the synthetic approach significantly inhibited Auger recombination. The Auger recombination rate decreases by up to one order of magnitude because of the bandgap alignment between the core and the shell.[127] Furthermore, three different types of Auger recombination were observed: i) Intradot, ii) trap-assisted, and iii) diffusion-assisted. The effects of both passivation and excitonic mode delocalization showed an impact on Auger recombination. However, only modal delocalization significantly affected intradot Auger recombination. The passivation of QDs with Cl and CdS resulted in a relatively small increase in the Auger lifetime compared to OA-capped PbS because of the elimination of surface trap states and consequently trap-assisted Auger recombination. In the case of $MAPbI_3$ passivated PbS QDs, the increase is considerably larger (approximately one order of magnitude) because of the wave-function delocalization in the core.

Efficient charge carrier transfer between the two components is possible because of the adequate positions of the conduction and valence bands in $CsPbBr_3$ NCs and CdSe QDs or CdSe/CdS core–shell QDs.[132] As the VB edge in $CsPbBr_3$ NCs is located below that in CdSe and CdSe/CdS QDs, the hole can be transferred into the former. The energy of the CB edge in PS NCs is located at higher energy than the CB energy of CdSe and CdSe/CdS QDs; thus, electron transfer occurs from PSs to QDs. Indeed, the comparison of time-integrated PL spectra and time-resolved up-conversion emission and transient absorption decays in PSNCs/CD QD systems suggest efficient electron transfer between the two systems. The emission bands related to PSNCs (487 nm) and CdSe QDs (600 nm) are strongly quenched in the mixture of both materials owing

to the efficient and fast charge carrier separation. Surprisingly, in the PSNCs and CdSe/CdS QD mixture, only the emission of the PS component is strongly reduced, which clearly indicates that the hole transfer to the former is restricted because of the presence of the CdS shell. In agreement with the time-integrated emission, the acceleration of the up-conversion emission and transient absorption decays in composites indicates efficient charge transfer. The photoexcited electron transfer from CsPbBr$_3$ NCs to CdSe QDs and CdSe/CdS core–shell QDs was calculated to be 550 and 650 fs, respectively. The hole transfer from photoexcited CdSe QDs to PS NCs was 750 fs.

Interestingly, a change in the dimensionality of CsPbBr$_3$ and CdSe NCs significantly influences the process of electron transfer from the former to the latter.[133] Bromberg et al. investigated the impact of 0D and 2D nanostructures on the optical properties of their composites; they found that the electron transfer from PSs to CdSe in the composites composed of 2D nanostructures is faster than that in the mixtures of 0D structures, which manifests itself by the distinctive acceleration of PL decays in the studied materials. In some cases, the combination of metal chalcogenides with PSs led to materials being characterized by improved uniformity and operational stability, narrow-band emission, and enhanced PLQY.[125] Further, capping CsPbBr$_3$ QDs with a CdS shell reduces nonradiative Auger recombination, which leads to higher amplified spontaneous emission compared to noncapped PSQDs; the relative efficiency increases by over 130%. The authors concluded that the capping of PSQDs with a CdS shell reduced the number of deep electron and hole surface traps.[125] Surface trap passivation in thin polycrystalline MAPbI$_3$ films was observed due to CdSe/ZnS QD layer deposition on top of the PS film.[43] The CdSe/ZnS QD layer additionally served as a protective layer and augmented the hydrophobicity of the composite material.

3.2.3. Green (Free from Pb and Cd) Quantum Dots in Perovskites

Carbon-Based Quantum Dots in Perovskites: GQDs are a group of materials that display promising charge carrier separation and transport features.[134–136] The great advantage of GQDs lies in the possibility of tuning the highest unoccupied molecular orbital (HOMO)/lowest unoccupied molecular orbital (LUMO) energy by the chemical modification of these nanostructures. Research on CH$_3$NH$_3$PbI$_3$-based solar cells with and without a GQD layer showed that the presence of carbon-based materials causes significant quenching of the emission intensity in the absorber (**Figure 7**A). The electron is transferred to TiO$_2$ in both solar cells, and therefore, the 75% reduction of the emission band in the solar cell containing GQDs is attributed to the more efficient electron injection into the hole-transporting layer (Figure 7B).[135] The reduction in the emission intensity in similar systems caused by GQD addition is in agreement with other reports.[134,136] The enhanced proficiency of electron transfer in solar cells comprising GQDs (TiO$_2$/GQDs/PS) compared to those lacking carbon-based material (TiO$_2$/PS) was established by the acceleration of emission and TA decays in the former (Figure 7C,D).[135] The improvement in the charge carrier extraction efficiency in the PSCs containing GQDs was

attributed to a two-step electron transfer between PS and TiO$_2$. First, the electron is transferred from the PS and GQDs, and in the next step, to TiO$_2$ (Figure 7E,F). The TA decay analysis indicated that the presence of GQDs decreased the PS → TiO$_2$ electron injection time from 260 to 307 ps in TiO$_2$/PS to 90–160 ps in the TiO$_2$/GQDs/PS system.[135]

Black Phosphorus Quantum Dots in Perovskites: BPQDs have been found to be good candidates for charge carrier extraction materials from PS materials. The application of a nanocomposite composed of a BPQD layer deposited on a FA$_{0.85}$MA$_{0.15}$PbI$_{2.5}$Br$_{0.5}$ PS thin film in a plastic solar cell resulted in a 3.15-fold enhancement of efficiency (11.26%) compared to the device without the BPQD layer.[137] This impressive improvement is attributed to more effective electron extraction from the PS material into BPQDs. The increase in the electron extraction efficacy is proven by the distinctive reduction in the intensity of the PS emission band and the shortening of the emission lifetimes form τ_1 = 6.8 and τ_2 = 198.2 ns in pure PS to τ_1 = 4.3 and τ_2 = 27.6 ns in the BPQDs/PS nanocomposite material. Interestingly the increase in the dimensionality of black phosphorus nanosheets interacting with CsPbBr$_3$ QDs capped with organic ligands (OA, oleylamine, siloxane ligand 3-aminopropyltriethoxy-silane with glutaric anhydride, benzylamine (BA), and benzoic acid (BZA))results in even larger reduction of emission lifetime, and thus, in more efficient electron transfer.[138] Earlier studies on PSQDs covered by BA and BZA showed charge carrier transfer in these systems.[139]

Interestingly, it was shown that BPQDs can be used as seed-like sites to modulate the nucleation and growth of CsPbI$_2$Br and MAPbI$_3$ PS films.[140,141] Perovskite nanocomposite films formed in the presence of BPQDs are characterized by high crystallinity and fewer nonradiative defects compared to pure PS material (**Table 1**). Therefore, this increases the emission efficiency and excited charge carrier lifetime in the BPQD/PS material. Yang et al. showed that the emission lifetime increased from 78 ns in pure PS to 95 ns in BPQD/PS.[141]

4. Application

4.1. Quantum Dot/Perovskite Hybrid Solar Cell

Semiconductor nanostructured architectures that exhibit quantum properties in PV applications have attracted considerable research interest in the last two decades. Semiconductor QDs have been exploited as light-harvesting materials to design low-cost third-generation solar cells owing to their properties such as the ease of bandgap tunability, high absorption coefficient, low-cost preparation, and potential to generate multiple excitons.[20,142–144] Devices comprising QDs as light-absorbing material have shown excellent potential regarding room temperature stability and ease of device fabrication in a larger scale. Different strategies such as the formation of core/shell structures and surface engineering to reduce surface trap states and improve carrier transport in addition to computational studies have increased the PCE of QD-based third-generation solar cells to 18.1%.[26,145–148] Due to lack of proper bandgap absorbers and electron–hole transport materials, people are
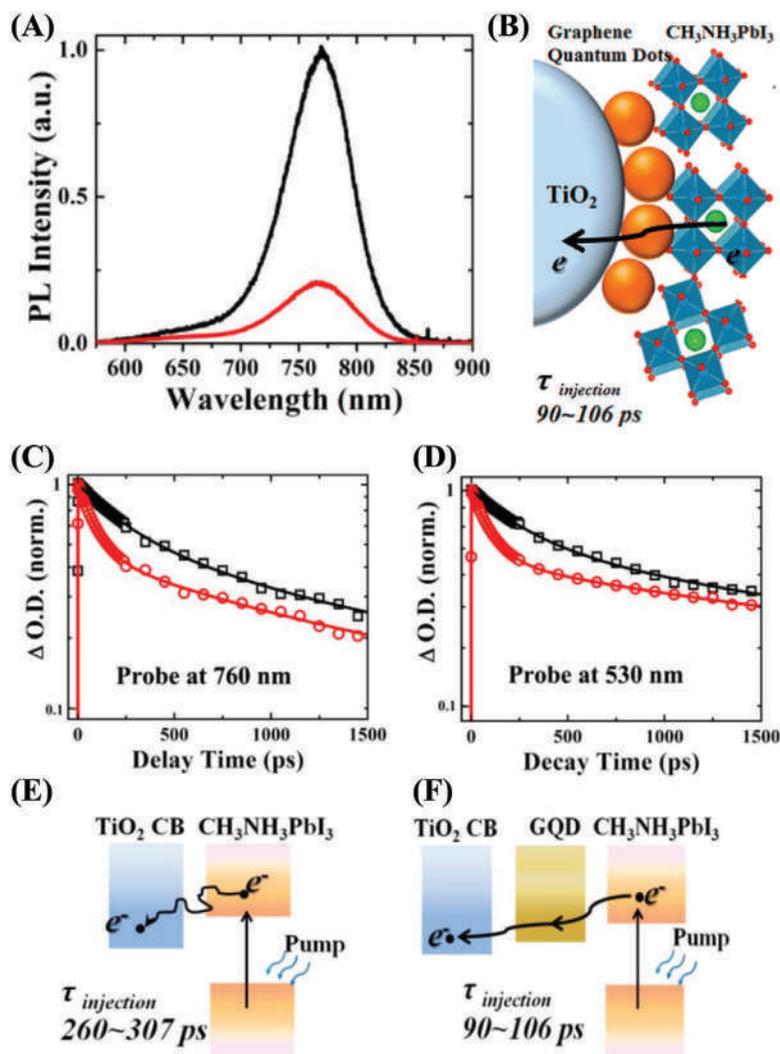
Figure 7. A) Photoluminescence spectra of TiO_2/PS (black line) and TiO_2/GQDs/PS (red line). B) Illustration of the electron transfer in TiO_2/GQDs/PS. C,D) Transient absorption decays of the bleach band (at 760 nm) and photoinduced positive absorption (at 539 nm) in TiO_2/PS (black squares and line) and TiO_2/GQDs/PS (red circles and line). Illustration of the electron transfer in E) TiO_2/PS and F) TiO_2/GQDs/PS. Reproduced with permission.[135] Copyright 2014, The American Chemical Society.

finding it is difficult to overcome the issues and challenges associated with the development of efficient QDSCs, despite single-junction QDSCs being considerably more stable than PSCs.[146,149] In terms of PCE QD based solar cells lack far behind the bulk PSCs. Over the last eight years, rigorous research on the development of PSCs has boosted their PCE to 25.5% (29.5% in tandem architecture) from 3.8%, and this value continues to rise.[26,150–153] The effectiveness of PSCs lies in the fact that organic–inorganic hybrid PSs can act both as an absorber and an efficient CTL because of their high optical absorption properties (greater than 105 cm^{-1} attributed to s-p antibonding coupling), excellent charge-carrier mobility (800 cm^2 Vs^{-1}), longer exciton diffusion length ($\approx$1 μm), low exciton binding energy (less than 10 meV), high PLQY(as high as 95%), high carrier lifetime (exceeding 300 ns), and tunable bandgap.[154] The cost-effectiveness and easy fabrication compared to silicon solar cells further support their increasing use for converting solar energy into electrical energy.

4.1.1. Perovskite Solar Cell Architectures: Configurations and Challenges

PSC device architectures can be classified into three types: mesoporous n-i-p, planar n-i-p, and planar p-i-n. Regular PSCs are configured by a transparent conductive oxide/ blocking layer (ETL)/PS absorber layer/HTL material/gold (Au) (**Figure 8**A).[155]

In the mesoporous n-i-p architecture, an intermixed layer formation is governed by the infiltration of PS materials into an ETL scaffold with nanoscale pores. The device stack is completed by depositing an HTL over the PS and the evaporation of the top electrode. The use of a mesoporous layer suppresses the photocurrent–voltage (J–V) hysteresis phenomenon in the PSCs by enhancing the charge separation, which leads to a PCE of 22.1%.[26] However, in the planar n-i-p PSC architecture, a compact ETL can be found instead of an intermixed layer directly attached to the PS layer. Direct attachment favors

ADVANCED
SCIENCE NEWS
www.advancedsciencenews.com

ADVANCED
OPTICAL
MATERIALS
www.advopticalmat.de

Table 1. Reported effects of the QDs on the charge carrier dynamics of PS systems.

Type of QDs	QD	Photoinduced processes	Reference
Pb chalcogenide	PbS	Efficient charge carriers from PS to PbS QDs	[122,123,126,129–131]
		Acceleration of free charge carriers transition with PbS QDs size due to VBs and CBs alignment between two components	
		A strong influence of interfacial trap states on the free charge carriers transfer	
		Trap mediated exciton transport	
Cd chalcogenide	CdSe	Efficient charge carriers transfer between the components due to adequate positions of VBs and CBs in PS and CdSe	[125,127,132,133]
		Electron is transferred to PS while hole to CdSe	
Green QDs	CQD	Enhancement of electron transfer efficiency to electron transporting layer	[134–136]
	BPQD	Efficient electron extraction from PS to black phosphorus materials	[137–139]
		Acting as seed-like sites, the black phosphorus nanostructures improve the optical quality of PS materials	

the scaling-up process, and this structure has recently shown high-efficiency performance with negligible hysteresis. In this architecture, carbon or gold electrodes are used directly instead of the HTL, which favors the scaling-up process.[153] The planar p-i-n architecture refers to the inversion of carrier extraction layers compared to the n-i-p configuration (Figure 8B).

The rapid transition of this PSC technology at the industrial scale requires a proper route to scale up the synthesis and fabrication procedure as PS films and devices are extremely sensitive to PS deposition conditions, and film drying procedures can significantly affect the morphology of PSs. Strategically incorporating semiconductor QDs within PSs can boost the PV performance of PSCs; most importantly, it can boost device stability. The advantages of incorporating QDs is five-fold: i) QDs can act like a seed or heterogeneous nucleation centers to facilitate the uniform, pinhole-free high-quality large-grain PS film formation; ii) QDs enhance the light-harvesting ability by absorbing the short-wave infrared part of the solar spectrum; iii) they can serve as both ETL and HTL materials for the rapid extraction of charge carriers; iv) QDs can reduce the surface trap concentration of the PS films, which prohibits

charge carriers from rapid radiative recombination and residing at the surface traps, thereby increasing efficiency; and v) most importantly, incorporation of QDs increases the stability of the PV devices.

One interesting synergistic effect of adding the embedded QDs into halide PS layers is their role as seed promoting and helping in the crystallization of the halide PS layer and the final photoconversion efficiency of the PV devices.[62,69] The efficiency of the PSC with the addition of embedded QDs depends not only on QD concentration but also on the surface nature of QDs.[48]

4.1.2. Quantum Dot/Perovskite as the Absorber Layer

The extraordinary PCE of the PSCs generally originates from the minimized charge recombination effects inside the absorbing layer and good interfacial contact with the charge extraction layers. However, the surface defect can act as a poison to facilitate non-radiative recombination resulting decrease in charge carrier lifetimes. The key to excellent photo-carrier diffusion is the efficiency of converting photoelectrons
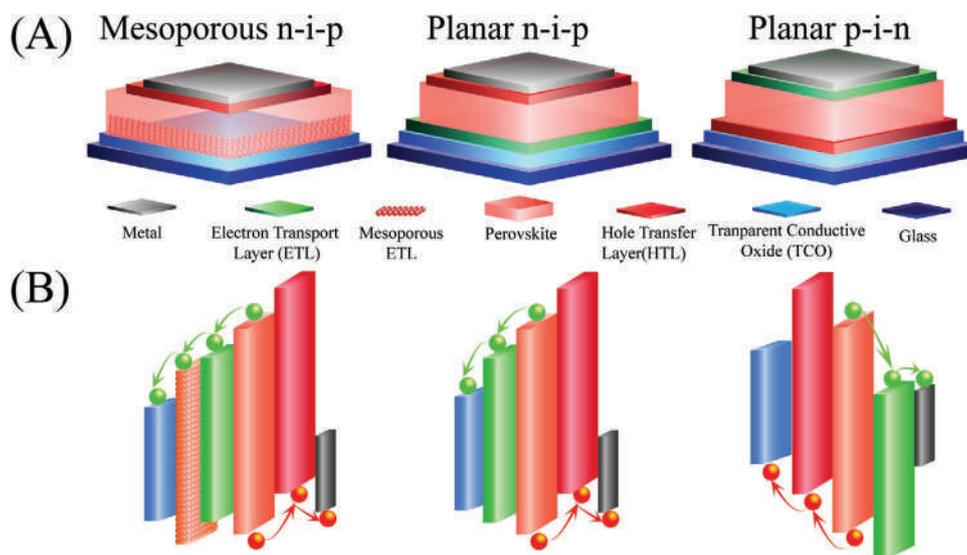
Figure 8. A) Schematic illustrations of the layered structures of three typical perovskite solar cell architectures: mesoporous n-i-p, planar n-i-p and planar p-i-n. B) Illustration of the energy band diagram showing how different perovskite solar cells operate.

ADVANCED
SCIENCE NEWS
www.advancedsciencenews.com

ADVANCED
OPTICAL
MATERIALS
www.advopticalmat.de

and holes generated at the PS surface to excitons. QD passivation has a vital role to play in this regard. The introduction of QDs with low trap densities in PSCs reduces the overall surface defect concentration in the films facilitating charge separation, improves conductivity, enhances unidirectional charge flow along with superior light-harvesting, and finally, results in the enhancement of device stability and efficiency.

Pb Chalcogenides in Perovskite Layers: The addition of embedded QDs into the halide PSs matrix is an effective method to significantly increase the stability of the black PS phase.[156] PbS QDs are the most studied systems in this regard as PbS has the lowest lattice mismatch with MAPbI$_3$ (<5%) and CsPbBr$_3$ (~0.5%) perovskites, which basically ensures high-quality epitaxy with low strain. In this context, the stabilization of FAPbI$_3$ layers presents a major challenge to increase the performance of a single-absorber PSC because FAPbI$_3$ has the narrowest bandgap,[156] the closest one to the bandgap that can provide the maximum theoretical efficiency considering the Shockley–Queisser limit.[157] However, the size of FA is slightly larger than cation sizes that allow the stabilization of the PS phase (α-phase); the stable phase of FAPbI$_3$ at room temperature is hexagonal (δ-phase). Although the α-phase presents the desired narrow bandgap (black phase), the δ-phase is not photoactive with a broad bandgap (yellow phase). The instability of the FAPbI$_3$ black phase is conventionally solved by the addition of cations with a size smaller than FA, such as Cs and/or methylammonium.[158] Nevertheless, this strategy has a drawback in that the bandgap of the resulting PS increases while

moving away from the maximum theoretical efficiency for Pb-based halide PSs. In this context, adding PbS QDs to a pure FAPbI$_3$ layer with an optimized concentration and size can preserve the FAPbI$_3$ black phase (**Figure 9**A).[53] This stabilization has an essential effect on the performance of solar cells fabricated with FAPbI$_3$. Photoconversion efficiency and solar cell reproducibility were enhanced with the addition of QDs (Figure 9B).[53] The stability of the device stored under ambient conditions with no encapsulation increases significantly (Figure 9C).[53] The beneficial effect in terms of stability enhancement is limited to pure FAPbI$_3$ and other halide PSs such as FACsPbI$_3$. Nonencapsulated solar cells fabricated with FACsPbI$_3$ with embedded PbS nanoplatelets preserved their photocurrent after 4 months of storage under ambient conditions compared to a clear decrease observed for samples with no additives (Figure 9D,E).[54] This stability enhancement was observed again when harder ageing conditions were applied, for example, thermal annealing at 70 °C and 55% RH (Figure 9F).[54] No significant effect was noted in the samples containing embedded PbS nanoplatelets, whereas a continuous performance decrease was observed for FACsPbI$_3$ with no additives. Very recently the same group has reported also a significant increase of the T80 parameter, the time in which the efficiency drops to 80% of the initial value, of pure FAPbI$_3$ solar cells when cells were fabricated in air.[159] T80 increases from 21 (for devices fabricated in N$_2$) to 112 days (for solar cells fabricated in the ambient atmosphere). Interestingly T80 reaches 145 days if PbS quantum dots (QDs) are introduced as additives in air-prepared
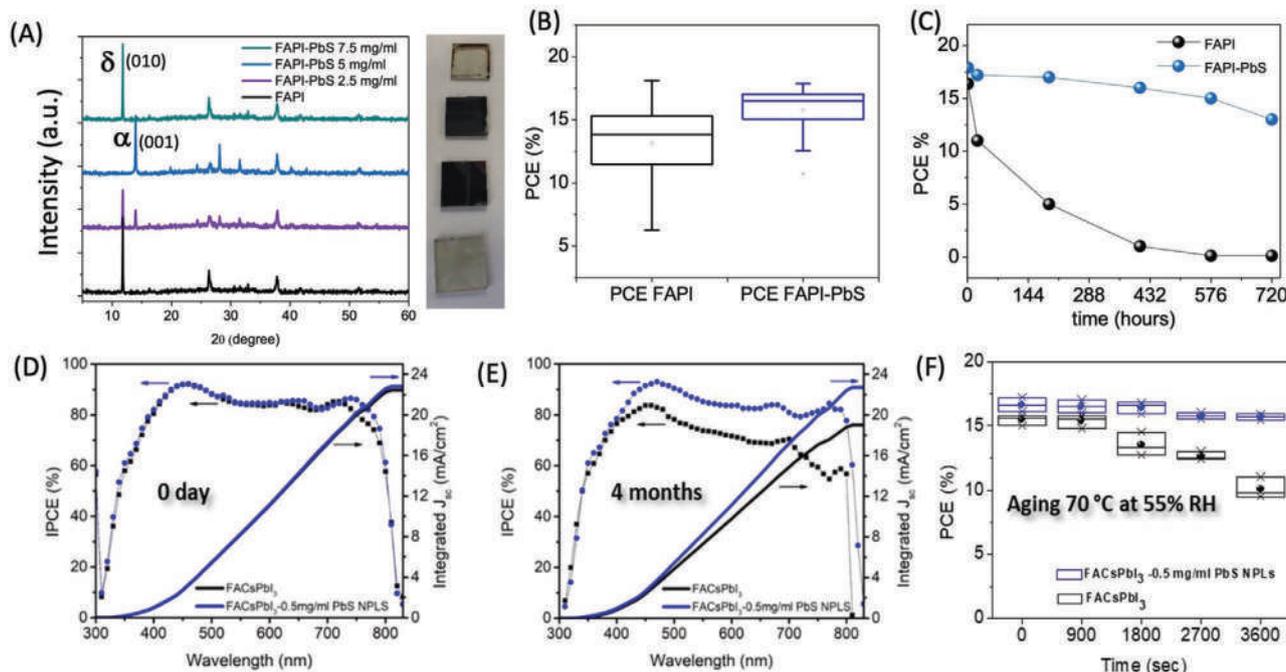
Figure 9. A) X-ray diffraction patterns of FAPbI$_3$ (FAPI) layers without and with different concentrations of embedded PbS QDs 30 days after the synthesis and storing at ambient conditions. The pictures show that the predominant black or yellow phase can be distinguished by bare eyes. B) Statistical distribution of photoconversion efficiency (PCE) of pure FAPI and FAPI-PbS composites. C) Stability of PCE of FAPI and FAPI-PbS stored at ambient conditions. Reproduced with permission.[53] Copyright 2020, The American Chemical Society. D) Comparison of the incident photon to current efficiency (IPCE) for fresh FACsPbI$_3$ and FAPbI$_3$ + PbS nanoplatelets samples. E) Comparison of the same samples after 4 months storing at ambient conditions. F) Effect of an annealing at 70 °C and 55% RH on the PCE of FACsPbI$_3$ and FAPbI$_3$ + PbS nanoplatelet samples. Reproduced with permission.[54] Copyright 2020, Wiley-VCH.

FAPI PSCs. On the other hand, the performance of the solar cells depends on the concentration of PbS QDs embedded in the $FACsPbI_3$ matrix, but for all the analyzed concentrations and increase of stability respect devices without QDs was reported.[159] The combination of halide PSs and semiconductor QDs presents a high interest in developing advanced solar cell configurations as intermediate-bandgap solar cells.[46,58,160]

Incorporation and passivation of PbS QDs in perovskite matrix have proved to be quite successful in terms of stability and efficiency.[49,53,62,80,161–165] Initial PCE of 4.92%[49] has been boosted to ~ 21%[165] in 4 years.

Cd Chalcogenide in Perovskite Layers: Apart from PbS QDs CdSe/ZnS[43] QDs have also been employed for the passivation. CdSe/ZnS QDs effectively passivated the surface charge traps and grain boundaries of the perovskite materials to reach an outstanding efficiency close to 20%, along with a suppressed hysteresis in the *J–V* characteristics.

Perovskite Quantum Dots in Perovskite Layers: Deposition of $CsPbBr_3$ QDs over $CsPbIBr_2$ PS film suppressed light-induced phase segregation and degradation which increased the PCE by over 11% from 8.7%.[83] Integrating a small amount of ligand-capped $CsPbBrCl_2$ QDs within $MAPbI_3$ layer improved the stability and increased the PCE upto 21.5%.[166] Recently, treatment of the $MAPbBr_3$ PS films with $Cs_{0.05}(MA_{0.17}FA_{0.83})_{0.95}PbBr_3$ QDs greatly influences the effectiveness of ionic defect passivation with PCE exceeding 21% with more than 90% of its initial PCE retained on expo-sure to continuous illumination of more than 550 h.[167] Passivating the $CsPbI_3$ QDs over the triple-cation perovskite films greatly improved the morphology, surface electronic properties and the crystal structure of perovskite films to reach the PCE over 21%.[168] The use of the embedded or integrated QDs in perovskite matrix has been used as the efficient absorber layer in solar cells and the journey has been tabulated in **Table 2**.

4.1.3. Quantum Dot Electron Transport Layer for Electron Extraction in Perovskite Solar Cell

Oxygen, temperature, UV illumination, and biasing are detrimental to the long-term stability of PSCs. Although the coating of the PSCs is effective against moisture and oxygen, it is inadequate to protect the device from UV, heat, and biasing. The considerable increase in the cost of device making is another obstacle toward commercialization. Further, the interface configuration between the CTL and absorber layer is a deciding factor that affects the performance of PSCs. The fabrication of the HTL and ETL with suitable interfacial energy alignment plays a pivotal role in extracting charge carriers when constructing any solar cell modules. Both organic and inorganic materials have been used as HTLs. Thus far, the most common materials used are polymers such as PEDOT:PSS and PTAA and inorganic materials such as NiO_x and CuSCN. Recently, spiro-OMeTAD and bifluo-OMeTAD have emerged as the best in the business. TiO_2, ZnO, and SnO_2 are the commonly used ETL materials, along with some doped oxides. However, conventional HTL and ETL materials have different issues, which always lead to the poor stability of PSCs. The photocatalytic degradation of the PS layer by the TiO_2 ETL layer induces

pinholes by spiro-OMeTAD, which makes the PS layer severely hygroscopic, pulling back the extensive research on PSCs. However, the synergetic combination of semiconductor QDs and PSs offers a unique platform to enhance the PCE of PSCs.

In general, the ETL is sandwiched between a photoactive and transparent cathode or metal counter electrode to transport the generated electrons from the PS to the electrode.[169–172] The underlying effectiveness of the ETL in designing highly efficient PSC needs to be addressed. In PSCs, the ETL is indispensable for the following functions: i) Extraction and transportation of photogenerated electrons,[173] ii) efficient carrier recombination at the ETL/PS or electrode/ETL interface to facilitate interfacial charge dynamics,[174] iii) engineering the conduction band offset at the interface of ETL/PS,[175–177] and iv) regulation of UV light to eliminate light-induced degradation.[173] However, the main deciding factor is the electron transfer rate at the ETL/PS interface, because they are slower than the hole transfer at the PS/HTL interface.[173,174] This has a direct implication on the hysteresis behavior in efficiency measurement and ion migration.[174,178] Therefore, selecting and engineering the ETL in PSCs can be considered the most critical factor in designing highly efficient and stable PSCs. The choice of ETL for any PSC depends on two factors: i) the photons should pass through the ETL layer easily to be absorbed by the PS layer (for the same reason, the ETL with high transmittance in the UV–vis region is necessarily selected) and ii) the LUMO and HOMO of the ETL must be higher than that of the corresponding PS molecular orbitals. To date, fullerenes and their derivatives, along with conducting polymers and metal oxides,[179–181] have been found to show good performance, but as a tradeoff with stability because of the augmented nonradiative recombination. The quest to find a suitable ETL for PSCs has forced scientists to lean on QDs, which showed great potential as an ETL.

Cd Chalcogenides as Electron Transport Layer in Perovskite Solar Cell: Several QDs have been used as ETLs in PSCs so far because of their low cost and charge mobility. Among these, Cd- based chalcogenide QDs were found to be suitable to act as an ETL because of their incredible ability to generate multiple excitons. Cadmium selenide (CdSe) NCs were used for the first time as an ETL for PSCs because of their high electron mobility and solution-processability, which resulted in a PCE of 11.7%.[182] The possibility of employing a CdSe/PCBM composite as a promising ETL has been demonstrated to improve the structural and device stability and operating performance of PSCs.[183] An optimal PCE of 13.7% was obtained under ambient conditions. An all-inorganic ETL composed of CdSe QD/LiF double layers was developed for the inverted PSCs.[184] The CdS QDs were used as ETLs in several cases.[185–191] CdS nanorod (NR) arrays as an ETL via a physical-CVD process were used to upscale the PCE of PSCs. The CdS NRs not only provided a scaffold to the PS film but also increased the interfacial contact between the PS film and ETL to provide high mobility, thereby achieving a PCE of 12.46%.[189] Although the PCE achieved so far is quite impressive, further development is required to make the architecture more stable.

Green (Free from Pb and Cd) Quantum Dots as Electron Transport Layer in Perovskite Solar Cell: The use of SnS_2/SnS nanosheets as an ETL resulted in well-matched energy and

Table 2. Effect of different QDs (as absorber layer) on the PCE of PS-based solar cells of different architectures.

Type of QDs	QD	Effect of the QD	Device architecture	PCE [%]		Ref.
				W/O QD	With QD	
Pb-chalcogenide	PbS	Enhanced charge diffusion lengths due to improved electron transport and reduced electron recombination	TiO_2/PbS/MAPbI$_3$/P$_3$HT/Pt	1.91	4.92	[49]
	PbS	Prevented the degradation of MAPbI$_3$ by the ambient environment	ITO/ZnO/MAPbI$_3$-PbS/spiro-OMeTAD /Ag	6.30	6.99	[161]
	PbS	Enhancement of PL emission intensity and carrier life-time accompanying with improved surface morphology and homogenous composition distribution in QD-treated films	ITO/MZO/PbS-CsPbI$_3$-P/Au	8.80	10.50	[80]
	PbS	Reduced energy funneling, improved carrier transport, and efficient carrier injection into electrodes	ITO/ZnO/MAPbI$_3$-PbS/PbS-EDT/Au	8.80	11.28	[162]
	PbS	i) Elimination of the hysteresis-effect in metal-halide perovskites ii) Extension of the range of device photo response and simultaneously deliver excellent device performance as well as improved stability	ITO/ ZnO NPs/PbS QDs/n-PEDOT/SnO$_2$ NPs/MAPbI$_3$ perovskite/spiro-OMeTAD/ MoO$_3$/Ag	–	11.03	[163]
	PbS	Enhanced crystallization and more efficient carrier transport along the direction perpendicular to the substrate of the devices	FTO/compact TiO$_2$/CH$_3$NH$_3$PbI$_{3-x}$Cl$_x$/ spiro-OMeTAD/Au	–	17.40	[62]
	PbS	Larger crystal grain size, better morphology, higher crystallinity, and marginally broadened light absorption region	FTO/ETL/MAPI–PbS/HTL	14	18.6	[164]
	PbS	Stabilizes the black phase of FAPI in ambient conditions while preserving the narrow band gap of pure FAPI	FTO/SnO$_2$/FAPI-PbS/spiro-OMeTAD/Au	16.4	18.0	[53]
	PbS	Increased stability of the device Reduced defects, and increased moisture resistance ability	ITO/SnO$_2$/MAPbI$_{3\_}$ PbS /PCBM:C$_{60}$/ Zr(acac)$_4$/Ag		20.64	[165]
	PbS	Increases solar cell photoconversion efficiency and stability	ITO/SnO$_2$/FAPbI$_3$–PbS/spiro-OMeTAD/Au	15.53	17.08	[159]
			ITO/SnO$_2$/FAPbI$_3$ -MACl–PbS/ spiro-OMeTAD/Au	18.83	19.38	[159]
Cd-chalcogenide	CdSe/ZnS	Effectively passivate the surface charge traps and grain boundaries of perovskite materials	FTO/TiO$_2$/MAPbI$_3$-CdSe/ZnS QDs/C60/ BCP/Ag	14.67	19.89	[43]
Perovskite QDs	CsPbBr$_3$	Accelerate the crystallization of perovskite precursor solution reduced defect density	ITO/SnO$_2$/CsPbIBr$_2$-CsPbBr$_3$/ Spiro-OMeTAD/MoO$_3$/Au	8.70	11.10	[83]
	CsPbBrCl$_2$	Increased stability by filling the defect sites and rendering moisture stability	PTAA/MAPbI$_3$-CsPbBrCl$_2$/C60/BCP/Cu.		21.5	[166]
	Cs$_{0.05}$(MA$_{0.17}$FA$_{0.83}$)$_{0.95}$PbBr$_3$	i) Reduced non-radiative recombination and extended charge carrier lifetimes ii) Enhanced moisture and photostability due to the formation of low dimensional perovskite which increases surface hydrophobicity and device stability	FTO/SnO$_2$/(FAPbI$_3$)-(MAPbBr$_3$)$_{1-x}$/QDs/ Spiro-OMeTAD/Au.	19.45	21.1	[167]
	CsPbI$_3$	Improvement of the morphology, surface electronic properties and the crystal structure of perovskite films	ITO/PTAA/FAMACs perovskite:CsPbI$_3$ QDs/ PC$_{61}$BM/C$_{60}$/BCP/Cu		21.03	[168]

a higher V_{oc} promotion (from 0.94 to 1.08 V); it was found to increase the PCE by 27.95% (from 14.13% to 18.08%), compared with pristine SnS$_2$ ETL.[175] Zn$_2$SnO$_4$ nanoparticles have been successfully used as efficient ETL materials for both

conventional n-i-p and inverted p-i-n PSCs, which results in an exceptional PCE of 17.7% along with enhanced ambient stability (over 90% of the initial PCE was retained after 14-day storage under ambient conditions at 30 ± 5% relative humidity).[192] The use of solution-processed ZnSe NCs has been found to increase electron mobility and reduce charge accumulation to produce a high PCE.[193–195] The potential of solution-processed ZnSe NC-based ETL has been demonstrated (**Figure 10**A) to achieve a high PCE of 17.78% with negligible hysteresis, compared with a TiO₂-based cell (13.76%). The use of In₂S₃ as an ETL for MAPbI₃ PSs resulted in considerably encouraging PCE values of 18.22% and 18.83%, respectively.[196,197] However, the use of In₂S₃ also increased the PCE to 5.59% for an all-inorganic CsPbIBr₂ PSC (Figure 10B and **Table 3**).[198]

4.1.4. Quantum Dot Hole Transport Layer for Hole Extraction in Perovskite Solar Cell

For any PSC, the steps for PVs include: i) Absorption of light, ii) electron–hole separation, and iii) efficient carrier collection. As discussed previously, engineering different interfaces is of the utmost importance for successfully fabricating a stable and efficient PSC. The interface between the HTL and PS with perfect energy-level alignment favors efficient charge collection. Although the HTL in PSCs has several important functions, the main method is to extract holes from the perovskite sensitizer layer and improve hole transport efficiency.[199–202] The HTL acts as an energy barrier between the PS layer and the back contact to prevent carrier recombination.[203,204]
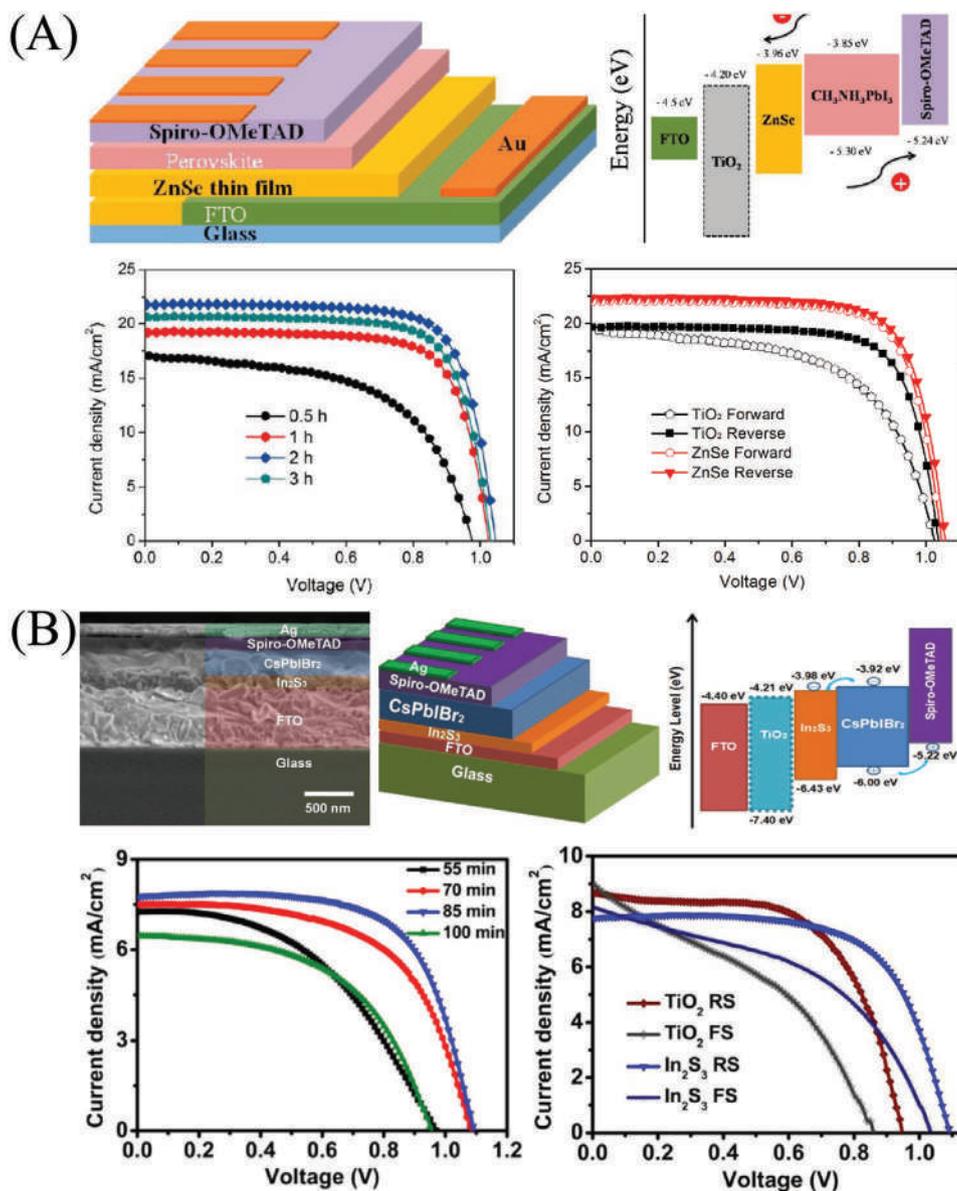
Figure 10. A) Cell architecture, energy band diagram, J–V curves of the perovskite solar cells based on various ZnSe ETLs and J–V curves of the best performing PKSCs using ZnSe and TiO₂ ETLs. Reproduced with permission.[195] Copyright 2018, American Chemical Society. B) Cross-sectional SEM image of the device and its architecture, energy band diagram, J–V curves and best performance of the devices with In₂S₃ nanostructures as ETL. Reproduced with permission.[198] Copyright 2019, Elsevier.

Table 3. Effect of different QDs (as electron transport layer) on the photobehaviors and PCE of PS-based solar cells of different architectures.

Type of QDs	QD	Effect of the QD	Device architecture	PCE [%] W/O QD	With QD	Ref.
Cd-chalcogenide	CdSe	Efficient electron transport ability	ITO/CdSe/CH$_3$NH$_3$PbI$_3$/spiro-OMeTAD/Ag	9.00	11.70	[182]
		Introduced structural stability and exhibit enhanced photocurrent and fill factor	ITO/PEDOT:PSS/CH$_3$NH$_3$PbI$_{3-x}$Cl$_x$/CdSe-PCBM/Rhodamine101/LiF/Ag	11.22	13.70	[183]
		Enhanced electrons transfer and extraction efficiency along with performance stability	ITO/PEDOT:PSS/CH$_3$NH$_3$PbI$_3$/CdSe-LiF/Ag	4.80	15.10	[184]
	CdS	Ensuring larger interfacial areas and higher electron mobility	ITO/CdS NRs/CH$_3$NH$_3$PbI$_3$/spiro-MeOTAD/MoO$_3$/Ag	–	2.27	[185]
		Larger grain PS layer with less surface roughness, Facilitating the charge transport, reducing the charge recombination by decreasing the surface traps	FTO/CdS/CH$_3$NH$_3$PbI$_3$/spiro-MeOTAD/Ag	–	8.36	[186]
		Reducing charge-trapping effect	FTO/CdS/CH$_3$NH$_3$PbI$_3$/spiro-MeOTAD/Au	–	12.20	[187]
		Higher electron mobility and charge transport	ITO/CdS/CH$_3$NH$_3$PbI$_3$/spiro-MeOTAD/Au	–	10.80	[188]
		Perovskite deposition, light transmission, provided high mobility.	FTO/CdSNRs/CH$_3$NH$_3$PbI$_{3-x}$Cl$_x$/spiro-MeOTAD/Ag	–	12.46	[189]
		Higher recombination resistance and efficient charge extraction in the interfaces	ITO/CdS/CH$_3$NH$_3$PbI$_3$/Spiro-OMeTAD/Ag	–	16.10	[190]
		Enhanced electron extraction and transfer properties	FTO/CdS/Cs$_{0.05}$(MA$_{0.17}$FA$_{0.83}$)$_{0.95}$Pb(I$_{0.83}$Br$_{0.17}$)$_3$/spiro-MeOTAD/Au	–	16.50	[191]
Green QDs	Zn$_2$SnO$_4$	Facilitates efficient electron transfer and extraction in the derived devices along with introduction of extraordinary stability	ITO/Zn$_2$SnO$_4$-PCBM/Perovskite/NiO$_x$/Ag	–	17.70	[192]
	SnS$_2$/SnS	Caused better energy level alignment (ELA) between electron transport layers (ETLs) and perovskite layers	FTO/SnS$_2$/SnS/Cs$_{0.05}$(FA$_{0.83}$MA$_{0.17}$)$_{0.95}$Pb(I$_{0.83}$Br$_{0.17}$)$_3$/Sprio-OMeTAD/Au	14.13	18.08	[175]
	ZnSe	Better separation of the carriers and increases carrier transfer efficiency to reduce the interface charge recombination	FTO/ZnO/ZnO@ZnSe/CH$_3$NH$_3$PbI$_3$/Spiro-OMeTAD/Au	6.65	8.44	[193]
		Enhanced electron transport ability and device stability	ITO/PTAA/FA$_{0.9}$MA$_{0.1}$PbI$_{2.7}$Br$_{0.3}$/C60/ZnSe/Ag	–	18.38	[194]
		High electron mobility, and reduced charge accumulation at the interface of ETL/perovskite	FTO/TiO$_2$/ZnSe/CH$_3$NH$_3$PbI$_3$/Spiro-OMeTAD/Au	13.76	18.57	[195]
	In$_2$S$_3$	Optimized band structure, enhanced light tapping, high charge carrier injection and separation	FTO/TiO$_2$/In$_2$S$_3$/CH$_3$NH$_3$PbI$_3$/Spiro-OMeTAD/Au	15.70	18.22	[196]
		Lower potential barrier for electron injection from the perovskite layer, higher electron mobility and electron extraction ratio at the In$_2$S$_3$/ CH$_3$NH$_3$PbI$_3$ interface, smaller contact resistance, and charge recombination.	FTO/TiO$_2$/In$_2$S$_3$/CH$_3$NH$_3$PbI$_3$/Spiro-OMeTAD/Au	15.88	18.83	[197]
		Suitable band alignment, low resistance, and low recombination of photo-generated carriers at the interface of In$_2$S$_3$/CsPbIBr$_2$	FTO/In$_2$S$_3$/CsPbIBr$_2$/Spiro-OMeTAD/Ag	5.02	5.59	[198]

The speed of extracting the photogenerated holes from the absorber is the determining step for modulating the device efficiency and stability, and it is governed by the HTL. Thus, engineering the HTL/PS interface is very important for suppressing carrier recombination, blocking electron transport, and improving the corresponding interface selectivity.[204] Sometimes HTL plays a crucial role in preventing the degradation of the PS layer by acting as a moisture-resistant or metal ion diffusion barrier.[199,200,205,206] Stability issues give the HTL an upper hand, and numerous studies have been performed for developing unique and effective HTL. Diverse HTLs has been employed to improve the efficiency and stability of PSCs. Small molecules,[207–209] organic polymers,[210,211] and metal-phthalocyanines,[212–215] have been used as efficient hole transfer materials, although their hygroscopic nature and questionable stability issue restricted their use in PSCs. To this end, a special mention of spiro-OMeTAD is necessary.[216] However, the use of spiro-OMeTAD as an HTL has been debated for many years in terms of its cost-effectiveness, long-term stability, temperature, and environment-dependent

**ADVANCED
SCIENCE NEWS**

www.advancedsciencenews.com

**ADVANCED
OPTICAL
MATERIALS**

www.advopticalmat.de

degradation issues. These organic materials suffer from low hole conductivity because of their amorphous nature. Therefore, different additives such as bis(trifluoromethane)sulfonimide lithium salt (LiTFSI),[217–219] 4-tert-butylpyridine (TBP),[220,221] and tris(2-(1H-pyrazol-1-yl)-4-tert-butylpyridine) cobalt(III) bis(trifluoromethylsulfonyl)imide (FK209),[222–225] have been introduced by many scientists to enhance the electrical properties of the hole transport material (HTM). The hygroscopic nature of these dopants, along with their ability to diffuse ions, not only deteriorates the long-term stability of PSCs but also increase the cost so much that the commercialization of these PSCs seems impossible. Therefore, the development of dopant-free HTL has gained interest very recently.[206] In this regard, inorganic hole-transporting materials can act as an escape route in terms of stability and high cost. Inorganic HTMs have advantages of high intrinsic hole mobilities, low cost, and good stability. Inorganic HTMs have been less investigated due to the difficulty in the preparation of high-quality films via a simple and inexpensive method, and the PCE lags that of organic HTMs. An empirical four-element golden law was formulated after a comprehensive summary and analysis of the reported results to guide the further design of dopant-free HTMs: 1) An ideal HTM should have a high hole mobility to avoid the use of dopants; 2) it should effectively extract and transport holes, which require a suitable energy level, high film quality, and optimized interfacial contact; 3) it needs to be stable under thermal, optical, chemical, and environmental stresses; and 4) it should be cost-effective in terms of both the material price and production cost.[206]

Chalcogenides as Hole Transport Layer in Perovskite Solar Cell: The use of PbS as a hole transporting layer in PSCs has gained attention due to their superior hole extraction efficiency which can balance the important charge transfer process. The hole injection from $CH_3NH_3PbI_3$ into PbS CQDs is favored by the shallow valence band edge of PbS CQDs compared to $CH_3NH_3PbI_3$; and the device based on PbS hole transporting material showed an optimized PCE of 7.5% with its absorption extended to 1000 nm.[226] In another report, PbS was employed to construct a spiro-OMeTAD/PbS bilayer which exhibited a higher hole extraction efficiency than bare spiro-OMeTAD.[227] Employing the buffer bilayer resulted in an enhanced charge extraction process between perovskite and HTL, and a more balanced electron and hole transfer event to give an improved PCE from 17.4% to 18.0%. However, in a very recent report, the same approach has been able to increase the PCE upto 20.11%.[228]

Cd Chalcogenides as Hole Transport Layer in Perovskite Solar Cell: The contact between PSs and HTL has been improved by using CdTe QDs,[229] CdSe/CdS QDs,[230] and hybrid CdSe/CsPbI₃.[82] The CdSe/CdS layer as the HTL proved to be quite effective for converting high-energy UV light into lower-energy visible wavelengths, which improved the UV stability and device performance (higher J_{sc} and PCE, with a maximum efficiency of 20.7%) of the PSCs. Improved contact between the PS and HTL was demonstrated using CdTe QDs. Devices with CdTe QD-in-PS solid interlayer achieved a high efficiency (≈19.3%, averaged), which was attributed to the congeneric junction contact between the PSs and CdTe QD-in-PS layer. A PCE of 21% was achieved by employing hybrid CdSe/CsPbI₃ QDs as the HTL.

Green Quantum Dots (Free from Pb and Cd) as Hole Transport Layer in Perovskite Solar Cell: Although p-type semiconductors have been used in different solar cells for many years, their use in PSCs has not been properly explored. Cu-and Ni-based oxides have mostly been used in DSSCs and QDSCs to induce stability and reduce the commercialization cost. CuO, MoO_3, and NiO_x are inorganic HTLs that have shown excellent performance in fabricating stable and efficient PSCs.[231–235] Several QDs were found to be very effective in enhancing the PCE stability. The $Cu_{1.8}S$ modified HTL could enhance hole extraction at the PS/HTL interface and suppress carrier recombination.[236] Other Cu-based QDs such as $CuInSe_2$,[237,238] $CuGaS_2$,[239] Cu_2ZnSnS_4,[240] $Cu_{12}Sb_4S_{13}$,[241] and $CsCu_5S_3$ (**Figure 11A**)[242] have been implicated in enhancing the hole transfer (**Table 4**). Recently, molybdenum disulfide (MoS_2) and reduced graphene oxide (RGO) hybrids were used as the HTL and active buffer layer in mesoscopic methylammonium lead iodide PS ($MAPbI_3$)-based PSCs. The MoS_2 QDs anchored to the functional sites of RGO flakes effectively and collected the photogenerated holes (as well as block electrons) from $MAPbI_3$ toward the anode contact in the mesoscopic architecture, which resulted in better regulation of charge transfer and energy transfer processes for reaching the maximum PCE value of 20.12% (average PCE of 18.8%) (Figure 11B).[243] BPQDs were employed to increase the hole extraction rate with more efficient hole transfer and suppression of energy-loss recombination.[244–246] Carbon and GQDs were used as the HTL in different PSCs.[247–249]

Perovskite Quantum Dots as Hole Transport Layer in Perovskite Solar Cell: The PSQD rich HTL over the PSs absorber layer was proven to be considerably efficient for extracting holes at the interface, which led to highly efficient PSCs with enhanced stability (Figure 11C).[166,250,251] Fabrication of $FAPbI_3$-based bulk perovskite thin films with a Cs-rich surface using solution-deposition of $Cs_{1-x}FA_xPbI_3$ alloy perovskite QDs not only improved the charge dynamics in the devices but also significantly enhanced the ambient stability of the $FAPbI_3$-based thin films and the associated PSCs to reach the PCE up to 20.82%.[250] Incorporation of an ultra-thin interfacial layer of inorganic $CsPbBr_{1.85}I_{1.15}$ perovskite quantum-dots showed potential regarding defect passivation at or near to the perovskite/HTM interface, which significantly suppressed interfacial recombination to produce hysteresis-free cells with the efficiency beyond 21%.[251]

4.2. Quantum Dot/Perovskite Systems as LEDs

Organic semiconductors, metal chalcogenides, and colloidal semiconductor NCs have been considered next-generation materials; however, the introduction of highly luminescent PS nano/microcrystals with controllable dimensionalities and very narrow emission (full width at half maximum, FWHM ~ 20 nm) and high mobility completely changed the scenario.[252,253] LEDs based on solution-processable PSs have been applied in flat panel displays and solid-state lighting, and the past 5 years have witnessed unprecedented advancements in the field of PS-based LEDs.[254–256] Here, the interaction between halide PSs and semiconductor QDs has reported interesting outcomes.

**ADVANCED
SCIENCE NEWS**

www.advancedsciencenews.com

**ADVANCED
OPTICAL
MATERIALS**

www.advopticalmat.de
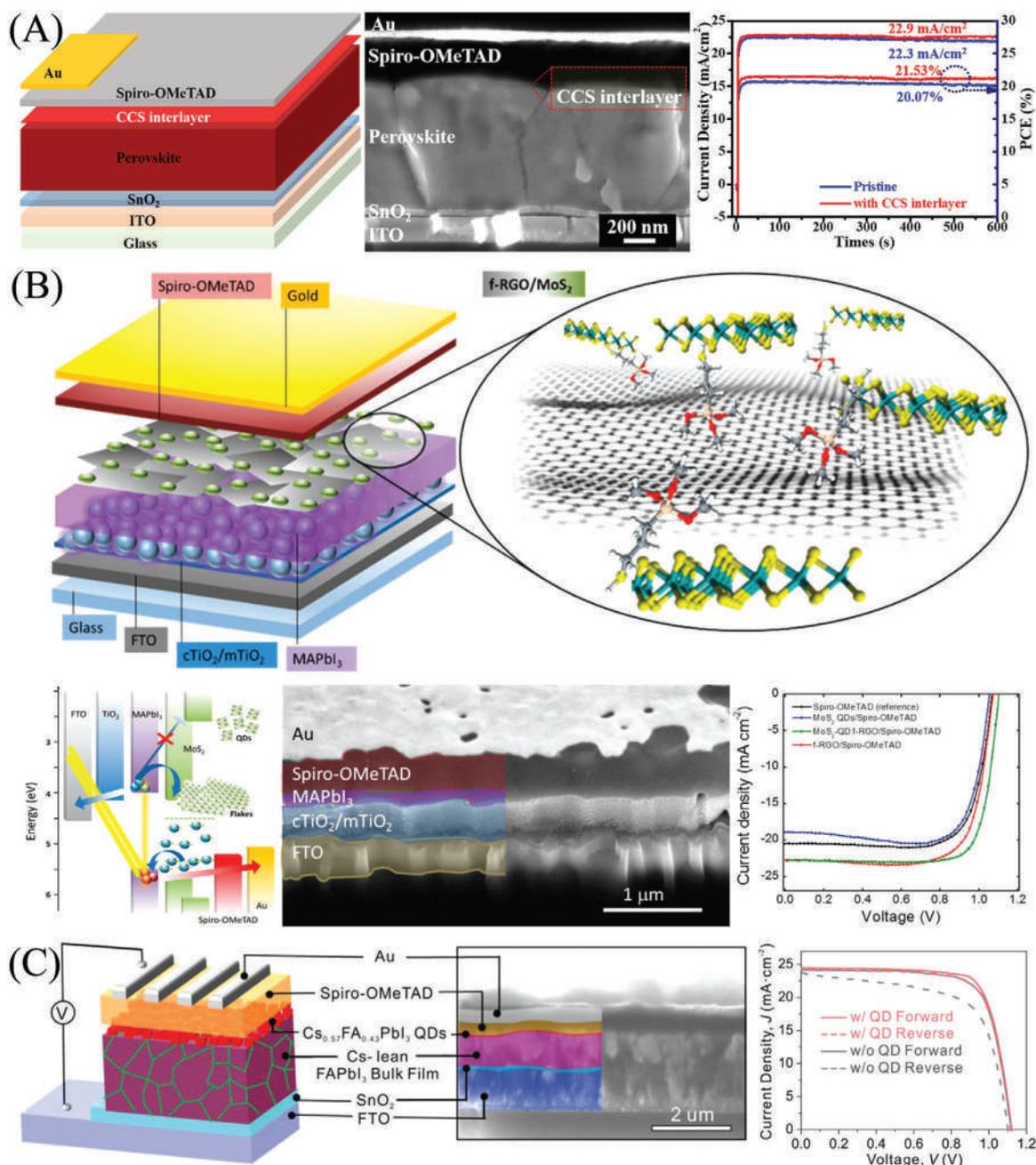
Figure 11. A) Device architecture and cross-sectional view of SEM images of PSC with a $CsCu_5S_3$ interlayer, and devices current density and PCE behaviors of pristine and of PSC with $CsCu_5S_3$ interlayer. Reproduced with permission.[237] Copyright 2021, Elsevier. B) Upper panel: Schematic of mesoscopic $MAPbI_3$-based PSC exploiting MoS_2 QDs:f-RGO hybrids as both HTL and ABL. Lower panel: Diagram of the energy band edge positions of the materials used in the different components of the assembled mesoscopic $MAPbI_3$-based PSC, cross-sectional SEM image of a representative PSC device, I–V characteristics of tested PSCs using MoS_2 QDs, f-RGO, and MoS_2 QDs:f-RGO as HTL. Reproduced with permission.[238] Copyright 2019, American Chemical Society. C) Illustration of the PSC device structure, cross-sectional SEM image of the fabricated device and J–V curves of the PSCs with and without $Cs_{0.57}FA_{0.43}PbI_3$ QD modification (both reverse and forward scans). Reproduced with permission.[245] Copyright 2019, American Chemical Society.

A hybrid LED system can benefit from the good transport properties of halide PSs to increase the performance of NIR LEDs using PbS QDs as active emitters. The first report on an NIR LED based on PbS QDs embedded in a mixed halide $MAPbI_xBr_{3-x}$ matrix gave an EQE of 4.9%.[257] The same group beat these results by reporting an EQE to 8.1% at 980 nm at a radiance of up to 7.4 W Sr^{-1} m^{-2} using a layered PS matrix.[124]

The issues of luminescence efficiency, charge transport, and high power consumption have been overcome by embedding QDs in a high-mobility hybrid PS matrix, and this provides a long diffusion length to enhance the number of injected carriers that successfully diffuse to a QD with excellent passivation, which improves both fractions of these carriers that transfer into a QD and form QD-localized excitons that recombine

Table 4. Effect of different QDs (as hole transport layer) on the photobehaviors and PCE of PS-based solar cells of different architectures.

Type of QDs	QD	Effect of the QD	Device architecture	PCE [%]		Ref.
				W/O QD	With QD	
Pb chalcogenides	PbS	Superior hole extraction and injection	$ITO/PbS/CH_3NH_3PbI_3/PCBM/Al$	–	7.5	[226]
		Increased charge transfer, improved device stability and photovoltaic performance	$FTO/SnO_2/PCBM/perovskite/spiro-OMeTAD/PbS/Au$	17.4	18.0	[227]
		Reduced carrier loss and improved carrier transmission performance	FTO/PCBM/perovskite/spiro-OMeTAD/PbS/Au	13.17	20.11	[228]
Cd chalcogenides	CdTe	Faster hole extraction at the interface due to the high hole mobility in CdTe	$ITO/SnO_2/MAPbI_3/CdTe-QD/Spiro-OMeTAD/Ag$	17.40	18.40	[229]
	CdSe/CdS	Improves the grain size and crystallinity leading to a longer carrier lifetime as compared to perovskite films	$ITO/NiO/MAPbI_3/CdSe-CdS/C-60/BCP/Ag$	18.80	20.70	[230]
	$CdSe/CsPbI_3$	Serves as charge transport bridges and also as passivation materials	$ITO/TiO_2/MAPbI_3/CdSe-CsPbI_3/Spiro-OMeTAD/Au$	14.0	17.10	[82]
Green QDs	$Cu_{1.8}S$	Improve the hole mobility, conductivity, and stability of Spiro-OMeTAD hole transport layer	$FTO/c-TiO_2/m-TiO_2/Ti_3C_2T_x$ QDs-Perovskite/$Cu_{1.8}S$-Spiro-OMeTAD/Au	18.31	21.64	[236]
	CuInSe	Facilitated the hole transport and protected the perovskite from moisture.	$ITO/SnO_2/Perovskite/CuInSe/Au$	–	13.72	[237]
		Higher light transmission rate and conductivity of CISe film	ITO/CuInSe/Perovskite/PCBM/BCP/Au	7.18	8.59	[238]
	$CuGaS_2$	$CuGaS_2$ QDs with lower surface defects, suppressed the carrier recombination process.	$ITO/SnO_2/Perovskite/CuGaS_2/Au$	–	17.56	[239]
	Cu_2ZnSnS_4	Effective hole extraction and transfer properties of the CZTS QDs interface layer.	$FTO/c-TiO_2/m-TiO_2/CsPbBr_3/Cu_2ZnSnS_4/Ag$	–	4.84	[240]
	$Cu_{12}Sb_4S_{13}$	Enhanced light harvesting and outstanding hole extraction ability of the QDs	$FTO/c-TiO_2/m-TiO_2/CsPbI_3/Cu_{12}Sb_4S_{13}/Au$	–	12.14	[241]
	$CsCu_5S_3$	The QD interlayer is favorable for energy levels between the perovskite and HTM to reduce carrier recombination	$ITO/SnO_2/perovskite/CsCu_5S_3$ interlayer/ Spiro-OMeTAD/Au	–	22.29	[242]
	MoS_2	Effectively collect the photogenerated holes (as well as to block electrons) from $MAPbI_3$ toward the anode contact in mesoscopic architecture	$ITO/c-TiO_2/m-TiO_2/MAPbI_3/RGO-MOS_2$ interlayer/ Spiro-OMeTAD/Au	17.08	20.12	[243]
	Black P QDs	Nucleation assistance for the growth of large grain size perovskite crystals, fast hole extraction, more efficient hole transfer, and suppression of energy-loss recombination at the anode interface	$ITO/PEDOT/BPQD/MAPbI_3/PCBM/Au$	14.10	16.69	[245]
		The lone-pair electrons of BPQDs can induce strong binding between molecules of the $CsPbI_2Br$ precursor solution and P atoms stemming from the concomitant reduction in coulombic repulsion	$ITO/SnO_2/BPQD@CsPbI_2Br/Spiro-OMeTAD/Au$	–	15.47	[246]
	Carbon QD	Accelerated carrier transport and suppressed carrier recombination due to the ameliorated band alignment, passivated defect states, improved hole mobility, and crystalline properties	$FTO/cp-TiO_2/mp-TiO_2/MAPbI_3-CQD/Spiro-OMeTAD/Au$	–	13.30	[247]
	Graphene QD	Improved grain size, stability and optimized band alignment	$FTO/\alpha-Fe_2O_3/MAPbI_3-NSGQD/Spiro-OMeTAD/Au$	14.0	19.20	[248]
Perovskite QDs	$Cs_{1-x}FA_xPbI_3$	Reduces the film hygroscopicity, thereby imparting ambient stability. Also favors more efficient hole extraction at that interface	$FTO/SnO_2/FAPbI_3/Cs_{0.57}FA_{0.43}PbI_3/Spiro-OMeTAD/Au$	–	20.82	[250]
	$CsPbBr_{1.85}I_{1.15}$	Suppressed charge recombination, increased moisture stability	FTO/c-TiO2/ $m-TiO_2/Cs_{0.05}(FA_{0.85}MA_{0.15})_{0.95}Pb(I_{0.85}Br_{0.15})_3/$ $CsPbBr_{1.85}I_{1.15}/spiro-OMeTAD/Au$	19.51	21.14	[251]

**ADVANCED
SCIENCE NEWS**

www.advancedsciencenews.com

**ADVANCED
OPTICAL
MATERIALS**

www.advopticalmat.de

radiatively. A type-I band alignment enables electrons and holes to be funneled efficiently from the matrix and confined in the QDs, which prevents exciton dissociation losses. Very recently, a report showed that $CsPbI_3$ perovskite QD-in-matrix heteroepitaxial structures gave 12 times higher maximum luminescence (≈ 4700 cd m^{-2}) and higher efficiency ($\approx 18\%$) in QD-in-matrix LEDs compared to the QD-only control (**Figure 12**A).[258] No electroluminescence shift was observed in QD-in-matrix LEDs along with a stupendous rise in the lifetime (The T_{50} at 100 cd m^{-2} is estimated to be 2100 h for QD-in-matrix LEDs, whereas, the T_{50} of the QD-only device at ≈ 184 cd m^{-2} is merely 25 min). Reduced gradient crystallization and suppressed halide segregation, enabled charge carrier transport to the dots,

which lead to high performance QD LEDs that unite high efficiency and high brightness with improved stability compared to prior perovskite reports. Mora-Seró developed pinhole-free $CH_3NH_3PbI_3$ films embedded with PbS and PbS/CdS core/shell QDs for fabricating NIR LEDs with low turn-on potentials.[259] The strong interaction between the PSs and QDs generated the emission from the exciplex. This was indeed a valuable proof of concept for the coupling of these two important families of materials. Very recently, the same group demonstrated a simple method for preparing white-light-emitting diodes with tunable warm-cold emission (Figure 12B) based on QD colloidal solutions using mixed CQDs and $CsPbI_3$ PSQDs.[260] The combination of halide PSs and PbS QDs allows tuning emission
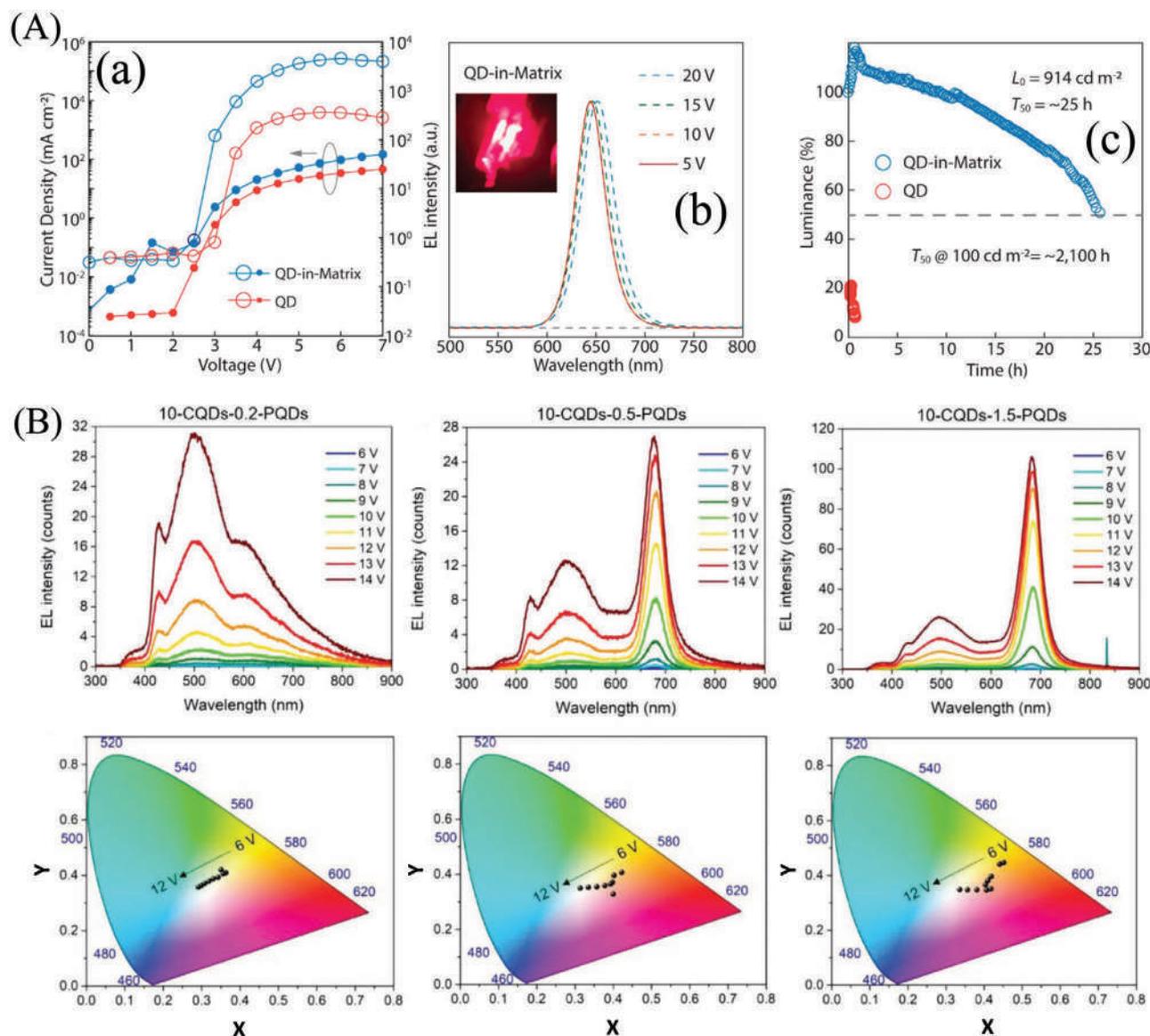
Figure 12. A) Electroluminescence and operating stability of QD and QD-in-matrix LEDs. a) Luminance and current density, as a function of applied bias. b) Electroluminescence spectrum of a representative QD-in-matrix LED at different driving voltages. c) Relative luminance versus operation time at ambient condition (23–25 °C; relative humidity ≈ 30%), measured with a constant drive current and an initial luminance of 914 cd m^{-2} (QD-in-matrix LED) and 184 cd m^{-2} (QD-only LED). Reproduced with permission.[258] Copyright 2021, American Chemical Society. B) Electroluminescence spectra and their corresponding chromaticity diagram generated by the WLEDs based on 10-CQDs–X-PQDs colloidal solutions, X = 0.2, 0.5, and 1.5 at different operation voltages. Reproduced with permission.[260] Copyright 2018, Wiley-VCH.

between the visible and NIR spectral regions via the applied voltage.[58]

Accessibility in the NIR region apart from the visible region attributed to the incorporation of QDs is a winning moment for PS-based LED devices. The careful choice of QDs passivates the surface defects (generally deep traps), impedes ion migration, and localizes the exciton migration to induce higher EQE.

4.3. Quantum Dot/Perovskite Systems as Photodetectors

Recently, photodetectors have received extensive attention because of their rapidly increasing use in biochemical detection, environmental monitoring, and optical communications.[261,262] PSNCs with outstanding optical and electrical properties show exceptional sensitivity to lower brightness and have a detection band in which photodetectors can efficiently detect light and dynamic range responses.[263,264] However, the development of PS-based broadband photodetectors is severely restricted because of their limited wavelength region up to 820 nm.[261,262] Incorporating NIR-absorbing QDs within PS films can successfully increase the detection limit. The Sargent group reported that field-emission QD (PbS)-in-PS ($CH_3NH_3PbI_{2.5}Br_{0.5}$) photodiodes extended the PS response into the short-wavelength infrared and achieved measured specific detectivities exceeding 10^{12} Jones.[265] The mechanism of photocurrent generation in these systems is fascinating because of the presence of QDs.[265] Photogenerated excitons confined within the QDs in the presence of an external large electric field separate themselves and release the charge into the host PS matrix. The emitted electrons and holes are then extracted and reinjected at the electrodes, which results in a multiplicative (i.e., one exhibiting gain) photocurrent (**Figure 13**A). A 45-fold increase in photoresponsivity was observed at a 0.5 V reverse bias as photogenerated charges in the QDs started to be emitted into the PS matrix.[265] Their field-emission solution-processed optoelectronic architecture exploits a set of physical effects previously attained only through costly heteroepitaxy.[265] $CH_3NH_3PbI_3$ PS-PbSe QD hybrid phototransistors with a wide photodetection region ranging from 300 to 1500 nm have been developed with high sensitivity (R = 1.2 A W^{-1}), high carrier mobility (μ_n = 0.147 cm^2 V^{-1} s^{-1} and μ_p = 0.16 cm^2 V^{-1} s^{-1}), fast response times (rise time: 2.5 ms and fall time: 3 ms), and excellent stability and reproducibility.[266] The ultra-broadband photodetection, especially in the IR region with the help of $CH_3NH_3PbI_3$ PS–PbSe QD heterostructures, has demonstrated great potential in designing cost-effective, solution-processed NIR photodetectors.[266] A tandem photodiode based on a bilayer of PbS QDs and $CsPbBr_3$ PSNCs has been reported with detectivities as high as 8×10^{10} Jones.[50] Phototransistors composed of a vertically stacked $Au/PbS/CsPbCl_3$ architecture demonstrated excellent broadband photodetection of UV–vis–NIR.[267] The photodiode showed a remarkable responsivity of 3892 A W^{-1}, a high detectivity of 3.29×10^{13} Jones, with a wide spectral photodetection range of 300–1100 nm.[267] Solution-processed, high-performance broadband (300–1100 nm) photodetectors based on double active layers incorporating narrow-bandgap $CuInSe_2$ QDs and halide PSs have been developed very recently.[67] The photoelectric conversion capacity was improved because of the

joint light absorption effect of $CuInSe_2$ QDs and the halide PS. The optimized photodetector exhibited responsivity over 150 mA W^{-1} in the visible range and by more than 20 mA W^{-1} in the near-infrared (800–1000 nm) range; specific detectivity of more than 7.0×10^{12} Jones in the visible region and 7.7×10^{11} Jones in the near-infrared region; a transient response time of 277 ns with the active area of 0.013 cm^2; and a linear dynamic range of ≈75 dB (Figure 13B). Furthermore, the introduction of CISe QDs not only facilitated the correct separation of carriers, but also improved the air and thermal stabilities of the photodetector.[67] A hybrid HTM composed of $CuInSe_2$ QDs and PEDOT:PSS was employed to enhance the performance of $MAPbI_3$ PS-based photodetectors.[268] The resulting hybrid HTL-based device was superior to the control device in the field of a larger ratio of photocurrent density to dark current density (4.1×10^6), broader LDR (132 dB), faster on-off switching properties (<0.02 s), higher photoresponsivity (240 mA W^{-1}), and larger detectivity (≈1.02×10^{13} Jones). The extraordinary performance of the device can be ascribed to three reasons: I) Easy extraction of holes from the PS layer because of the complementary energy band structure of $CuInSe_2$ QDs and PEDOT:PSS; II) $CuInSe_2$ QDs increases the surface roughness of PEDOT:PSS, which serve as nucleation centers for the growth of PS crystals; and III) increase in charge collection at the active layer because of the excellent light-harvesting ability of $CuInSe_2$ QDs. High specific detectivity (2.2×10^{12} Jones), a fast fall time of 236 µs, and an extremely low NEP (45 fW $Hz^{-1/2}$) have been reported in another $CuInSe_2$ QD-based hybrid PS photodetector.[68] The interfacial band offset between the $MAPbI_3$ film and $CuInSe_2$ QDs extends the detection range of the photodetector in the NIR region.[68] Thus far, $CuInSe_2$ QDs have been proved to be considerably useful not only to broaden the spectral detection range of PS-based hybrid photodetectors but also to enhance their performance and improve stability.[68] High-performance photodetectors based on $CH_3NH_3PbI_3$ ($MAPbI_3$)/CdS heterostructures demonstrated a maximum detectivity of 2.3×10^{11} Jones, along with a responsivity of 0.43 A W^{-1} measured at 730 nm.[269] A detectivity over 6×10^{13} Jones at a 2 V bias with a response time of 11.5 µs, an EQE of 4500%, and photoresponsivity of 15 000 mA W^{-1} has been reported for $MAPbI_3$/PbS QD photodetectors, which exploits the trap-assisted charge injection process.[270]

The strategy of incorporating QDs in PSs has been found to be considerably useful for fabricating vis–NIR PS photodetectors. The incorporated QDs sufficiently increased the rate of transport of the photogenerated carriers along with gate tuning. The underlying plan is to manipulate the conduction and valence bands of the PSs and QDs such that the photogenerated carriers can be successfully transferred to the conduction band of the QD with lower energy; the holes generated at the QD can easily be transported to the valance band of the PS. More efficient hole mobility, hole transfer, and hole collection at the electrode is key to the success of photodetectors comprising QD/PS systems.

5. Conclusion and Future Perspectives

This review highlighted a very new strategy for QD incorporation to increase the stability and efficiency of PS-based PVs and
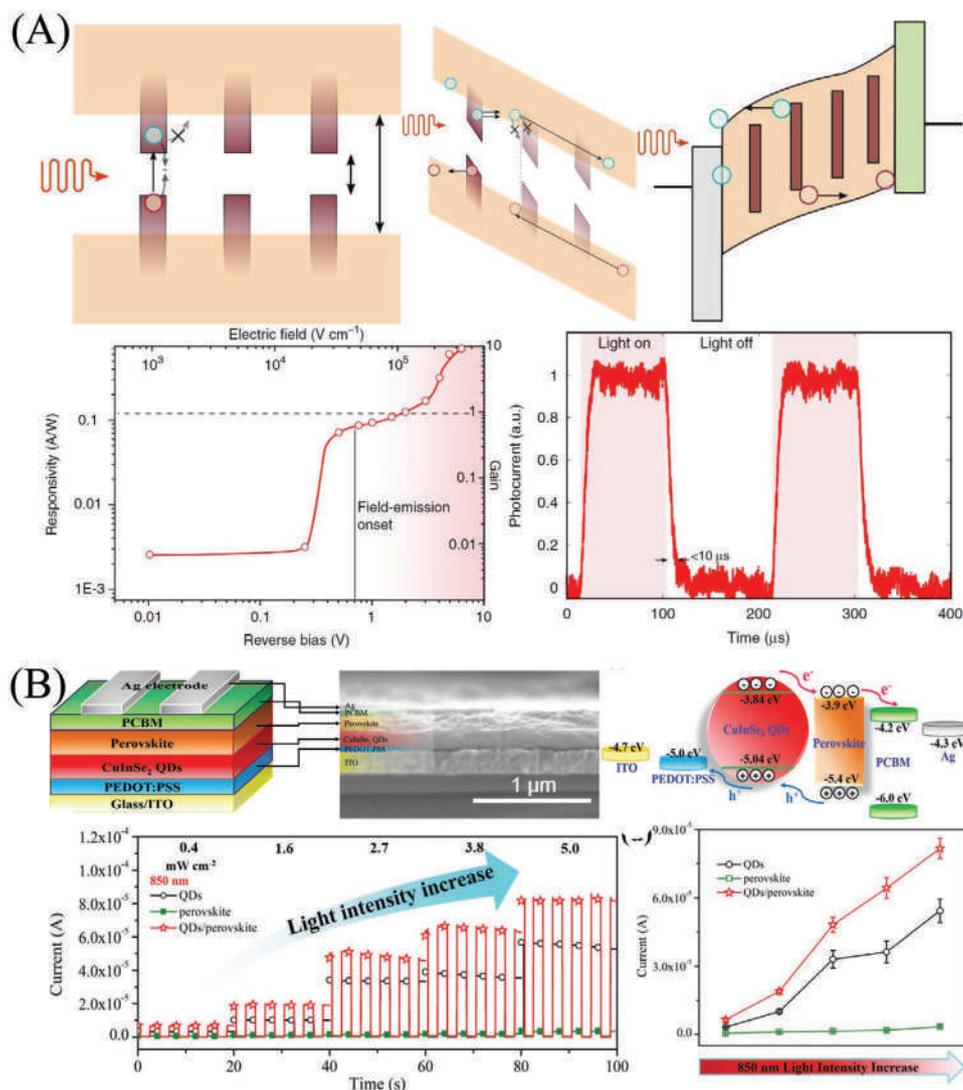
Figure 13. A) Schematic of trapping and eventual recombination of photogenerated excitons in perovskite layer through QDs, tunneling of carriers and operation of the field-emission QD/PS photodiode (upper panel). Lower panel elaborates the responsivity of the photodetector as a function of reverse bias and the photo response dynamics at 1 V reverse bias. Reproduced with permission.[265] Copyright 2017, Springer Nature. B) The architecture structure, the cross-sectional SEM image and the energy band diagram of the double-active layer photodetector based on lead halide perovskite and CuInSe$_2$ QDs. Lower panel shows the time-dependent response of fresh photodetectors based on CuInSe$_2$ QDs, perovskite, and double-active layer photodetector (at 0 bias voltage) to 850 nm on/off modulated light. The relationship between the current and the 850 nm modulated light intensity of devices based on CISe QDs, perovskite, and double-active layer photodetector in the air without encapsulation. Reproduced with permission.[67] Copyright 2020, Wiley-VCH.

optoelectronic devices. An exhaustive essay has been conducted on the progress made to date in this field. We elaborately discussed state-of-the-art solution-based synthetic strategies to shed light on the heteroepitaxy of defect-free interfaces between QDs and PSs. Then, we focused on deciphering the underlying electron and hole dynamics at the interfaces of the photoexcited hybrid materials. A detailed discussion on the renewable energy applicability of these QD/PS systems, such as absorber layers in solar cells, LEDs, and photodetectors, was presented. We believe that the critical outlook on the effect of QD incorporation in halide PS films on the effective charge carrier extraction and performance of PV and optoelectronic

devices has been able to provide a considerably better understanding of the strategy.

Semiconductor QDs and metal halide PSs are some of the most promising materials that hold the key to a sustainable future. Both families of materials possess excellent optoelectronic properties, which render them appropriate for PV and optoelectronic applications. Decades of extensive research on engineering non-radiative recombination pathways of conventional QDs via playing with surface defects has enabled their application in commercial PV applications. However, the introduction of hybrid organic–inorganic PSs in 2012 and all-inorganic PSs in 2015 completely stole the limelight

from QDs; further, they are now in the forefront in the competition to be the next-generation PV material because of their broad absorption spectrum, tunable exciton binding energy, exceptional charge carrier mobility, and high absorption coefficient. A substantial improvement in the issues of surface defects and stability needs to be considered before making PS-based PVs commercially competitive because most research efforts focus on them aim to increase the efficiency of the modules. To address these issues researchers deliberately couple the two most precious materials of our time. The strategic introduction of QDs within PS-based solar cells, LEDs, and photodetector devices enhanced their stability, efficacy and improved their light-harvesting properties. QDs (PbS or PbSe) with broad band gap tunability enable QD/PS hybrid systems to harvest low-energy (NIR) photons, which are totally restricted in sole PS systems. Besides these points, QDs can act as hole and electron transport materials, which accelerate charge carrier transfer and reduce charge recombination. The combination of QDs and PSs leads to some fascinating outcomes such as complementary light-harvesting, pinhole and defect-free PS crystal formation, rapid charge carrier extraction, and efficient carrier transport, which are important for device performance augmentation. Further, it is very promising for the chemistructural effect of QDs embedded in the PS matrix in the phase stability of pure FA or FA-rich PSs; a significant improvement has been achieved in the long-term stability of the devices prepared with QD additives because it is the most important challenge currently faced by PSCs.

Although some exciting results have been published in this field, the PCE of QD/PS hybrid solar cells or LEDs has not reached the current record values of pure halide PSs. The reason is twofold: the lack of proper design of both the materials and device and intrinsic surface defects of QDs. The effectiveness of these synergistic hybrid materials depends on the efficient tunneling of the charge carriers in a unidirectional manner and their light-harvesting ability. Thus far, the most studied synergistic combination in this field is MAPbI$_3$ and PbS QDs, and very few new combinations have been tested, which is a significant reason for the restricted growth of this field. The introduction of different QDs with various bandgaps can improve the light-harvesting properties. The choice of QDs is crucial for matching lattice mismatch and energy alignment. The surface engineering of the QDs also needs to be addressed in future works as trapping defects accelerate charge recombination, which restricts charge transport. Another major challenge is maximizing the synergistic benefit of the QD/PS system interface and band structure engineering.

Combining QDs with PSs has been so far proved to be an effective strategy for enhancing PV device performance and stability. However, considerable work must be conducted to achieve defect-free interfaces and manipulation of exciplex states between these two materials for advanced PV configurations. A more critical understanding of photoexcited carrier generation, carrier extraction, carrier transfer, and carrier recombination processes in hybrid interfaces is yet to be revealed, which can guide us toward a much better PV performance of these systems.

Conflict of Interest

The authors declare no conflict of interest.

[1] P. Horton, B. P. Horton, *One Earth* **2019**, *1*, 86.
[2] S. Chu, Y. Cui, N. Liu, *Nat. Mater.* **2016**, *16*, 16.
[3] S. Spillias, P. Kareiva, M. Ruckelshaus, E. McDonald-Madden, *Nat. Clim. Change* **2020**, *10*, 974.
[4] A. Kalair, N. Abas, M. S. Saleem, A. R. Kalair, N. Khan, *Energy Storage* **2021**, *3*, e135.
[5] D. Bogdanov, J. Farfan, K. Sadovskaia, A. Aghahosseini, M. Child, A. Gulagi, A. S. Oyewo, L. d. S. N. S. Barbosa, C. Breyer, *Nat. Commun.* **2019**, *10*, 1077.
[6] P. A. Owusu, S. Asumadu-Sarkodie, *Cogent Eng.* **2016**, *3*, 1167990.
[7] D. Groppi, A. Pfeifer, D. A. Garcia, G. Krajačić, N. Duić, *Renewable Sustainable Energy Rev.* **2021**, *135*, 110183.
[8] R. Rajesh, M. C. Mabel, *Renewable Sustainable Energy Rev.* **2015**, *51*, 231.
[9] M. L. Petrus, J. Schlipf, C. Li, T. P. Gujar, N. Giesbrecht, P. Müller-Buschbaum, M. Thelakkat, T. Bein, S. Hüttner, P. Docampo, *Adv. Energy Mater.* **2017**, *7*, 1700264.
[10] M. Victoria, N. Haegel, I. M. Peters, R. Sinton, A. Jäger-Waldau, C. Cañizo, C. Breyer, M. Stocks, A. Blakers, I. Kaizuka, K. Komoto, A. Smets, *Joule* **2021**, *5*, 1051.
[11] L. Wagner, S. Mastroianni, A. Hinsch, *Joule* **2020**, *4*, 882.
[12] J. Y. Kim, J. W. Lee, H. S. Jung, H. Shin, N. G. Park, *Chem. Rev.* **2020**, *120*, 7867.
[13] Q. Van Le, H. W. Jang, S. Y. Kim, *Small Methods* **2018**, *2*, 1700419.
[14] H. B. Kim, Y. J. Yoon, J. Jeong, J. Heo, H. Jang, J. H. Seo, B. Walker, J. Y. Kim, *Energy Environ. Sci.* **2017**, *10*, 1950.
[15] K. Yoshikawa, H. Kawasaki, W. Yoshida, T. Irie, K. Konishi, K. Nakano, T. Uto, D. Adachi, M. Kanematsu, H. Uzu, K. Yamamoto, *Nat. Energy* **2017**, *2*, 17032.
[16] D. Zhu, C. J. Humphreys, Solid-State Lighting Based on Light Emitting Diode Technology, *Optics in Our Time*, Springer Nature, Cham, Switzerland, **2016**, 87.
[17] K. Zhang, N. Zhu, M. Zhang, L. Wang, J. Xing, *J. Mater. Chem. C* **2021**, *9*, 3795.
[18] S. Mathew, A. Yella, P. Gao, R. Humphry-Baker, B. F. E. Curchod, N. Ashari-Astani, I. Tavernelli, U. Rothlisberger, M. K. Nazeeruddin, M. Grätzel, *Nat. Chem.* **2014**, *6*, 242.

[19] M. Freitag, J. Teuscher, Y. Saygili, X. Zhang, F. Giordano, P. Liska, J. Hua, S. M. Zakeeruddin, J. E. Moser, M. Grätzel, A. Hagfeldt, *Nat. Photonics* **2017**, *11*, 372.

[20] G. H. Carey, A. L. Abdelhady, Z. Ning, S. M. Thon, O. M. Bakr, E. H. Sargent, *Chem. Rev.* **2015**, *115*, 12732.

[21] Y. Zhang, G. Wu, F. Liu, C. Ding, Z. Zou, Q. Shen, *Chem. Soc. Rev.* **2020**, *49*, 49.

[22] Y. Shirasaki, G. J. Supran, M. G. Bawendi, V. Bulović, *Nat. Photonics* **2013**, *7*, 13.

[23] Z. Yang, M. Gao, W. Wu, X. Yang, X. W. Sun, J. Zhang, H. C. Wang, R. S. Liu, C. Y. Han, H. Yang, W. Li, *Mater. Today* **2019**, *24*, 69.

[24] K. P. Goetz, A. D. Taylor, Y. J. Hofstetter, Y. Vaynzof, *ACS Appl. Mater. Interfaces* **2021**, *13*, 1.

[25] H. S. Kim, C. R. Lee, J. H. Im, K. B. Lee, T. Moehl, A. Marchioro, S. J. Moon, R. Humphry-Baker, J. H. Yum, J. E. Moser, M. Grätzel, N. G. Park, *Sci. Rep.* **2012**, *2*, 591.

[26] Best Research-Cell Efficiency Chart, **2021**, https://www.nrel.gov/pv/cell-efficiency.html.

[27] W. Zou, R. Li, S. Zhang, Y. Liu, N. Wang, Y. Cao, Y. Miao, M. Xu, Q. Guo, D. Di, L. Zhang, C. Yi, F. Gao, R. H. Friend, J. Wang, W. Huang, *Nat. Commun.* **2018**, *9*, 608.

[28] H. Kim, L. Zhao, J. S. Price, A. J. Grede, K. Roh, A. N. Brigeman, M. Lopez, B. P. Rand, N. C. Giebink, *Nat. Commun.* **2018**, *9*, 4893.

[29] P. Liu, W. Wang, S. Liu, H. Yang, Z. Shao, *Adv. Energy Mater.* **2019**, *9*, 1803017.

[30] J. Huang, Y. Yuan, Y. Shao, Y. Yan, *Nat. Rev. Mater.* **2017**, *2*, 17042.

[31] G. Grancini, M. K. Nazeeruddin, *Nat. Rev. Mater.* **2019**, *4*, 4.

[32] D. Luo, R. Su, W. Zhang, Q. Gong, R. Zhu, *Nat. Rev. Mater.* **2020**, *5*, 44.

[33] J. Shi, Y. Li, Y. Li, D. Li, Y. Luo, H. Wu, Q. Meng, *Joule* **2018**, *2*, 879.

[34] B. Bahrami, A. H. Chowdhury, A. Gurung, S. Mabrouk, K. M. Reza, S. I. Rahman, R. Pathak, Q. Qiao, *Nano Today* **2020**, *33*, 100874.

[35] Y. Fu, H. Zhu, J. Chen, M. P. Hautzinger, X. Y. Zhu, S. Jin, *Nat. Rev. Mater.* **2019**, *4*, 169.

[36] J. Xue, R. Wang, Y. Yang, *Nat. Rev. Mater.* **2020**, *5*, 809.

[37] H. Ryu, H. J. Yoon, S. W. Kim, *Adv. Mater.* **2019**, *31*, 1802898.

[38] H. Chen, J. M. Pina, Y. Hou, E. H. Sargent, *Adv. Energy Mater.* **2022**, *12*, 2100774.

[39] W. Xiang, W. Tress, *Adv. Mater.* **2019**, *31*, 1902851.

[40] A. K. Jena, A. Kulkarni, T. Miyasaka, *Chem. Rev.* **2019**, *119*, 3036.

[41] Y. Chen, Y. Zhao, *J. Mater. Chem. A* **2020**, *8*, 25017.

[42] D. Yan, M. Liu, Z. Li, B. Hou, *J. Mater. Chem. A* **2021**, *9*, 15522.

[43] C. Hanmandlu, S. Swamy, A. Singh, H.-A. Chen, C. C. Liu, C. S. Lai, A. Mohapatra, C. W. Pao, P. Chen, C. W. Chu, *J. Mater. Chem. A* **2020**, *8*, 5263.

[44] A. Younis, L. Hu, P. Sharma, C. H. Lin, Y. Mi, X. Guan, D. Zhang, Y. Wang, T. He, X. Liu, B. Shabbir, S. Huang, J. Seidel, J. Tu, *Adv. Funct. Mater.* **2020**, *30*, 2002948.

[45] Z. Ning, X. Gong, R. Comin, G. Walters, F. Fan, O. Voznyy, E. Yassitepe, A. Buin, S. Hoogland, E. H. Sargent, *Nature* **2015**, *523*, 324.

[46] T. T. Ngo, I. Mora-Seró, *J. Phys. Chem. Lett.* **2019**, *10*, 1099.

[47] L. Lin, T. W. Jones, T. C. J. Yang, N. W. Duffy, J. Li, L. Zhao, B. Chi, X. Wang, G. J. Wilson, *Adv. Funct. Mater.* **2021**, *31*, 2008300.

[48] T. T. Ngo, S. Masi, P. F. Mendez, M. Kazes, D. Oron, I. M. Seró, *Nanoscale Adv.* **2019**, *1*, 4109.

[49] Y. Yang, W. Wang, *J. Power Sources* **2015**, *293*, 577.

[50] J. N. Arenas, A. Soosaimanickam, H. P. Adl, R. Abargues, P. P. Boix, P. J. Rodríguez-Cantó, J. P. Martínez-Pastor, *Nanomaterials* **2020**, *10*, 1297.

[51] Z. Yang, O. Voznyy, G. Walters, J. Z. Fan, M. Liu, S. Kinge, S. Hoogland, E. H. Sargent, *ACS Photonics* **2017**, *4*, 830.

[52] Y. Chen, J. Yang, S. Wang, Y. Wu, N. Yuan, W. H. Zhang, *iScience* **2020**, *23*, 100762.

[53] S. Masi, C. Echeverría-Arrondo, K. M. M. Salim, T. T. Ngo, P. F. Mendez, E. López-Fraguas, D. F. Macias-Pinilla, J. Planelles, J. I. Climente, I. Mora-Seró, *ACS Energy Lett.* **2020**, *5*, 418.

[54] H. E. Sánchez-Godoy, E. A. Erazo, A. F. Gualdrón-Reyes, A. H. Khan, S. Agouram, E. M. Barea, R. A. Rodriguez, I. Zarazúa, P. Ortiz, M. T. Cortés, V. Muñoz-Sanjosé, I. Moreels, S. Masi, I. Mora-Seró, *Adv. Energy Mater.* **2020**, *10*, 2002422.

[55] D. Zhao, J. Huang, R. Qin, G. Yang, J. Yu, *Adv. Opt. Mater.* **2018**, *6*, 1800979.

[56] J. Peng, Y. Chen, X. Zhang, A. Dong, Z. Liang, *Adv. Sci.* **2015**, *3*, 1500432.

[57] M. Albaladejo-Siguan, D. Becker-Koch, A. D. Taylor, Q. Sun, V. Lami, P. G. Oppenheimer, F. Paulus, Y. Vaynzof, *ACS Nano* **2020**, *14*, 384.

[58] R. S. Sanchez, M. S. De La Fuente, I. Suarez, G. Muñoz-Matutano, J. P. Martinez-Pastor, I. Mora-Sero, *Sci. Adv.* **2016**, *2*, 1501104.

[59] B. R. Sutherland, S. Hoogland, M. M. Adachi, C. Kanjanaboos, C. T. O. Wong, J. J. McDowell, J. Xu, O. Voznyy, Z. Ning, A. J. Houtepen, E. H. Sargent, *Adv. Mater.* **2015**, *27*, 53.

[60] P. Luo, S. Zhou, Z. Liu, W. Xia, L. Sun, J. Cheng, C. Xu, Y. Lu, *Chem. Commun.* **2016**, *52*, 11203.

[61] J. Pradhan, S. Mukherjee, A. H. Khan, A. Dalui, B. Satpati, C. U. Segre, D. D. Sarma, S. Acharya, *J. Phys. Chem. C* **2017**, *121*, 6401.

[62] S. S. Li, C. H. Chang, Y. C. Wang, C. W. Lin, D. Y. Wang, J. C. Lin, C. C. Chen, H. S. Sheu, H. C. Chia, W. R. Wu, U. S. Jeng, C. Te Liang, R. Sankar, F. C. Chou, C. W. Chen, *Energy Environ. Sci.* **2016**, *9*, 1282.

[63] Y. Zhang, Y. Han, Y. Xu, G. Yu, Y. Miao, C. Gao, X. Zhou, Y. Song, K. Jiang, *Sustainable Energy Fuels* **2021**, *5*, 3700.

[64] J. Qi, H. Xiong, G. Wang, H. Xie, W. Jia, Q. Zhang, Y. Li, H. Wang, *J. Power Sources* **2018**, *376*, 46.

[65] J. Xiao, S. Ma, S. Yu, C. Zhou, P. Liu, Y. Chen, *Nano Energy* **2018**, *46*, 45.

[66] C. H. Ravikumar, N. Maroli, B. Kulkarni, P. Kolandaivel, R. G. Balakrishna, *Mater. Sci. Eng., B* **2022**, *275*, 115513.

[67] R. Guo, C. Bao, F. Gao, J. Tian, *Adv. Opt. Mater.* **2020**, *8*, 2000557.

[68] Z. Duan, J. Ning, M. Chen, Y. Xiong, W. Yang, F. Xiao, S. V Kershaw, N. Zhao, S. Xiao, A. L. Rogach, *ACS Appl. Mater. Interfaces* **2020**, *12*, 35201.

[69] J. Han, X. Yin, H. Nan, Y. Zhou, Z. Yao, J. Li, D. Oron, H. Lin, *Small* **2017**, *13*, 1700953.

[70] G. W. Kim, A. Petrozza, *Adv. Energy Mater.* **2020**, *10*, 2001959.

[71] T. W. Jones, A. Osherov, M. Alsari, M. Sponseller, B. C. Duck, Y. K. Jung, C. Settens, F. Niroui, R. Brenes, C. V. Stan, Y. Li, M. Abdi-Jalebi, N. Tamura, J. E. MacDonald, M. Burghammer, R. H. Friend, V. Bulović, A. Walsh, G. J. Wilson, S. Lilliu, S. D. Stranks, *Energy Environ. Sci.* **2019**, *12*, 596.

[72] M. Kulbak, D. Cahen, G. Hodes, *J. Phys. Chem. Lett.* **2015**, *6*, 2452.

[73] M. Kulbak, S. Gupta, N. Kedem, I. Levine, T. Bendikov, G. Hodes, D. Cahen, *J. Phys. Chem. Lett.* **2016**, *7*, 167.

[74] J. Kang, L. Wang, *J. Phys. Chem. Lett.* **2017**, *8*, 489.

[75] S. ten Brinck, F. Zaccaria, I. Infante, *ACS Energy Lett.* **2019**, *4*, 2739.

[76] Z. Yao, W. Zhao, S. Liu, *J. Mater. Chem. A* **2021**, *9*, 11124.

[77] F. Penā-Camargo, P. Caprioglio, F. Zu, E. Gutierrez-Partida, C. M. Wolff, K. Brinkmann, S. Albrecht, T. Riedl, N. Koch, D. Neher, M. Stolterfoht, *ACS Energy Lett.* **2020**, *5*, 2728.

[78] C. Liu, Y. Yang, X. Xia, Y. Ding, Z. Arain, S. An, X. Liu, R. C. Cristina, S. Dai, M. K. Nazeeruddin, *Adv. Energy Mater.* **2020**, *10*, 1903751.

[79] X. Zhang, M. Lu, Y. Zhang, H. Wu, X. Shen, W. Zhang, W. Zheng, V. L. Colvin, W. W. Yu, *ACS Cent. Sci.* **2018**, *4*, 1352.

[80] X. Zhang, J. Zhang, D. Phuyal, J. Du, L. Tian, V. A. Öberg, M. B. Johansson, U. B. Cappel, O. Karis, J. Liu, H. Rensmo, G. Boschloo, E. M. J. Johansson, *Adv. Energy Mater.* **2018**, *8*, 1702049.

[81] J. Zhang, X. Liu, P. Jiang, H. Chen, Y. Wang, J. Ma, R. Zhang, F. Yang, M. Wang, J. Zhang, G. Tu, *Nano Energy* **2019**, *66*, 104142.

[82] J. Ge, W. Li, X. He, H. Chen, W. Fang, X. Du, Y. Li, L. Zhao, *Sustainable Energy Fuels* **2020**, *4*, 1837.

[83] L. Hu, L. Duan, Y. Yao, W. Chen, Z. Zhou, C. Cazorla, C. H. Lin, X. Guan, X. Geng, F. Wang, T. Wan, S. Wu, S. Cheong, R. D. Tilley, S. Liu, J. Yuan, D. Chu, T. Wu, S. Huang, *Adv. Sci.* **2021**, *9*, 2102258.

[84] S. Wang, C. Bi, A. Portniagin, J. Yuan, J. Ning, X. Xiao, X. Zhang, Y. Y. Li, S. V Kershaw, J. Tian, A. L. Rogach, *ACS Energy Lett.* **2020**, *5*, 2401.

[85] L. Hu, Z. Zhang, R. J. Patterson, S. B. Shivarudraiah, Z. Zhou, M. Ng, S. Huang, J. E. Halpert, *Sol. RRL* **2018**, *2*, 1800234.

[86] Z. Zhang, Z. Chen, L. Yuan, W. Chen, J. Yang, B. Wang, X. Wen, J. Zhang, L. Hu, J. A. Stride, G. J. Conibeer, R. J. Patterson, S. Huang, *Adv. Mater.* **2017**, *29*, 1703214.

[87] V. K. Ravi, S. Saikia, S. Yadav, V. V. Nawale, A. Nag, *ACS Energy Lett.* **2020**, *5*, 1794.

[88] R. Wang, F. Wang, W. Zhou, J. Z. Fan, F. P. G. de Arquer, K. Xu, E. H. Sargent, Z. Ning, *Infrared Phys. Technol.* **2019**, *98*, 16.

[89] C. Fan, X. Xu, K. Yang, F. Jiang, S. Wang, Q. Zhang, *Adv. Mater.* **2018**, *30*, 1804707.

[90] C. Li, A. Wang, X. Deng, S. Wang, Y. Yuan, L. Ding, F. Hao, *ACS Photonics* **2020**, *7*, 1893.

[91] J. Yin, O. M. Bakr, O. F. Mohammed, *J. Phys. Chem. C* **2021**, *125*, 9630.

[92] J. Peng, Y. Chen, K. Zheng, T. Pullerits, Z. Liang, *Chem. Soc. Rev.* **2017**, *46*, 5714.

[93] L. M. Herz, *Annu. Rev. Phys. Chem.* **2016**, *67*, 65.

[94] X. Deng, X. Wen, S. Huang, R. Sheng, T. Harada, T. W. Kee, M. Green, A. Ho-Baillie, *J. Phys. Chem. C* **2016**, *120*, 2542.

[95] C. Wehrenfennig, G. E. Eperon, M. B. Johnston, H. J. Snaith, L. M. Herz, *Adv. Mater.* **2014**, *26*, 1584.

[96] P. Piatkowski, B. Cohen, C. S. Ponseca, M. Salado, S. Kazim, S. Ahmad, V. Sundström, A. Douhal, *J. Phys. Chem. Lett.* **2016**, *7*, 204.

[97] M. De Bastiani, V. D'Innocenzo, S. D. Stranks, H. J. Snaith, A. Petrozza, *APL Mater.* **2014**, *2*, 081509.

[98] X. Wu, M. T. Trinh, D. Niesner, H. Zhu, Z. Norman, J. S. Owen, O. Yaffe, B. J. Kudisch, X. Y. Zhu, *J. Am. Chem. Soc.* **2015**, *137*, 2089.

[99] J. Butkus, P. Vashishtha, K. Chen, J. K. Gallaher, S. K. K. Prasad, D. Z. Metin, G. Laufersky, N. Gaston, J. E. Halpert, J. M. Hodgkiss, *Chem. Mater.* **2017**, *29*, 3644.

[100] L. Protesescu, S. Yakunin, M. I. Bodnarchuk, F. Krieg, R. Caputo, C. H. Hendon, R. X. Yang, A. Walsh, M. V. Kovalenko, *Nano Lett.* **2015**, *15*, 3692.

[101] T. Qiao, D. H. Son, *Acc. Chem. Res.* **2021**, *54*, 1399.

[102] Y. Wang, X. Li, J. Song, L. Xiao, H. Zeng, H. Sun, *Adv. Mater.* **2015**, *27*, 7101.

[103] Z. Y. Zhang, H. Y. Wang, Y. X. Zhang, Y. W. Hao, C. Sun, Y. Zhang, B. R. Gao, Q. D. Chen, H. B. Sun, *Sci. Rep.* **2016**, *6*, 27286.

[104] N. Mondal, A. Samanta, *Nanoscale* **2017**, *9*, 1878.

[105] M. Li, S. Bhaumik, T. W. Goh, M. S. Kumar, N. Yantara, M. Grätzel, S. Mhaisalkar, N. Mathews, T. C. Sum, *Nat. Commun.* **2017**, *8*, 3.

[106] H. Chung, S. Il Jung, H. J. Kim, W. Cha, E. Sim, D. Kim, W. K. Koh, J. Kim, *Angew. Chem., Int. Ed.* **2017**, *56*, 4160.

[107] J. Chen, M. E. Messing, K. Zheng, T. Pullerits, *J. Am. Chem. Soc.* **2019**, *141*, 3532.

[108] P. Papagiorgis, L. Protesescu, M. V. Kovalenko, A. Othonos, G. Itskos, *J. Phys. Chem. C* **2017**, *121*, 12434.

[109] G. R. Yettapu, D. Talukdar, S. Sarkar, A. Swarnkar, A. Nag, P. Ghosh, P. Mandal, *Nano Lett.* **2016**, *16*, 4838.

[110] B. A. Koscher, J. K. Swabeck, N. D. Bronstein, A. P. Alivisatos, *J. Am. Chem. Soc.* **2017**, *139*, 6566.

[111] D. P. Nenon, K. Pressler, J. Kang, B. A. Koscher, J. H. Olshansky, W. T. Osowiecki, M. A. Koc, L. W. Wang, A. P. Alivisatos, *J. Am. Chem. Soc.* **2018**, *140*, 17760.

[112] F. Liu, Y. Zhang, C. Ding, T. Toyoda, Y. Ogomi, T. S. Ripolles, S. Hayase, T. Minemoto, K. Yoshino, S. Dai, Q. Shen, *J. Phys. Chem. Lett.* **2018**, *9*, 294.

[113] S. Mandal, S. Mukherjee, C. K. De, D. Roy, S. Ghosh, P. K. Mandal, *J. Phys. Chem. Lett.* **2020**, *11*, 1702.

[114] J. Bo, X. Sun, P. Wan, D. Huang, X. Chen, M. Chen, R. Li, D. Shen, Q. Li, W. Xia, Z. Ye, Y. Chen, S. Chen, *J. Phys. Chem. Lett.* **2021**, *12*, 9115.

[115] T. Chiba, J. Kido, *J. Mater. Chem. C* **2018**, *6*, 11868.

[116] G. Li, F. W. R. Rivarola, N. J. L. K. Davis, S. Bai, T. C. Jellicoe, F. De La Peña, S. Hou, C. Ducati, F. Gao, R. H. Friend, N. C. Greenham, Z. K. Tan, *Adv. Mater.* **2016**, *28*, 3528.

[117] Y. Liu, G. Pan, R. Wang, H. Shao, H. Wang, W. Xu, H. Cui, H. Song, *Nanoscale* **2018**, *10*, 14067.

[118] A. L. Abdelhady, M. I. Saidaminov, B. Murali, V. Adinolfi, O. Voznyy, K. Katsiev, E. Alarousu, R. Comin, I. Dursun, L. Sinatra, E. H. Sargent, O. F. Mohammed, O. M. Bakr, *J. Phys. Chem. Lett.* **2016**, *7*, 295.

[119] G. Pan, X. Bai, D. Yang, X. Chen, P. Jing, S. Qu, L. Zhang, D. Zhou, J. Zhu, W. Xu, B. Dong, H. Song, *Nano Lett.* **2017**, *17*, 8005.

[120] M. Liu, G. Zhong, Y. Yin, J. Miao, K. Li, C. Wang, X. Xu, C. Shen, H. Meng, *Adv. Sci.* **2017**, *4*, 1700335.

[121] Z. J. Yong, S. Q. Guo, J. P. Ma, J. Y. Zhang, Z. Y. Li, Y. M. Chen, B. B. Zhang, Y. Zhou, J. Shu, J. L. Gu, L. R. Zheng, O. M. Bakr, H. T. Sun, *J. Am. Chem. Soc.* **2018**, *140*, 9942.

[122] X. Zhang, X. Wu, X. Liu, G. Chen, Y. Wang, J. Bao, X. Xu, X. Liu, Q. Zhang, K. Yu, W. Wei, J. Liu, J. Xu, H. Jiang, P. Wang, X. Wang, *J. Am. Chem. Soc.* **2020**, *142*, 4464.

[123] L. Gao, L. N. Quan, F. P. G. de Arquer, Y. Zhao, R. Munir, A. Proppe, R. Quintero-Bermudez, C. Zou, Z. Yang, M. I. Saidaminov, O. Voznyy, S. Kinge, Z. Lu, S. O. Kelley, A. Amassian, J. Tang, E. H. Sargent, *Nat. Photonics* **2020**, *14*, 227.

[124] A. Pramanik, K. Gates, S. Patibandla, D. Davis, S. Begum, R. Iftekhar, S. Alamgir, S. Paige, M. M. Porter, P. C. Ray, *ACS Appl. Bio Mater.* **2019**, *2*, 5872.

[125] X. Tang, X. Yang, S. Li, Z. Liu, Z. Hu, J. Hao, J. Du, Y. Leng, H. Qin, X. Lin, Y. Lin, Y. Tian, M. Zhou, Q. Xiong, *Adv. Sci.* **2019**, *6*, 1900412.

[126] P. Piatkowski, S. Masi, P. Galar, M. Gutiérrez, T. T. Ngo, I. Mora-Seró, A. Douhal, *J. Mater. Chem. C* **2020**, *8*, 14834.

[127] R. Quintero-Bermudez, R. P. Sabatini, M. Lejay, O. Voznyy, E. H. Sargent, *ACS Nano* **2017**, *11*, 12378.

[128] B. Sun, A. Johnston, C. Xu, M. Wei, Z. Huang, Z. Jiang, H. Zhou, Y. Gao, Y. Dong, O. Ouellette, X. Zheng, J. Liu, M. J. Choi, Y. Gao, S. W. Baek, F. Laquai, O. M. Bakr, D. Ban, O. Voznyy, F. P. G. de Arquer, E. H. Sargent, *Joule* **2020**, *4*, 1542.

[129] P. Galar, P. Piatkowski, T. T. Ngo, M. Gutiérrez, I. Mora-Seró, A. Douhal, *Nano Energy* **2018**, *49*, 471.

[130] A. H. Proppe, M. H. Elkins, O. Voznyy, R. D. Pensack, F. Zapata, L. V. Besteiro, L. N. Quan, R. Quintero-Bermudez, P. Todorovic, S. O. Kelley, A. O. Govorov, S. K. Gray, I. Infante, E. H. Sargent, G. D. Scholes, *J. Phys. Chem. Lett.* **2019**, *10*, 419.

[131] L. Hu, Z. Yang, A. Mandelis, A. Melnikov, X. Lan, G. Walters, S. Hoogland, E. H. Sargent, *J. Phys. Chem. C* **2016**, *120*, 14416.

[132] J. Dana, P. Maity, B. Jana, S. Maiti, H. N. Ghosh, *ACS Omega* **2018**, *3*, 2706.

[133] A. Brumberg, B. T. Diroll, G. Nedelcu, M. E. Sykes, Y. Liu, S. M. Harvey, M. R. Wasielewski, M. V. Kovalenko, R. D. Schaller, *Nano Lett.* **2018**, *18*, 4771.

[134] H. Tetsuka, A. Nagoya, T. Fukusumi, T. Matsui, *Adv. Mater.* **2016**, *28*, 4632.

[135] Z. Zhu, J. Ma, Z. Wang, C. Mu, Z. Fan, L. Du, Y. Bai, L. Fan, H. Yan, D. L. Phillips, S. Yang, *J. Am. Chem. Soc.* **2014**, *136*, 3760.

ADVANCED
SCIENCE NEWS

www.advancedsciencenews.com

ADVANCED
OPTICAL
MATERIALS

www.advopticalmat.de

[136] J. Ryu, J. W. Lee, H. Yu, J. Yun, K. Lee, J. Lee, D. Hwang, J. Kang, S. K. Kim, J. Jang, *J. Mater. Chem. A* **2017**, *5*, 16834.

[137] N. Fu, C. Huang, P. Lin, M. Zhu, T. Li, M. Ye, S. Lin, G. Zhang, J. Du, C. Liu, B. Xu, D. Wang, S. Ke, *J. Mater. Chem. A* **2018**, *6*, 8886.

[138] Y. Gong, J. Shen, Y. Zhu, W. Yan, J. Zhu, L. Hou, D. Xie, C. Li, *Appl. Surf. Sci.* **2021**, *545*, 149012.

[139] E. T. Vickers, T. A. Graham, A. H. Chowdhury, B. Bahrami, B. W. Dreskin, S. Lindley, S. B. Naghadeh, Q. Qiao, J. Z. Zhang, *ACS Energy Lett.* **2018**, *3*, 2931.

[140] X. Gong, L. Guan, Q. Li, Y. Li, T. Zhang, H. Pan, Q. Sun, Y. Shen, C. Grätzel, S. M. Zakeeruddin, M. Grätzel, M. Wang, *Sci. Adv.* **2020**, *6*, 5661.

[141] W. Yang, J. Chen, X. Lian, J. Li, F. Yao, G. Wu, W. Qiu, C. Jin, P. Heremans, H. Chen, *Sol. RRL* **2019**, *3*, 1970104.

[142] P. V. Kamat, *J. Phys. Chem. C* **2008**, *112*, 18737.

[143] S. Das, S. Rakshit, A. Datta, *J. Phys. Chem. C* **2020**, *124*, 28313.

[144] W. Xu, M. M. S. Lee, Z. Zhang, H. H. Y. Sung, I. D. Williams, R. T. K. Kwok, J. W. Y. Lam, D. Wang, B. Z. Tang, *Chem. Sci.* **2019**, *10*, 3494.

[145] Z. Pan, H. Rao, I. Mora-Seró, J. Bisquert, X. Zhong, *Chem. Soc. Rev.* **2018**, *47*, 7659.

[146] M. Albaladejo-Siguan, E. C. Baird, D. Becker-Koch, Y. Li, A. L. Rogach, Y. Vaynzof, *Adv. Energy Mater.* **2021**, *11*, 2003457.

[147] I. J. Kramer, E. H. Sargent, *Chem. Rev.* **2014**, *114*, 863.

[148] J. M. Pietryga, Y. S. Park, J. Lim, A. F. Fidler, W. K. Bae, S. Brovelli, V. I. Klimov, *Chem. Rev.* **2016**, *116*, 10513.

[149] P. V. Kamat, *J. Phys. Chem. Lett.* **2013**, *4*, 908.

[150] A. Kojima, K. Teshima, Y. Shirai, T. Miyasaka, *J. Am. Chem. Soc.* **2009**, *131*, 6050.

[151] Z. Li, T. R. Klein, D. H. Kim, M. Yang, J. J. Berry, M. F. A. M. Van Hest, K. Zhu, *Nat. Rev. Mater.* **2018**, *3*, 18017.

[152] N. G. Park, K. Zhu, *Nat. Rev. Mater.* **2020**, *5*, 333.

[153] P. Liu, N. Han, W. Wang, R. Ran, W. Zhou, Z. Shao, *Adv. Mater.* **2021**, *33*, 2002582.

[154] T. M. Brenner, D. A. Egger, L. Kronik, G. Hodes, D. Cahen, *Nat. Rev. Mater.* **2016**, *1*, 15007.

[155] T. Webb, S. J. Sweeney, W. Zhang, *Adv. Funct. Mater.* **2021**, *31*, 2103121.

[156] S. Masi, A. F. Gualdrón-Reyes, I. Mora-Seró, *ACS Energy Lett.* **2020**, *5*, 1974.

[157] W. Shockley, H. J. Queisser, *J. Appl. Phys.* **1961**, *32*, 510.

[158] S. Gholipour, A. M. Ali, J. P. Correa-Baena, S. H. Turren-Cruz, F. Tajabadi, W. Tress, N. Taghavinia, M. Grätzel, A. Abate, F. De Angelis, C. A. Gaggioli, E. Mosconi, A. Hagfeldt, M. Saliba, *Adv. Mater.* **2017**, *29*, 1702005.

[159] K. M. M. Salim, S. Masi, A. F. Gualdrón-Reyes, R. S. Sánchez, E. M. Barea, M. Krečmarová, J. F. Sánchez-Royo, I. Mora-Seró, *ACS Energy Lett.* **2021**, *6*, 3511.

[160] H. Hosokawa, R. Tamaki, T. Sawada, A. Okonogi, H. Sato, Y. Ogomi, S. Hayase, Y. Okada, T. Yano, *Nat. Commun.* **2019**, *10*, 4.

[161] V. Q. Dang, M. Byun, J. Kang, C. Kim, P. H. Jung, Y. D. Kim, N. E. Lee, H. Lee, *Org. Electron.* **2017**, *50*, 247.

[162] M. Liu, O. Voznyy, R. Sabatini, F. P. G. De Arquer, R. Munir, A. H. Balawi, X. Lan, F. Fan, G. Walters, A. R. Kirmani, S. Hoogland, F. Laquai, A. Amassian, E. H. Sargent, *Nat. Mater.* **2017**, *16*, 258.

[163] Y. Zhang, M. Gu, N. Li, Y. Xu, X. Ling, Y. Wang, S. Zhou, F. Li, F. Yang, K. Ji, J. Yuan, W. Ma, *J. Mater. Chem. A* **2018**, *6*, 24693.

[164] J. Han, S. Luo, X. Yin, Y. Zhou, H. Nan, J. Li, X. Li, D. Oron, H. Shen, H. Lin, *Small* **2018**, *14*, 1801016.

[165] R. Ma, Z. Ren, C. Li, Z. Huang, Y. Zhao, T. Yang, Y. Liang, X. W. Sun, W. C. H. Choy, *Small* **2020**, *16*, 2002628.

[166] X. Zheng, J. Troughton, N. Gasparini, Y. Lin, M. Wei, Y. Hou, J. Liu, K. Song, Z. Chen, C. Yang, B. Turedi, A. Y. Alsalloum, J. Pan,

J. Chen, A. A. Zhumekenov, T. D. Anthopoulos, Y. Han, D. Baran, O. F. Mohammed, E. H. Sargent, O. M. Bakr, *Joule* **2019**, *3*, 1963.

[167] L. Xie, P. Vashishtha, T. M. Koh, P. C. Harikesh, N. F. Jamaludin, A. Bruno, T. J. N. Hooper, J. Li, Y. F. Ng, S. G. Mhaisalkar, N. Mathews, *Adv. Mater.* **2020**, *32*, 2003296.

[168] W. Yang, R. Su, D. Luo, Q. Hu, F. Zhang, Z. Xu, H. Zhong, Q. Gong, T. P. Russell, R. Zhu, *Nano Energy* **2020**, *67*, 104189.

[169] M. F. M. Noh, C. H. Teh, R. Daik, E. L. Lim, C. C. Yap, M. A. Ibrahim, N. A. Ludin, A. R. B. M. Yusoff, J. Jang, M. A. Mat Teridi, *J. Mater. Chem. C* **2018**, *6*, 682.

[170] J. Lian, B. Lu, F. Niu, P. Zeng, X. Zhan, *Small Methods* **2018**, *2*, 1800082.

[171] A. M. Elseman, C. Xu, Y. Yao, M. Elisabeth, L. Niu, L. Malavasi, Q. L. Song, *Sol. RRL* **2020**, *4*, 2000136.

[172] K. Wang, S. Olthof, W. S. Subhani, X. Jiang, Y. Cao, L. Duan, H. Wang, M. Du, S. (Frank) Liu, *Nano Energy* **2020**, *68*, 104289.

[173] L. Zhu, X. Shang, K. Lei, C. Wu, S. Zheng, C. Chen, H. Song, *Sol. RRL* **2021**, *5*, 2000605.

[174] T. Kim, J. Lim, S. Song, *Energies* **2020**, *13*, 5572.

[175] L. Gao, C. Liu, F. Meng, A. Liu, Y. Li, Y. Li, C. Zhang, M. Fan, G. Wei, T. Ma, *ACS Sustainable Chem. Eng.* **2020**, *8*, 9250.

[176] T. Yokoyama, Y. Nishitani, Y. Miyamoto, S. Kusumoto, R. Uchida, T. Matsui, K. Kawano, T. Sekiguchi, Y. Kaneko, *ACS Appl. Mater. Interfaces* **2020**, *12*, 27131.

[177] W. Zhu, Z. Zhang, W. Chai, Q. Zhang, D. Chen, Z. Lin, J. Chang, J. Zhang, C. Zhang, Y. Hao, *ChemSusChem* **2019**, *12*, 2318.

[178] P. Calado, A. M. Telford, D. Bryant, X. Li, J. Nelson, B. C. O'Regan, P. R. F. Barnes, *Nat. Commun.* **2016**, *7*, 13831.

[179] J. You, L. Meng, T. Bin Song, T. F. Guo, W. H. Chang, Z. Hong, H. Chen, H. Zhou, Q. Chen, Y. Liu, N. De Marco, Y. Yang, *Nat. Nanotechnol.* **2016**, *11*, 75.

[180] T. Cao, K. Chen, Q. Chen, Y. Zhou, N. Chen, Y. Li, *ACS Appl. Mater. Interfaces* **2019**, *11*, 33825.

[181] Q. Jiang, X. Zhang, J. You, *Small* **2018**, *14*, 1801154.

[182] L. Wang, W. Fu, Z. Gu, C. Fan, X. Yang, H. Li, H. Chen, *J. Mater. Chem. C* **2014**, *2*, 9087.

[183] X. Zeng, T. Zhou, C. Leng, Z. Zang, M. Wang, W. Hu, X. Tang, S. Lu, L. Fang, M. Zhou, *J. Mater. Chem. A* **2017**, *5*, 17499.

[184] F. Tan, W. Xu, X. Hu, P. Yu, W. Zhang, *Nanoscale Res. Lett.* **2017**, *12*, 614.

[185] J. Wang, L. Liu, S. Liu, L. Yang, B. Zhang, S. Feng, J. Yang, X. Meng, W. Fu, H. Yang, *Sustainable Energy Fuels* **2017**, *1*, 504.

[186] Z. Gu, F. Chen, X. Zhang, Y. Liu, C. Fan, G. Wu, H. Li, H. Chen, *Sol. Energy Mater. Sol. Cells* **2015**, *140*, 396.

[187] I. Hwang, K. Yong, *ACS Appl. Mater. Interfaces* **2016**, *8*, 4226.

[188] M. Abulikemu, J. Barbé, A. El Labban, J. Eid, S. Del Gobbo, *Thin Solid Films* **2017**, *636*, 512.

[189] Z. Song, G. Tong, H. Li, G. Li, S. Ma, S. Yu, Q. Liu, Y. Jiang, *Nanotechnology* **2018**, *29*, 025401.

[190] H. Peng, W. Sun, Y. Li, W. Yan, P. Yu, H. Zhou, Z. Bian, C. Huang, *J. Photonics Energy* **2016**, *6*, 022002.

[191] J. Dong, J. Wu, J. Jia, L. Fan, Y. Lin, J. Lin, M. Huang, *J. Mater. Chem. C* **2017**, *5*, 10023.

[192] X. Liu, C. C. Chueh, Z. Zhu, S. B. Jo, Y. Sun, A. K. Y. Jen, *J. Mater. Chem. A* **2016**, *4*, 15294.

[193] Y. Wang, M. Zhong, W. Wang, Q. Wang, W. Wu, X. Luo, *Appl. Surf. Sci.* **2019**, *495*, 143552.

[194] M. Imran, H. Coşkun, F. H. Isikgor, L. Bichen, N. A. Khan, J. Ouyang, *J. Mater. Chem. A* **2018**, *6*, 22713.

[195] X. Li, J. Yang, Q. Jiang, H. Lai, S. Li, J. Xin, W. Chu, J. Hou, *ACS Nano* **2018**, *12*, 5605.

[196] Y. Hou, X. Chen, S. Yang, Y. L. Zhong, C. Li, H. Zhao, H. G. Yang, *Nano Energy* **2017**, *36*, 102.

[197] Z. Xu, J. Wu, Y. Yang, Z. Lan, J. Lin, *ACS Appl. Energy Mater.* **2018**, *1*, 4050.

[198] B. Yang, M. Wang, X. Hu, T. Zhou, Z. Zang, *Nano Energy* **2019**, *57*, 718.

[199] R. Singh, P. K. Singh, B. Bhattacharya, H. W. Rhee, *Appl. Mater. Today* **2019**, *14*, 175.

[200] J. Chen, N. G. Park, *ACS Energy Lett.* **2020**, *5*, 2742.

[201] A. M. Elseman, S. Sajid, A. E. Shalan, S. A. Mohamed, M. M. Rashad, *Appl. Phys. A: Mater. Sci. Process.* **2019**, *125*, 476.

[202] Z. Shariatinia, *Renewable Sustainable Energy Rev.* **2020**, *119*, 109608.

[203] P. K. Kung, M. H. Li, P. Y. Lin, Y. H. Chiang, C. R. Chan, T. F. Guo, P. Chen, *Adv. Mater. Interfaces* **2018**, *5*, 1800882.

[204] A. Fakharuddin, M. Vasilopoulou, A. Soultati, M. I. Haider, J. Briscoe, V. Fotopoulos, D. Di Girolamo, D. Davazoglou, A. Chroneos, A. R. b. M. Yusoff, A. Abate, L. Schmidt-Mende, M. K. Nazeeruddin, *Sol. RRL* **2021**, *5*, 2000555.

[205] Z. Yang, B. H. Babu, S. Wu, T. Liu, S. Fang, Z. Xiong, L. Han, W. Chen, *Sol. RRL* **2020**, *4*, 1900257.

[206] X. Yin, Z. Song, Z. Li, W. Tang, *Energy Environ. Sci.* **2020**, *13*, 4057.

[207] T. Swetha, S. P. Singh, *J. Mater. Chem. A* **2015**, *3*, 18329.

[208] X. Liu, X. Ding, Y. Ren, Y. Yang, Y. Ding, X. Liu, A. Alsaedi, T. Hayat, J. Yao, S. Dai, *J. Mater. Chem. C* **2018**, *6*, 12912.

[209] S. Gangala, R. Misra, *J. Mater. Chem. A* **2018**, *6*, 18750.

[210] J. H. Heo, H. J. Han, D. Kim, T. K. Ahn, S. H. Im, *Energy Environ. Sci.* **2015**, *8*, 1602.

[211] X. Hu, X. Meng, L. Zhang, Y. Zhang, Z. Cai, Z. Huang, M. Su, Y. Wang, M. Li, F. Li, X. Yao, F. Wang, W. Ma, Y. Chen, Y. Song, *Joule* **2019**, *3*, 2205.

[212] L. Caliò, J. Follana-Berná, S. Kazim, M. Madsen, H. G. Rubahn, Á. Sastre-Santos, S. Ahmad, *Sustainable Energy Fuels* **2017**, *1*, 2071.

[213] M. Haider, C. Zhen, T. Wu, J. Wu, C. Jia, G. Liu, H. M. Cheng, *Chem. Commun.* **2019**, *55*, 5343.

[214] M. Urbani, G. De La Torre, M. K. Nazeeruddin, T. Torres, *Chem. Soc. Rev.* **2019**, *48*, 2738.

[215] Z. Yu, A. Hagfeldt, L. Sun, *Coord. Chem. Rev.* **2020**, *406*, 213143.

[216] Z. Hawash, L. K. Ono, Y. Qi, *Adv. Mater. Interfaces* **2018**, *5*, 1700623.

[217] N. D. Pham, J. Shang, Y. Yang, M. T. Hoang, V. T. Tiong, X. Wang, L. Fan, P. Chen, L. Kou, L. Wang, H. Wang, *Nano Energy* **2020**, *69*, 104412.

[218] T. H. Schloemer, J. A. Christians, J. M. Luther, A. Sellinger, *Chem. Sci.* **2019**, *10*, 1904.

[219] G. Ren, W. Han, Y. Deng, W. Wu, Z. Li, J. Guo, H. Bao, C. Liu, W. Guo, *J. Mater. Chem. A* **2021**, *9*, 4589.

[220] S. Wang, M. Sina, P. Parikh, T. Uekert, B. Shahbazian, A. Devaraj, Y. S. Meng, *Nano Lett.* **2016**, *16*, 5594.

[221] S. N. Habisreutinger, N. K. Noel, H. J. Snaith, R. J. Nicholas, *Adv. Energy Mater.* **2017**, *7*, 1601079.

[222] H. Zhou, Q. Chen, G. Li, S. Luo, T.-b. Song, H.-S. Duan, Z. Hong, J. You, Y. Liu, Y. Yang, *Science* **2014**, *345*, 542.

[223] D. Liu, S. Li, P. Zhang, Y. Wang, R. Zhang, H. Sarvari, F. Wang, J. Wu, Z. Wang, Z. D. Chen, *Nano Energy* **2017**, *31*, 462.

[224] S. Sidhik, A. C. Pasarán, D. Esparza, T. L. Luke, R. Carriles, E. De La Rosa, *ACS Appl. Mater. Interfaces* **2018**, *10*, 3571.

[225] L. Caliò, M. Salado, S. Kazim, S. Ahmad, *Joule* **2018**, *2*, 1800.

[226] L. Hu, W. Wang, H. Liu, J. Peng, H. Cao, G. Shao, Z. Xia, W. Ma, J. Tang, *J. Mater. Chem. A* **2015**, *3*, 515.

[227] X. Zheng, H. Lei, G. Yang, W. Ke, Z. Chen, J. Ma, Q. Guo, F. Yao, Q. Zhang, H. Xu, G. Fang, *Nano Energy* **2017**, *38*, 1.

[228] G. Li, J. Song, D. Wang, W. Sun, J. Wu, Z. Lan, *J. Power Sources* **2021**, *481*, 229149.

[229] J. W. Xiao, S. Ma, S. Yu, C. Zhou, P. Liu, Y. Chen, H. Zhou, Y. Li, Q. Chen, *Nano Energy* **2018**, *46*, 45.

[230] M. M. Tavakoli, H. T. Dastjerdi, D. Prochowicz, P. Yadav, R. Tavakoli, M. Saliba, Z. Fan, *J. Mater. Chem. A* **2019**, *7*, 14753.

[231] B. Gil, A. J. Yun, Y. Lee, J. Kim, B. Lee, B. Park, *Electron. Mater. Lett.* **2019**, *15*, 505.

[232] M. Bidikoudi, E. Kymakis, *J. Mater. Chem. C* **2019**, *7*, 13680.

[233] J. S. Shaikh, N. S. Shaikh, Y. K. Mishra, P. Kanjanaboos, P. M. Shewale, S. Sabale, S. Praserthdam, C. D. Lokhande, *Mater. Today Chem.* **2021**, *20*, 100427.

[234] D. Di Girolamo, F. Di Giacomo, F. Matteocci, A. G. Marrani, D. Dini, A. Abate, D. Di Girolamo, *Chem. Sci.* **2020**, *11*, 7746.

[235] M. Y. Woo, K. Choi, J. H. Lee, S. Y. Park, J. H. Noh, *Adv. Energy Mater.* **2021**, *2003119*, 2003119.

[236] X. Chen, W. Xu, N. Ding, Y. Ji, G. Pan, J. Zhu, D. Zhou, Y. Wu, C. Chen, H. Song, *Adv. Funct. Mater.* **2020**, *30*, 2003295.

[237] J. Y. Kim, W. Baek, S. Kim, G. Kang, I. K. Han, T. Hyeon, M. Park, *Appl. Surf. Sci.* **2019**, *496*, 143610.

[238] Y. Zhang, Z. Zhang, Y. Liu, H. Gao, Y. Mao, *Mater. Sci. Semicond. Process.* **2020**, *120*, 105267.

[239] W. Ma, Z. Zhang, M. Ma, Y. Liu, G. Pan, H. Gao, Y. Mao, *Sol. Energy* **2020**, *211*, 55.

[240] Z. J. Zhou, Y. Q. Deng, P. P. Zhang, D. X. Kou, W. H. Zhou, Y. N. Meng, S. J. Yuan, S. X. Wu, *Sol. RRL* **2019**, *3*, 1800354.

[241] Y. Liu, X. Zhao, Z. Yang, Q. Li, W. Wei, B. Hu, W. Chen, *ACS Appl. Energy Mater.* **2020**, *3*, 3521.

[242] C. Yang, Z. Wang, Y. Lv, R. Yuan, Y. Wu, W. H. Zhang, *Chem. Eng. J.* **2021**, *406*, 126855.

[243] L. Najafi, B. Taheri, B. Martín-García, S. Bellani, D. Di Girolamo, A. Agresti, R. Oropesa-Nunìez, S. Pescetelli, L. Vesce, E. Calabrò, M. Prato, A. E. Del Rio Castillo, A. Di Carlo, F. Bonaccorso, *ACS Nano* **2018**, *12*, 10736.

[244] S. K. Muduli, E. Varrla, S. A. Kulkarni, G. Han, K. Thirumal, O. Lev, S. Mhaisalkar, N. Mathews, *J. Power Sources* **2017**, *371*, 156.

[245] W. Chen, K. Li, Y. Wang, X. Feng, Z. Liao, Q. Su, X. Lin, Z. He, *J. Phys. Chem. Lett.* **2017**, *8*, 591.

[246] X. Gong, L. Guan, Q. Li, Y. Li, T. Zhang, H. Pan, Q. Sun, Y. Shen, C. Grätzel, S. M. Zakeeruddin, M. Grätzel, M. Wang, *Sci. Adv.* **2020**, *6*, 5661.

[247] V. Ferguson, S. R. P. Silva, W. Zhang, *Energy Environ. Mater.* **2019**, *2*, 107.

[248] J. Han, Y. Zhou, X. Yin, H. Nan, M. Tai, Y. Gu, J. Li, D. Oron, H. Lin, *Sol. RRL* **2019**, *3*, 1900146.

[249] H. Chen, Q. Luo, T. Liu, M. Tai, J. Lin, V. Murugadoss, H. Lin, J. Wang, Z. Guo, N. Wang, *ACS Appl. Mater. Interfaces* **2020**, *12*, 13941.

[250] M. Que, Z. Dai, H. Yang, H. Zhu, Y. Zong, W. Que, N. P. Padture, Y. Zhou, O. Chen, *ACS Energy Lett.* **2019**, *4*, 1970.

[251] S. Akin, Y. Altintas, E. Mutlugun, S. Sonmezoglu, *Nano Energy* **2019**, *60*, 557.

[252] H. C. Wang, Z. Bao, H. Y. Tsai, A. C. Tang, R.-S. Liu, *Small* **2018**, *14*, 1702433.

[253] C. Zou, C. Zhang, Y. H. Kim, L. Y. Lin, J. M. Luther, *ACS Photonics* **2021**, *8*, 386.

[254] E. Yassitepe, Z. Yang, O. Voznyy, Y. Kim, G. Walters, J. A. Castañeda, P. Kanjanaboos, M. Yuan, X. Gong, F. Fan, J. Pan, S. Hoogland, R. Comin, O. M. Bakr, L. A. Padilha, A. F. Nogueira, E. H. Sargent, *Adv. Funct. Mater.* **2016**, *26*, 8757.

[255] J. Pan, L. N. Quan, Y. Zhao, W. Peng, B. Murali, S. P. Sarmah, M. Yuan, L. Sinatra, N. M. Alyami, J. Liu, E. Yassitepe, Z. Yang, O. Voznyy, R. Comin, M. N. Hedhili, O. F. Mohammed, Z. H. Lu, D. H. Kim, E. H. Sargent, O. M. Bakr, *Adv. Mater.* **2016**, *28*, 8718.

[256] X. Zhang, W. Yin, W. Zheng, A. L. Rogach, *ACS Energy Lett.* **2020**, *5*, 2927.

[257] X. Gong, Z. Yang, G. Walters, R. Comin, Z. Ning, E. Beauregard, V. Adinolfi, O. Voznyy, E. H. Sargent, *Nat. Photonics* **2016**, *10*, 253.

[258] Y. Liu, Y. Dong, T. Zhu, D. Ma, A. Proppe, B. Chen, C. Zheng, Y. Hou, S. Lee, B. Sun, E. H. Jung, F. Yuan, Y. K. Wang, L. K. Sagar, S. Hoogland, F. P. G. De Arquer, M. J. Choi, K. Singh, S. O. Kelley, O. Voznyy, Z. H. Lu, E. H. Sargent, *J. Am. Chem. Soc.* **2021**, *143*, 15606.

[259] T. T. Ngo, I. Suarez, R. S. Sanchez, J. P. Martinez-Pastor, I. Mora-Sero, *Nanoscale* **2016**, *8*, 14379.

[260] R. R. Rad, A. F. Gualdrón-Reyes, S. Masi, B. A. Ganji, N. Taghavinia, S. Gené-Marimon, E. Palomares, I. Mora-Seró, *Adv. Opt. Mater.* **2021**, *9*, 2001508.

[261] I. J. Luxmoore, P. Q. Liu, P. Li, J. Faist, G. R. Nash, *ACS Photonics* **2016**, *3*, 936.

[262] A. S. Pawbake, R. G. Waykar, D. J. Late, S. R. Jadkar, *ACS Appl. Mater. Interfaces* **2016**, *8*, 3359.

[263] X. Hu, X. Zhang, L. Liang, J. Bao, S. Li, W. Yang, Y. Xie, *Adv. Funct. Mater.* **2014**, *24*, 7373.

[264] C. Li, H. Wang, F. Wang, T. Li, M. Xu, H. Wang, Z. Wang, X. Zhan, W. Hu, L. Shen, *Light: Sci. Appl.* **2020**, *9*, 31.

[265] F. P. G. De Arquer, X. Gong, R. P. Sabatini, M. Liu, G. H. Kim, B. R. Sutherland, O. Voznyy, J. Xu, Y. Pang, S. Hoogland, D. Sinton, E. Sargent, *Nat. Commun.* **2017**, *8*, 14757.

[266] Y. Yu, Y. Zhang, Z. Zhang, H. Zhang, X. Song, M. Cao, Y. Che, H. Dai, J. Yang, J. Wang, H. Zhang, J. Yao, *J. Phys. Chem. Lett.* **2017**, *8*, 445.

[267] X. Zhao, H. Yu, P. Wang, K. Li, Y. Fang, Y. Tao, X. Song, H. Zhang, *ACS Appl. Electron. Mater.* **2020**, *2*, 4080.

[268] R. Guo, F. Huang, K. Zheng, T. Pullerits, J. Tian, *ACS Appl. Mater. Interfaces* **2018**, *10*, 35656.

[269] Z. Li, H. Li, K. Jiang, D. Ding, J. Li, C. Ma, S. Jiang, Y. Wang, T. D. Anthopoulos, Y. Shi, *ACS Appl. Mater. Interfaces* **2019**, *11*, 40204.

[270] C. Liu, H. Peng, K. Wang, C. Wei, Z. Wang, X. Gong, *Nano Energy* **2016**, *30*, 27.

Soumyadipta Rakshit did his bachelors, masters, and Ph.D. from Jadavpur University. Before joining Universidad de Castilla-La Mancha (UCLM) as a Marie Curie Postdoctoral Fellow he was a National Postdoctoral Fellow at IIT Bombay. His current research interest focuses on charge carrier dynamics and fluorescence blinking of photo-excited Pb-free perovskite nanocrystals and different photo-induced processes in environmentally benign semiconductor quantum dots.

Piotr Piatkowski received his Ph.D. degree in Chemistry from the University of Warsaw in 2010. From 2013 to 2016 he was a Postdoctoral Researcher at the Departamento de Química Física, Universidad de Castilla-La Mancha (UCLM), Toledo, Spain. In 2017 he was hired in the Faculty of Chemistry, University of Warsaw, Poland. In 2022 he got a new position in Department of Physics, American University of Sharjah, United Arabs Emirates. His research focuses mainly on the ultrafast processes photoinduced in semiconductor materials of different dimensionality. In his work, he uses predominantly ultrafast time-resolved pump-probe optical spectroscopies.

Iván Mora-Seró (Ph.D. Physics 2004) is Full Professor at Universitat Jaume I de Castelló (Spain) in the Institute of Advanced Materials (INAM). His research is focused on crystal growth, nanostructured devices, transport and recombination properties, photocatalysis, characterization and development of photovoltaic and optoelectronic devices. Recent research activities are focused on new concepts for photovoltaic conversion and light emission (LEDs and light amplifiers) based on nanoscaled devices and semiconductor materials following two main lines: Semiconductor quantum dots and halide perovskites.

2102566 (32 of 33)

**ADVANCED
SCIENCE NEWS**

www.advancedsciencenews.com

**ADVANCED
OPTICAL
MATERIALS**

www.advopticalmat.de

Abderrazzak Douhal, a Full Professor of physical chemistry at the University of Castilla La Mancha (UCLM, Toledo), has received his Ph.D. degree in chemistry from University of Kadi Ayyad (Marrakech). He was a Visiting Researcher at California Institute of Technology in several periods of 1995–2000, collaborating with Prof. Ahmed H. Zewail. Since 1998, he is heading the Femtoscience and Microscopy research group at the UCLM (https://www.uclm.es/grupos/fmg), focusing his current research on deciphering fs-ms photoevents in advanced materials for photonic applications. In 2018, he was awarded the Elsevier Lecture Award from the Japanese Photochemistry Association. ORCID: 0000-0003-2247-7566. Researcher ID: L-4940-2014.